Magnetic Order in Two-Dimensional Nanoparticle Assemblies

Mirela Georgescu

Published by: Shaker Publishing BV
ISBN: 978-90-393-4955-7
Cover: Disorder on billboard, Manhattan, New York

Magnetic Order in Two-Dimensional Nanoparticle Assemblies

Magnetische ordening in tweedimensionale systemen van nanodeeltjes
(met een samenvatting in het Nederlands)

Proefschrift

ter verkrijging van de graad van doctor aan de Universiteit Utrecht op gezag van de rector magnificus, prof. dr. J.C. Stoof, ingevolge het besluit van het college voor promoties in het openbaar te verdedigen
op maandag 15 december 2008 des middags te 2.30 uur

door

Mirela Georgescu

geboren op 07 december 1978
te Galaţi, Roemenië

Promotor: Prof. dr. F. H. P. M. Habraken

Co-promotor: Dr. P. A. Zeijlmans van Emmichoven

Contents

1 Introduction

1.1 Magnetic nanoparticles

The term *nanotechnology* was created by Norio Taniguchy of Tokio University in 1974 [1] to describe the precision manufacture of materials with nanometer tolerance. Its origin dates already back to Richard Feynman's 1959 talk *There's Plenty of Room at the Bottom* in which he proposed the direct manipulation of individual atoms as a more powerful form of synthetic chemistry. Today nanotechnology is considered to encompass the creation of functional materials, devices and systems through control of matter on the nanometer scale ($1\ nm = 10^{-9}\ m$) and the exploitation of novel properties and phenomena developed at that scale. One of the subjects within nanotechnology is the creation of nanoparticles and the study of their physical and chemical properties and of their applications.

The earliest known use of nanoparticles is in the ninth century when Arab potters used nanoparticles in their glasses so that objects would change color when viewed from another angle. Later the chemists have been making polymers, which were large molecules made up of nanoscale subunits, to create silver coatings for photographic films [2]. The study of nanoparticles is nowadays a well-established and dynamic research area in applied science that exhibits many fundamental aspects as well. It focuses on a better control and manipulation of the size, shape, composition, degree of crystallinity [3, 4], and on a better characterization of the nanoparticles [5].

The properties of the nanoparticles of a certain material can be different from the properties of objects of the same material with macroscopic dimensions for two main reasons. First, the nanoparticles have a larger ratio of their surface area to their volume. Since at the surface different phenomena play a role compared to in the bulk, the smaller the particles the stronger the surface

effects. Second, below 50 nm the laws of classical physics give way to quantum effects, provoking optical and electronic behavior different from those of the bulk.

Magnetic nanoparticles i.e. nanoparticles containing magnetic material, are produced using advanced chemical methods [3,4]. The synthesis is usually based on the reduction of organometallic precursors in a solution at high temperature in the presence of surfactant molecules. It results in the formation of clusters (critical nuclei), which further grow to form the nanoparticles. The surfactant has the role of controlling the shape and size of the particles: it lowers the surface tension, it prevents the agglomeration of particles, protects the particles against oxidation and defines the minimum interparticle distance.

The magnetic properties of the nanoparticles depend on their size, structure, crystallinity, shape, material, temperature, etc. With such a large playground, the magnetic nanoparticles may be interesting for application in magnetic storage technology. In present-day high-density hard disks, the information is stored in thin films consisting of nanometer-sized, arbitrarily shaped magnetic grains. A single bit corresponds to a large group of grains with their magnetic moments aligned. The increase of bit density by scaling down the dimensions of the grains will come to an end when, due to thermal effects, information will be lost within an appreciable period of time [6, 7]. The magnetic nanoparticles are good candidates to constitute the future hard disks magnetic medium, with an improved performance and increased information areal density.

Magnetic nanoparticles have also applications in other domains like medicine, pharmaceutics, and biotechnology [8,9]. Since the size of the nanoparticles can be tuned in a controlled way, they can be made as large as a cell, virus, protein or gene. They can be coated with specific biological molecules in order to bind or not with the targeted molecules. Since the nanoparticles are magnetic, they (or the molecules they are attached to) can be manipulated by external magnetic fields in order to bring a package in the desired area of the body. In addition, they can respond resonantly to an external magnetic field, causing a transfer of energy from the external field to the nanoparticles. This phenomenon can be used in medical treatments.

Magnetic nanoparticles with a size of 30 nm or smaller usually consist of a single magnetic domain state. They present magnetic anisotropy, which is a direction dependence of the material magnetic properties. There are different sources of magnetic anisotropy:

- Magnetocrystalline anisotropy: the electronic structure of the crystal induces preferential directions for the magnetization.

- Shape anisotropy: when the particles are not spherical, one or more preferential directions are present.

- Stress anisotropy: a distorted crystal lattice changes the interactions between the atoms, leading to magnetic anisotropy.

- Exchange anisotropy: occurs when antiferromagnetic and ferromagnetic materials (like, for example, cobalt and cobalt oxide) interact.

For non-interacting, spherical particles, with a magnetic moment $\mathbf{m}$, the main source of anisotropy is magnetocrystalline anisotropy, which involves electrostatic crystal-field interaction and relativistic spin-orbit coupling [10]. Depending on the crystal symmetry, magnetic materials can exhibit uniaxial or multiaxial anisotropy. For particles with uniaxial symmetry, if we consider (for simplicity purposes) the easy direction along the z-direction, the anisotropy energy E_A is, in first order:

$$E_A(\theta) = K_A V \sin^2 \theta \tag{1.1}$$

where K_A is the anisotropy constant in units of energy per unit volume (J/m^3), V is the (magnetic) volume of the nanoparticle and θ is the angle between the magnetic moment $\mathbf{m}$ and the z direction. When $K_A > 0$ the anisotropy has two minima at $\theta = 0$ and $\theta = \pi$. This case is referred to as *easy axis anisotropy*. Conversely, when $K_A < 0$ the energy is minimized for $\theta = \pi/2$, meaning that any direction in the *xy* plane corresponds to an easy direction. This case is referred to as *easy plane anisotropy*. The most frequent multiaxial anisotropy is cubic anisotropy [11]. For particles with cubic anisotropy, three special directions exist. The anisotropy energy in this case is [12]:

$$E_A(\mathbf{m}) = K_1 V(m_x^2 \cdot m_y^2 + m_y^2 \cdot m_z^2 + m_z^2 \cdot m_x^2) + K_2 V m_x^2 \cdot m_y^2 \cdot m_z^2 \tag{1.2}$$

where K_1 and K_2 are called the first and second order anisotropy constants and m_x, m_y, m_z are the projections of the vector $\mathbf{m}/|\mathbf{m}|$ along the privileged directions. Since K_2 is, in most cases, small compared to K_1, we will ignore the second term in relation 1.2 . In the case of $K_1 > 0$ there are six energy minima along the three directions; they are the easy directions. For the case of $K_1 < 0$ we obtain a more complex situation with eight energy minima and the three axes becoming the hard axes.

Due to thermal agitation, a particle attempts to reorient its magnetic moment with the frequency corresponding to the Néel relaxation time [13]:

$$\tau = \tau_0 \exp \frac{E_A}{k_B T} \tag{1.3}$$

where $\tau_0 \approx 10^{-10}\ s$ is the microscopic relaxation time and E_A is the anisotropy energy. The blocking temperature, T_B, is the temperature at which the anisotropy energy (E_A equal to $K_A V$ for uniaxial anisotropy and $K_1 V/4$ for cubic anisotropy) is comparable to the thermal energy $k_B T$, where $k_B =$

$1.386 \cdot 10^{-23}$ J/K is the Boltzmann constant and T is the temperature in Kelvin. Above this temperature, the particles are superparamagnetic and, in the absence of any external magnetic field, their overall magnetic moment is randomized to zero due to thermal relaxation.

For magnetic nanoparticles, predominantly three methods are used for the determination of the anisotropy constant: Mössbauer spectroscopy [14], magnetization measurements [15,16] and rotational hysteresis loss analysis [17]. As pointed out by Moumen et al. [14], these methods can give significantly different results. Although in these methods the anisotropy constant is taken to be constant, it should be realized that it has a temperature- and size-dependence. For cubic crystals with large anisotropy a temperature dependent method has been developed that uses the measurement of the torque for directions of the applied field near the direction of easy magnetization [18]. For bulk cobalt ferrite the following relation was found:

$$K_1 = 19.6 \cdot 10^5 \exp(-1.9 \cdot 10^{-5} T^2) \ (J/m^3) \tag{1.4}$$

which is also known as the Brükhatov-Kirensky empirical relation. Besides this variation with temperature, for nanoparticles the anisotropy constant is also expected to vary with the size. Moumen et al. [14] have found the following size dependence:

$$K_1 = \left(4.5 + \frac{55}{d^2}\right) \cdot 10^5 \ (J/m^3) \tag{1.5}$$

with d representing the diameter of the (spherical) nanoparticles in nm.

1.2 Magnetic nanoparticle assemblies

When the nanoparticles are brought close to each other, interactions between them change the behavior and the properties of the ensemble. Fig. 1.1 illustrates the main forces and the distances at which they dominate the interparticle interaction.

Exchange coupling is a short-range interaction that, because of the surfactant layer that covers the particles, can be neglected. The dipole-dipole energy E_{dd} originates in the interaction between two magnetic moments $\mathbf{m}_1$ and $\mathbf{m}_2$ at a distance $\mathbf{r}$ from one another:

$$E_{dd} = \frac{\mu_0}{4\pi} \frac{3\mathbf{m_1} \cdot (\mathbf{m_2} \cdot \mathbf{r})\mathbf{r} - (\mathbf{m_1} \cdot \mathbf{m_2})r^2}{r^5} \tag{1.6}$$

where μ_0 is the permeability of vacuum and $r = |\mathbf{r}|$.

For two dipoles (with equal magnetic moments, m) in the head-to-tail configuration, the dipole-dipole energy per particle amounts to:

$$|E_{dd}/par| = \frac{\mu_0 m^2}{4\pi r^3} \tag{1.7}$$

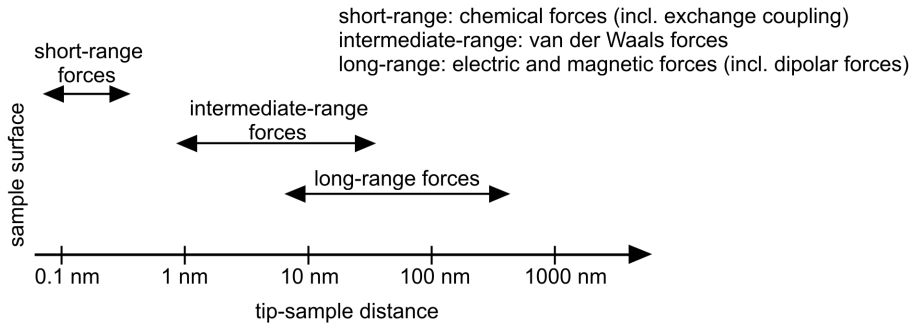

Figure 1.1: *The main forces acting in vacuum and the distances where they dominate the interparticle interaction.*

When this energy is significantly (at least three times [19]) larger than the thermal energy (k_BT), an ensemble of dipoles form (in the absence of external magnetic fields) dipolar chains and flux-closure rings, as predicted by Chantrell et al. [20] and experimentally shown by Klokkenburg et al. [21].

Three-dimensional (3D) systems of nanoparticles (like ferrofluids and powders) have been intensively studied with a variety of techniques as (zero) field cooled magnetization, Mössbauer spectroscopy, ac susceptibility, and hysteresis curves [22–24]. The studies focus on the macroscopic magnetic properties of the systems [25–27] as well as on the interactions between the nanoparticles [28]. The behavior of the magnetic properties of 3D systems of ferromagnetic nanoparticles has been studied also theoretically and by employing numerical calculations. Monte Carlo models have been used to investigate the evolution of magnetic properties as a function of the magnetic state [29–31]. Mørup et al. have developed a model to explain the experimental observation of the dependence of the superparamagnetic relaxation on the interparticle interaction strength [32].

Recently, high-quality two-dimensional (2D) assemblies of magnetic nanoparticles have been prepared by drop casting and by the Langmuir-Blodgett technique [15, 34]. For a system with a small magnetic moment per dipole, the role of dipole-dipole and van der Waals interactions on the formation of structures in 2D systems has recently been investigated. Lalatonne et al. [19] studied the arrangement of 10-nm diameter maghemite (γFe_2O_3) nanocrystals considering the two interactions. They have reported that the van der Waals interaction and the dipole moment of clusters of particles under external magnetic field were responsible for the formation of chain-like structures. Also Kortright et al. [35] studied the arrangement of magnetic moments in 2D systems. They found that the higher anisotropy system has randomly oriented magnetic moments while the lower anisotropy system shows collective behavior consistent with the dipole-dipole interactions. Neither sample exhibits domain formation. Sun et al. [36] reported memory effects in the dc magnetization

and magnetic relaxation that support the existence of spin-glass-like behavior in interacting 2D systems of magnetic nanoparticles.

The differences between 3D and 2D systems have also been studied. Poddar et al. [33] have compared three systems of Fe_3O_4 nanocrystals: one with non-interacting particles (NIP), one with two dimensional (2D) arrays and a quasi 3D assembly. They concluded that the behavior of the NIP system is dominated by internal anisotropy energy while the 2D and the quasi 3D samples show blocking of the moments due to dipole-dipole interactions. Decreasing the dimensionality of the system from three to two, an increase in the blocking temperature (T_B) and an increase in the low temperature remanent magnetization (M_R/M_S) have been observed. For both 2D and 3D systems spin-glass behavior has been observed at low temperatures. The observed relaxation times fit either a power low dependence or an exponential slowing down relation.

Advances in scanning probe techniques makes it possible to study the magnetic behavior of individual or quasi-individual nanoparticles in an assembly. In a recent Magnetic Force Microscopy (MFM) study of a 2D assembly of spherical 12 nm Co nanoparticles [37], the existence of correlated areas with diameters of at least ten nanoparticles was demonstrated and attributed to dipolar coupling between the nanoparticles. The configuration of the magnetic moments in these correlated regions however was not elucidated. When we started the investigations presented in this thesis, to our knowledge, this MFM study on the interaction between magnetic nanoparticles was the only one available in literature.

1.3 This thesis

This thesis involves a fundamental study of 2D arrays of magnetic nanoparticles using non contact-Atomic Force Microscopy (nc-AFM), Magnetic Force Microscopy (MFM), and Atomic Force Spectroscopy (AFS). The goal is to acquire a better understanding of the interactions between magnetic nanoparticles and the resulting configuration of their magnetic moments.

The nanoparticles studied are 20-nm-diameter magnetite (Fe_3O_4) and 21-nm-diameter cobalt-ferrite ($CoFe_2O_4$) nanoparticles, capped with oleic acid and oleylamine, deposited using the drop-casting technique on HOPG (Highly Oriented Pyrolytic Graphite). Small magnetite nanoparticles are known to be superparamagnetic at room temperature. As the temperature decreases the magnetocrystalline anisotropy energy, E_A, increases but remains small. The cobalt-ferrite nanoparticles, on the other hand, have small anisotropy energy at room temperature but, as for bulk (see relation 1.4), it is expected to increase significantly as the temperature decreases. As will be illustrated, we have exploited this behavior to study the interparticle interactions.

The thesis is organized as follows. The *second chapter* gives a description of the experimental setup and the instruments used to obtain our experimental results. The basic principle of AFM, MFM and AFS will be explained and measurements performed on a test sample are presented. We will present the preparation method of the nanoparticles and sample as well as other essential information about nanoparticles and tips. We will also explain the theoretical model developed to simulate the MFM images and the AFS curves.
In the *third chapter* we present the principles of the Monte Carlo model that we developed to perform calculations of the arrangements of the magnetic dipole moments of the nanoparticles. The total energy of the system has two main contributors: the dipole-dipole energy and the anisotropy energy. The model systems we have considered consist of two-dimensional assemblies of nanoparticles, unable to move but with magnetic moments able to rotate. The tip consists of a magnetic moment oriented towards the sample. When the configurations of moments have been determined, MFM images and spectroscopy curves can be simulated.
The *fourth chapter* presents the experimental and simulated results for the 20-nm magnetite Fe_3O_4 nanoparticles. The experiments performed at low temperatures reveal the influence of the tip on the arrangement of the moments. However, we will also show that, with the tip at the edge of the island of nanoparticles, its influence on the arrangement of moments is significantly less. The (repulsive) interaction at the edge of the island is ascribed to the interaction between the dipole moments which causes their blocking. Numerical simulations are presented to support this interpretation and to show the formation of flux-closure structures.
The fifth chapter presents our results obtained with the 21-nm cobalt-ferrite $CoFe_2O_4$ particles. We present experimental results and numerical simulations with the sample at different temperatures. It is shown that at low temperatures the blocking of the moments is strong enough to prevent any influence of the stray field of the tip. Simulations are presented to support the experimental observations and to show that areas with short-range order are present in the configuration of the moments.
Chapter six finally presents the general conclusions of this thesis.

2 Experimental

The first part of this chapter presents the setup in which the experiments were performed. The most important techniques available in the setup are atomic force microscopy (AFM), magnetic force microscopy (MFM), and atomic force spectroscopy (AFS). They are in detail discussed in the second section of this chapter. In force microscopy, the probe (also called tip) is attached to a cantilever. When close to a sample, the interactions between probe and sample cause the cantilever to deflect. While the probe scans the sample, the deflection of the cantilever is detected and the topography or the magnetic field of the sample can be measured. As an illustration of the operation of the setup, results obtained on a test sample are presented and discussed. The last part of the chapter addresses the interpretation of the signal (frequency shift) in terms of the force exerted on the tip. Since the amplitude is an important parameter in the calculation of the force, a method of determination of the amplitude is presented.

2.1 Experimental setup

All experimental results presented in this thesis were obtained operating an ultra-high vacuum (UHV) variable-temperature (VT) AFM/STM Omicron instrument (Fig. 2.1). The instrument contains two main independent chambers: the preparation and the analysis chamber.

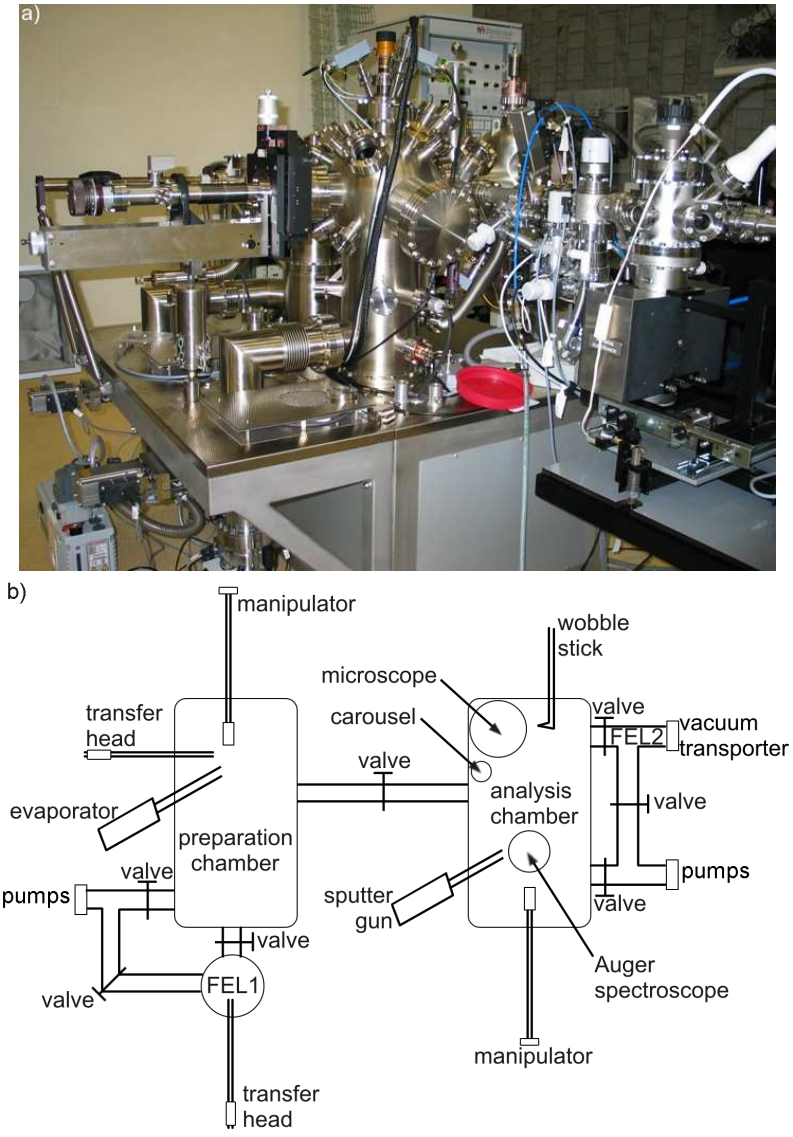

Figure 2.1: *(a) Photograph of the setup, taken from the lower right corner relative to the schematic. (b) Schematic overview of the setup with the main components: the preparation chamber and the analysis chamber with the microscope. The evaporator, sputter gun, and Auger microscope do not play a role in the measurements presented in this thesis.*

The main chambers are each pumped by a turbo-molecular pump in com-

bination with a two-stage rotary pump (starting at atmospheric pressure), an ion getter pump and, for lower pressures, a titanium sublimation pump (TPS). The pressure in the chambers is around $5 \cdot 10^{-11}$ mbar. To help reaching this low pressure fast, the system was baked in a controlled manner, by controlling the temperature, time and the increase/decrease of temperature per minute.

The samples and probe holders are introduced into the system via the fast entry locks (FEL1 and FEL2), which can be vented independently of the main chambers and pumped fast to a low pressure due to their small dimensions. Furthermore, FEL2 was designed to accommodate a vacuum transporter, used to transport samples from one setup to another without breaking vacuum. The sample plates as well as the tip holders are transported in the system by manipulators, transfer rods and a wobble-stick. The manipulator has a tungsten filament used to anneal samples up to 1170 K and the option to directly heat the sample by applying a current through this sample. It has also a chromel-alumel thermocouple for measurement of the temperature. The wobble-stick is a double action pincer used to load/unload samples on/from the manipulator, microscope, and the carousel (a device with 12 positions to store samples and tips).

The microscope

To obtain high-resolution imaging a high-quality vibration decoupling system is required (Fig. 2.2a). The microscope is suspended by four springs protected by surrounding columns (with a resonant frequency of 2 Hz) that, together with a non-periodic eddy-current damping mechanism, damp external oscillations. The base plate of the microscope is surrounded by a ring of copper plates that come down between permanent magnets. The suspension system can be blocked to allow for manipulation of sample/probe holders and cooling block.

The geometry of the tip/sample system is presented in Fig. 2.2b. While a sample is electrically grounded via the electrical contacts or the cooling block, a voltage can be applied to the tip via the scanner tube. The piezoelectric scanner moves in three directions and covers a positioning range from micrometers to angstroms needed to approach the sample and measure with atomic resolution. Note that since the piezoelectric element is sensitive to temperature variations, the scanner tube is protected by a radiation shield.

The cooling block is connected via a copper braid to a (liquid helium) continuous flow cryostat to allow to reach sample temperatures down to 25 K. Together with an integrated counter-heating element, a precise way of temperature control is achieved. The temperature at the cooling block is measured using a silicon diode with a sensitivity of ± 1 K below 100 K and $\pm 1\%$ above 100 K[1]. The difference in temperature between the cooling block and the sam-

[1] Values specified by the manufacturer.

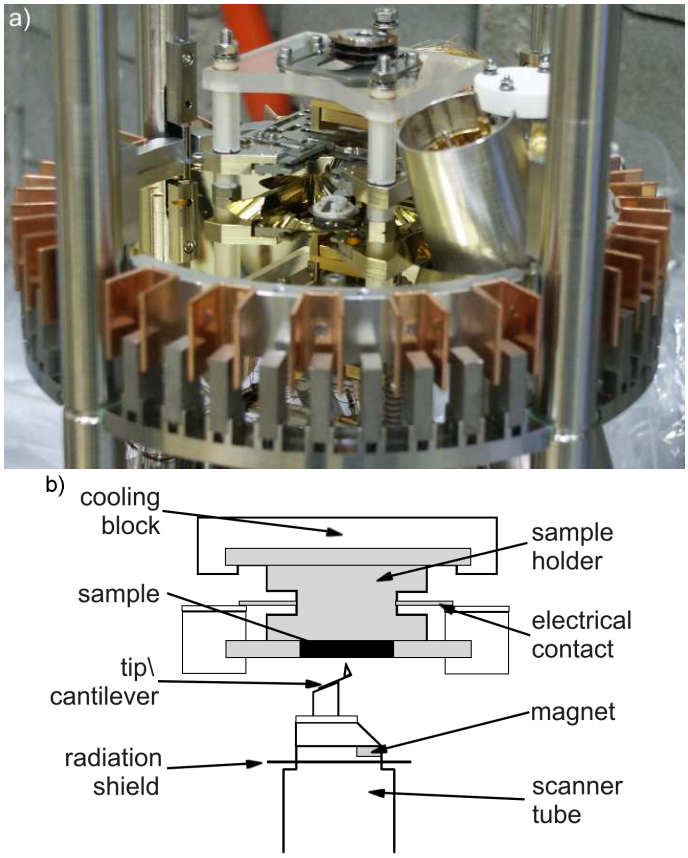

Figure 2.2: *(a) Photograph of the microscope with the vibration decoupling system and (b) schematic of the microscope stage. The tip is mounted on the scanner tube, the probe pointing upwards, able to move three-dimensional. The sample is fixed, clamped to the stage.*

ple depends on the absolute temperature, on the type of sample holder and on the sample mounting. For the specially designed cooling sample holders, the temperature difference is in between 1 K and 10 K. After reaching thermal balance, temperature stability of about 0.1 K is achieved. The values of the temperature given in this thesis are measured at the cooling block.

2.2 Atomic Force Microscopy

In this thesis, Atomic Force Microscopy is operated in non-contact mode (nc-AFM) [38]. Its basic principle is illustrated in Fig. 2.3. A sharp tip (probe) is attached to a cantilever mounted on a scanning device known as the *xyz*-scanner that allows three-dimensional positioning with subatomic precision. The relative position of the cantilever is determined by the deflection sensor. The cantilever is oscillating at or close to its resonant frequency. When the

distance between tip and sample is sufficiently small, the sample exerts a force F_{ts} on the tip that modifies its eigenfrequency. This frequency shift is used as feedback signal in the z-feedback loop (for more details see **Operation modes**).

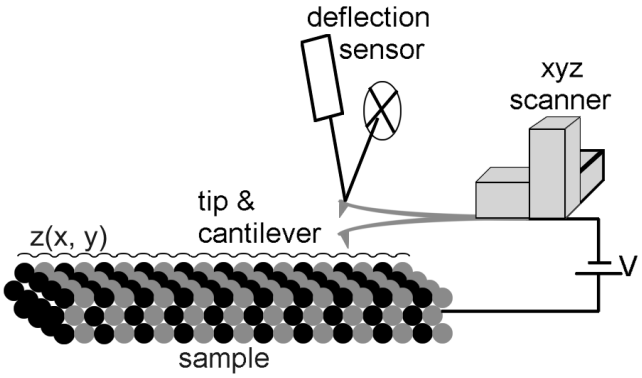

Figure 2.3: *Schematic view of an atomic force microscope. A very sharp tip is attached to a cantilever oscillating close to its resonant frequency. The cantilever is moved 3D by a xyz-scanner to scan the sample. The movement on the cantilever is monitored by the deflection sensor.*

Deflection sensor

One of the most commonly used methods for detection of the cantilever movement is optical detection [39, 40]. To avoid heating of the cantilever, an infrared laser diode is used as light source. Using a system of optical fibers and rotating mirrors, the laser beam is positioned on the back of the cantilever. The reflected beam is then positioned in the center of the detector, a four quadrants position sensitive detector (PSD). The difference signal between top and bottom quadrants contain the topographic information while the difference between left and right quadrants originates in lateral forces that twist the cantilever sideways during measuring.

Cantilever and tip

The cantilever with the tip at its end is the crucial sensing component responsible for the quality of the AFM images. They come in great variety, suitable for different applications.

We used $Nanosensors^{TM}$ probes, manufactured from highly doped, single-crystal silicon material that leads to highly conductive cantilevers (to avoid electrostatic charging). For non-magnetic measurements, we used Si probes with a resonant frequency of 300 kHz (suitable for fast scans) and a spring constant of 35 N/m. For the magnetic measurements, the probes we used had a resonant frequency of about 70 kHz and a spring constant of 2.8 N/m (for high sensitivity). It has a 40-nm Co-Cr-alloy magnetic coating, with a remanent

magnetization of $3 \cdot 10^5$ A/m and a relatively high coercivity of $2.4 \cdot 10^4$ A/m.[2] The high coercivity insures that the moment of the tip is not rotated in the magnetic field of the sample. We are not able to experimentally determine the effective magnetic moment of the tip. In the simulations discussed in this thesis, we used an estimated value of $2.5 \cdot 10^{-17}$ Am^2, a value similar to the ones reported in literature for a similar tip [41].

Sample

The first step in the preparation of a sample is the synthesis of nanoparticles. Sun et al. [42, 43] reported a novel method of preparing monodisperse magnetic nanoparticles. Klokkenburg et al. [21] and Viota et al. [44] used a modified method to prepare magnetite (Fe_3O_4) and cobalt-ferrite ($CoFe_2O_4$) magnetic nanoparticles, respectively. The particles were characterized as follows.[3] For stabilization, the particles are covered with surfactant: oleic acid and oleylamine. A surfactant layer thickness of 2.1 nm was determined using small-angle neutron scattering (SANS) and agrees well with the length of one surfactant molecule. Using transmission electron microscopy (TEM), the size of the particles was determined to be (excluding the surfactant layer) (20.0 ± 2.4) nm for Fe_3O_4 and (21.0 ± 2.7) nm for $CoFe_2O_4$ and the polydispersity to be less than 8%. In Fig. 2.4, TEM images of the two systems of nanoparticles are presented.

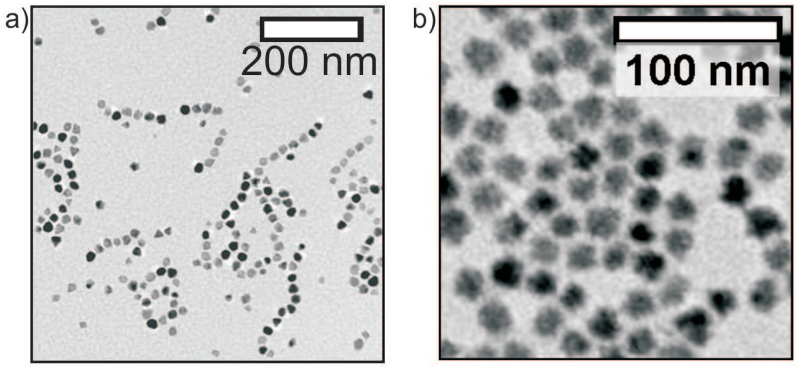

Figure 2.4: *(a) Cryo-TEM image of 20-nm magnetite particles. (b) TEM image of 21-nm cobalt-ferrite particles.*

Infrared spectroscopy (IR) was used to confirm the composition of the magnetite particles: the particles are iron oxide, most likely magnetite with a 5% volume fraction undefined iron oxide. Using X-ray diffraction (XRD) and energy dispersive X-ray spectroscopy (EDX) it was established that the

[2] Values specified by the manufacturer.

[3] The nanoparticle characterization was done in the Van 't Hoff Laboratory for Physical and Colloid Chemistry, Utrecht University, The Netherlands.

cobalt-ferrite particles have a cubic spinel structure and the atomic ratio Co:Fe is 1:2.

The magnetic moment m was determined by the initial magnetization curve using the Langevin equation for diluted solutions:

$$m = \frac{\chi_i}{M_{sat}} \frac{3k_BT}{\mu_0} \tag{2.1}$$

where χ_i is the initial susceptibility, M_{sat} is the saturation magnetization of the sample, k_BT is the thermal energy, and μ_0 is the permeability of vacuum. Its value is $1.55 \cdot 10^{-18} Am^2$ for Fe_3O_4 and $1.1 \cdot 10^{-18} Am^2$ for $CoFe_2O_4$. This gives a magnetic diameter d_M of 18.4 nm and 17.0 nm, respectively if we consider the particles spherical and $m = \frac{4\pi}{3}\left(\frac{d_M}{2}\right)^3 \cdot m_s$, where m_s is the bulk magnetization value. The magnetic diameters being only slightly smaller than the core diameters confirms that these nanoparticles have only a single magnetic domain. The magnetic diameters are smaller than the core diameters (without the surfactant layer) probably due to an oxide (non-magnetic) layer and to reorganization of the magnetic moments at the surface.

The particles were dispersed in decalin and/or hexane. The samples were subsequently prepared by using the drop-casting method, which means placing a droplet of solution on an atomically flat substrate (Highly Oriented Pyrolytic Graphite, HOPG). After drying, the particles were inspected using tapping mode AFM. Typical results showed monolayered islands of nanoparticles.

Operation modes

Nc-AFM (also known as dynamic force microscopy) can be operated in amplitude-modulation (AM) or in frequency-modulation (FM) mode. In FM-AFM, an actuator drives the cantilever at a fixed amplitude, A. When close to the sample, tip-sample interactions cause the resonant frequency (and, therefore, the cantilever effective spring constant) to change. The feedback signal is the frequency shift (df), representing the difference between the eigenfrequency of the cantilever when close to the sample and at large distance ($df = f - f_0$).

Analyzing the cantilevers motion one can understand the function principle of FM-AFM [45]. Considering the cantilever as a damped oscillator externally driven by a sinusoidal excitation with amplitude A_{drive} and frequency f_{drive}, the cantilever will oscillate with the amplitude:

$$A = \frac{A_{drive}}{\sqrt{\left(1 - \frac{f_{drive}^2}{f^2}\right)^2 + \frac{f_{drive}^2}{f^2 Q^2}}} \tag{2.2}$$

where Q is the quality factor of the cantilever. The phase difference between

driving and resulting signal is:

$$\varphi = \arctan\left(\frac{f_{drive}}{Qf\left(1-\frac{f_{drive}^2}{f^2}\right)}\right) \tag{2.3}$$

In the general case of a closed feedback-loop (the measured signal is used to oscillate the cantilever), the driving frequency cannot be chosen freely but depends on the eigenfrequency of the cantilever, the phase shift and the probe-sample interactions. For a controlled feedback (that will ensure a constant amplitude independent of external interactions), the phase angle must be $\pi/2$ (see equations 2.2 and 2.3).

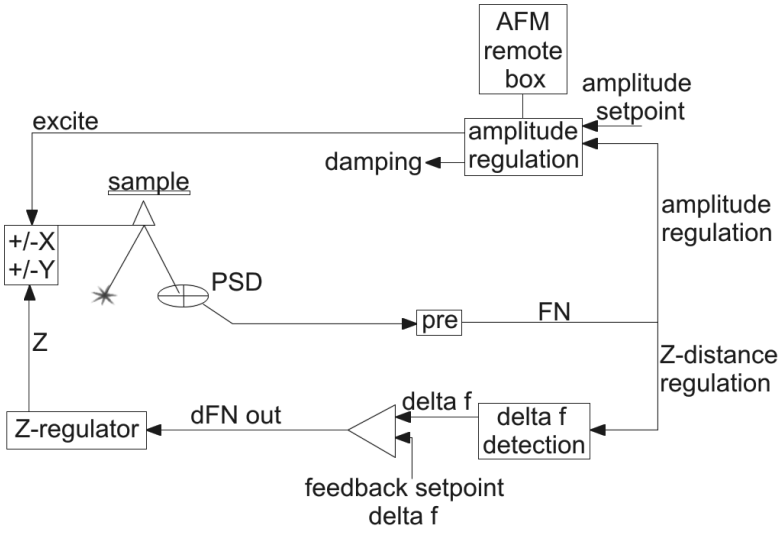

Figure 2.5: *Diagram of the FM nc-AFM feedback loop. We used the notations: pre for preamplifier, FN for the output signal from the preamplifier (it derives from difference between top and bottom quadrants of the PSD), and dFN is the output signal used to move the cantilever in the z-direction.*

A circuit as the one shown in Fig. 2.5 is used to oscillate a cantilever in FM-mode at a constant frequency shift (the feedback-set), while measuring the corrugation of the sample. The tip scans the sample in the *xy* direction. In each point, the movement of the cantilever is detected on the PSD. The signal is filtered (to cut off the noise), amplified and divided into two in order to feed two loops: one responsible for the excitation of the cantilever (amplitude regulation loop) and the other responsible for the movement of the tip in the z direction at constant frequency shift (z-distance regulation). On the first branch the measured signal is compared with the amplitude setpoint, yielding the amplitude error signal (*damping channel*). The damping channel is a measure of the amount of energy put into the cantilever's oscillation,

since the dissipative forces between tip and sample give rise to energy loss during each oscillation cycle. The second branch of the signal is used to obtain $\delta df = df_{measured} - df_{feedback-set}$ (the *frequency shift channel* or the *error channel*). Up to a constant, δdf is the frequency shift measured in each point, before the scanner tube adjusts the tip-sample distance so that $df_{measured}$ equals $df_{feedback-set}$. After this adjustment, the movement of the scanner tube in the z direction will give the *topography channel*.

In the *constant frequency shift mode*, images are created by scanning the tip in the *xy* plane and recording the z position required to keep the feedback signal constant. The scanning is performed in a raster fashion with a fast and a slow scanning direction. A computer controls the scanning of the surface in the *xy* plane while a 3D image *z(x, y; df=const.)* is created.

Magnetic Force Microscopy (MFM) [46] is a special mode of operating nc-AFM, capable of obtaining high resolution 2D images of the stray magnetic fields: using a magnetic tip to probe a magnetic sample, the cantilever is lifted to a certain distance (see for more details next section) to measure long-range magnetic interactions, in terms of frequency shift as in nc-AFM. The tip scans the surface and a 2D image *df(x, y; z=const.)* is obtained.

Atomic Force Spectroscopy (AFS) is another mode of operating in nc-AFM. Instead of scanning the surface, the tip measures in a specific location (x_0, y_0) the frequency shift as function of a free parameter. We measured in our experiments df as function of tip-sample distance (z-spectroscopy or z-curves) and as function of the tip-sample voltage difference (V-spectroscopy or V-curves).

2.3 Experimental procedure

In the experiments presented in this thesis, nc-AFM in constant frequency shift mode, MFM mode and AFS were used to obtain information about the sample surface.

It is important to note that in this section we are discussing forces. The arguments however will remain valid for the frequency shift (see Section 2.5 for an interpretation of the frequency shift in terms of force).

As illustrated in Fig. 1.1, electrostatic forces are present at large distances, together with magnetic forces. By analyzing the experimental results, it is difficult to distinguish between them since they have similar dependences on distance. To minimize the electrostatic forces we applied an appropriate voltage V_{appl} between tip and sample. This voltage corresponds to the contact potential difference, which we measured using AFS.

The electrostatic force can be approximated as:

$$F = \frac{1}{2}\frac{\partial C}{\partial z}V^2 \tag{2.4}$$

where C is the effective capacitance between tip and sample, z is the tip-sample distance and V is the tip-sample voltage difference. The functional dependence of the force is shown in Fig. 2.6.

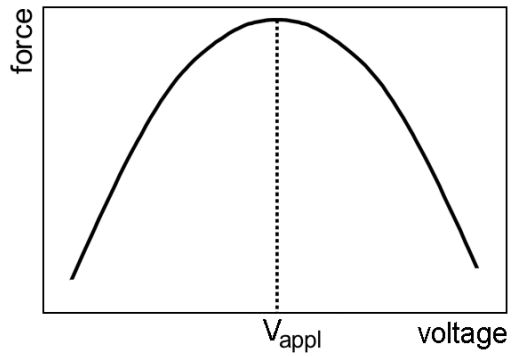

Figure 2.6: *Force vs. voltage curve. Note that the forces are attractive, thus they have negative sign.*

V_{appl} is the voltage corresponding to the maximum of the curve, thus to minimum interaction, thereby minimizing the electrostatic forces.

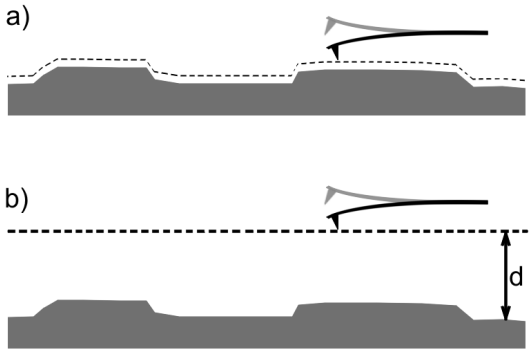

Figure 2.7: *Schematic diagram of the two different operating modes in nc-AFM: (a) constant frequency shift mode; (b) MFM mode.*

The next step is to measure the sample topography. As illustrated in Fig. 2.7(a), in *constant frequency shift mode*, the image is generated by maintaining a constant frequency shift by adjusting the tip-sample separation (as discussed in the previous section). The probe-sample distance is relatively small so the measured forces are predominantly caused by van der Waals interactions (as illustrated in Fig. 1.1); the image will constitute the topography of the sample.

Subsequent to measuring the sample topography, the MFM image is created in the so-called plane subtraction mode. In this mode the tip is scanned across the surface, parallel to the sample plane at a predetermined height d as shown in Fig. 2.7(b) yielding a 2D image *df(x, y, z=const.)*. The distance d has to

be carefully chosen; too small and the contribution of van der Waals forces will be large or even probe crashes may occur, too large and the magnetic signal-to-noise ratio will be poor.

By performing z-spectroscopy in specific locations, one can obtain detailed information about the nature and the range of the interaction, and an estimate of the optimum distance (d) at which MFM images will give the best results.

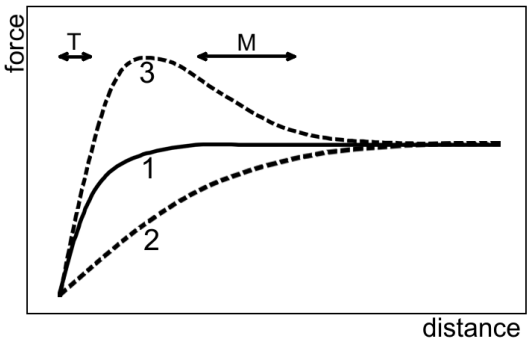

Figure 2.8: *Force vs. distance curves. T and M correspond to the intervals where topography and MFM images should be taken, respectively.*

As we will discuss in the next section, we found that the interactions lead to 3 characteristic z-spectroscopy curves (Fig. 2.8). Curve 1 exhibits relatively short-range interactions that can be ascribed to van der Waals forces between tip and sample. Curves 2 and 3 show longer-range interactions that can be ascribed to attractive and repulsive magnetic forces, respectively. They have, at small distances, a strong contribution from van der Waals forces. The "topography" images may, on the other hand, contain small contributions from magnetic forces. The smaller the tip-sample distance (the larger the feedback-set), the larger the contribution from van der Waals forces. At very small distances, instabilities or tip crashes may occur, thereby possibly damaging the tip.

2.4 Results on a test sample

As a test for the setup and the experimental procedure, we performed experiments on a computer hard disk. The hard disk has a well-known magnetic structure [47]; the information on the hard disk is stored in terms of bits - microscopic elongated areas with a local magnetic moment that alternates from one area to another. Hard disks are also easy to study with MFM because they have a large coercivity, so rotation of the magnetic moments on the sample in the magnetic field of the tip does not occur.

We carried out a complete set of measurements (topography, MFM, and spectroscopy) on a piece of a hard disk. We first performed V-spectroscopy to

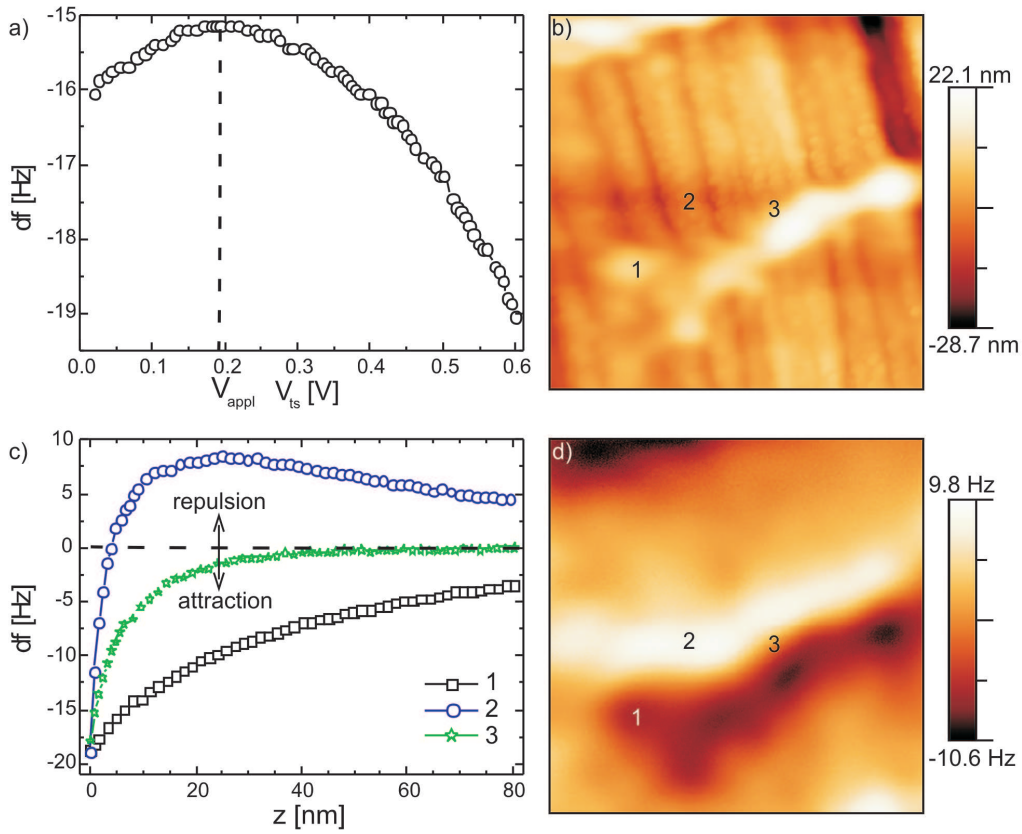

Figure 2.9: *Measurements on a hard disk with a density of* $200 Mbit/cm^2$. *(a) V-spectroscopy. (b) AFM image of a 1 x 1* μm^2 *area taken at -15 Hz feedback-set. (c) z-spectroscopy taken at the positions indicated in (b) and (d). Note that 0 nm corresponds to the -15 Hz feedback-set. (d) The MFM image of the same area as (b) taken at 50 nm with respect to the -15 Hz feedback-set.*

find V_{appl} (see Fig. 2.6). A typical result is presented in Fig. 2.9(a). In this case a voltage of 0.19 V was applied to the tip.

Subsequently, a topography measurement was performed (Fig. 2.9(b)). Figure 2.9(d) represents the MFM image of the same area on the hard disk taken at a distance of 50 nm with respect to the -15 Hz feedback-set. It shows one elongated structure, partially attractive and partially repulsive. The contrast in the image is relatively large, of about 20 Hz. Since a small feedback-set was used, a rather strong magnetic signal is present in the topography measurement (Fig. 2.9(b)). To make distinction between topography and magnetic structures, one should compare fig. 2.9 (b) and (d) and the features disappearing in the MFM image represent the topography.

Three typical distance spectroscopy curves are shown in fig. 2.9(c); they were taken in the positions indicated in fig. 2.9(b) and (d). Curve 1 shows attraction, curve 2 repulsion for distances larger than a few nanometers. The

forces are long range (up to at least 100 nm) and have a magnetic origin. For small distances, the van der Waals interaction between probe and sample becomes predominant, resulting in strong attraction. Since a hard disk contains a magnetic thin film, it is virtually impossible to obtain spectroscopy curves showing only van der Waals interactions. Curve 3, taken in a transition regime between repulsion and attraction, seems to show minimal magnetic interaction.

We present also another set of measurements in which a larger feedback-set was used, resulting in a smaller contribution of the magnetic forces in the topography image. They are presented in Fig. 2.10. Fig. 2.10 (a, b, and c) represents the topography of the sample in topographical, error and damping channels, respectively (see Section 2.2). The topography shows features elongated in the x' direction and others, less visible, along the y' direction. The signal in the error channel shows the same features with a higher sensitivity. The damping channel shows clear features in the y' direction as well. Fig. 2.10(d) shows the MFM image of the same area on the sample, taken at a distance of 60 nm. Elongated structures along the y' direction are clearly visible.

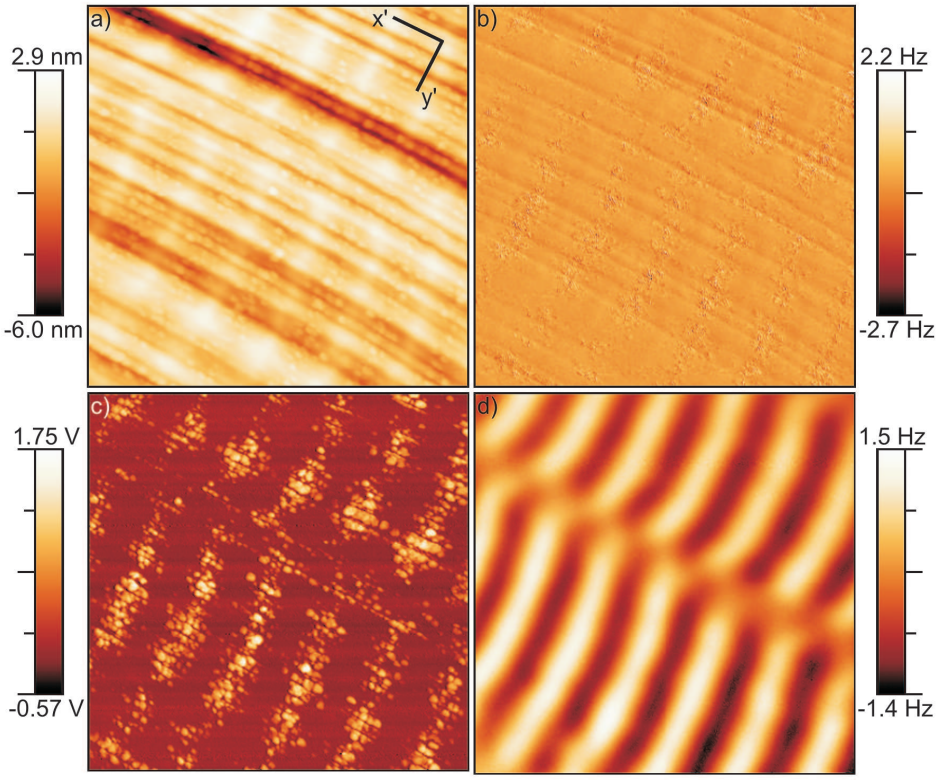

Figure 2.10: *AFM image of a 1.7 μm^2 area on a hard disk of 500 $Mbit/cm^2$ taken at a feedback set of -64.1 Hz; (a) topography channel, (b) error channel, (c) damping channel. (d) MFM image of the same area taken at a distance d = 60 nm with respect to the distance at which df = -64.1 Hz.*

The information one can obtain inspecting these images is the following:

- The structures along the x' direction are due to van der Waals forces since they disappear at large distances. They represent the real topography of the sample.
- The structures in the MFM images, along the y' direction originate in the interaction of the magnetic moment of the tip with the stray field of the magnetic domains written on the hard disk. Supposing that the orientation of the magnetic moment of the tip is towards the sample, the dark and bright areas represent stray fields going-in and coming-out of the sample, respectively.
- Studying the magnetic contributions in the topography and in the MFM image, one notices that white areas in the topography image correspond to black areas in the MFM image. The interpretation is quite straightforward: when the tip is close to the sample it senses attractive forces and it will retract (away from the sample), thus white in topography. At 60 nm away from the sample, the tip will sense the same attractive forces, thus black in the MFM image.
- Similarly, in between the white magnetic features in Fig. 2.10 (a), repulsive magnetic forces act on the tip. The tip therefore needs to approach the sample to reach the feedback-set. The damping channel shows in these areas that strong non-conservative forces act on the tip. Because in these areas the tip is so close to the sample, the lateral resolution increases and individual grains of the hard disk are visible.

For a sample as the hard disk, where the magnetic domains have an elongated shape and are aligned in the direction perpendicular to topographical features, it is quite straightforward to interpret the images and draw conclusions about the nature of the interactions. For other samples, spectroscopy is needed to give essential information about the nature of the interactions. Furthermore, spectroscopy curves can be interpreted in terms of forces.

2.5 Interpretation of frequency shift in nc-AFM

The frequency shift has a well-defined significance. In nc-AFM the cantilever is excited close to or at its eigenfrequency, f_D (Fig. 2.11(a)). When the tip is close to the sample, because of tip-sample interactions the cantilever will change its effective resonant frequency. Imposing the condition that the amplitude is constant (we neglect dissipative forces), the frequency shift will be $df = f_D - f'_D$ (Fig. 2.11(b)).

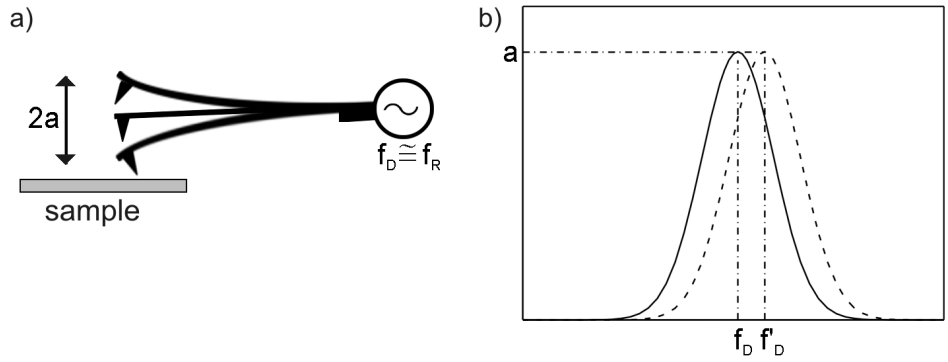

Figure 2.11: *(a) In nc-AFM the cantilever is oscillating close to or at its resonant frequency. (b) As the tip interacts with the sample the resonant curve shifts.*

To interpret the frequency shift in terms of forces is difficult. There are two ways of calculating the frequency shift as function of force: using canonical perturbation theory and the Hamilton-Jacobi formalism by F. Giessibl [48] and using the least-action principle by U. Dürig [49]. The methods give the same final result regarding the relation between frequency shift and force.

Giessibl considered the Hamiltonian of the harmonic oscillator:

$$H_0 = \frac{p^2}{2m} + \frac{kq\prime^2}{2} \tag{2.5}$$

where $p = m\dfrac{dq\prime}{dt}$ and the unperturbed motion is given by $q\prime(t) = a\cos(2\pi f_0 t)$.

With a perturbation caused by tip-sample interactions $F_{ts} = -\dfrac{\partial V_{ts}}{\partial q\prime}$, the perturbation Hamiltonian becomes $\Delta H = V_{ts}$.

Using the Hamilton-Jacobi formalism, the momentum p and the deflection q'are transformed to action $J$and angle β that depend on time in the perturbed case. Considering that the motion is still harmonic for the perturbed case, the expression for $df = f - f_0$ becomes:

$$\frac{df\,(z)}{f_0} \;=\; -\frac{1}{ka^2}\,\langle F_{ts} q\prime\rangle \tag{2.6}$$

$$= -\frac{1}{\pi a k}\int_{-1}^{1} F_{ts}(z+a(1+u))\,\frac{u}{\sqrt{1-u^2}}\,du \tag{2.7}$$

$$= -\frac{1}{\pi k a^2}\int_{z}^{z+2a} F_{ts}(v)\,\frac{v-z-a}{\sqrt{(v-z)(2a-v+z)}}\,dv \tag{2.8}$$

where the brackets indicate averaging across one oscillation cycle, *df* is the frequency shift, f_0 is the eigenfrequency of the unperturbed oscillator, a is the oscillation amplitude, k is the spring constant of the cantilever, and z is the tip-sample distance at the lower turning point.

J. Sader et al. [50] proposed a method involving fractional integrals and derivatives to obtain an expression for the force as a function of frequency shift. Based on his work, we have derived mathematical relations between force and frequency shift for every characteristic length scale regime.

Since the force goes to 0 at large distances, it can be written as:

$$F(x) = \int_0^\infty A(\lambda)e^{-\lambda x}d\lambda \tag{2.9}$$

where $A(\lambda)$ is the inverse Laplace transform of F(x). Relation 2.7 can be written as:

$$df(z) = \frac{f_0}{ak}\int_0^\infty A(\lambda)T(a\lambda)e^{-\lambda z}d\lambda \tag{2.10}$$

where $1/\lambda$ is the characteristic length scale of the interaction force (roughly defined as the distance between the minimum of the interaction potential and its inflection point), $T(a\lambda) = I_1(a\lambda)exp(-a\lambda)$ and I_1 is the modified Bessel function of the first kind of order 1. An expression for T(x) is then proposed; $T(x) \simeq cx^d$ where c and d are local constants. For the calculation of c and d and their interpretation we refer to Appendix A.

Relation 2.10 can be written as follows (see Appendix B):

$$df(z) = \begin{cases} \dfrac{f_0 c}{a^{1-d}k}\,\dfrac{1}{\Gamma(-d)}\displaystyle\int_z^\infty \frac{F(u)}{(u-z)^{1+d}}du, & for\ d \in [-0.5, 0) \\ \dfrac{f_0 c}{ak}\,F(z), & for\ d = 0 \\ -\dfrac{f_0 c}{a^{1-d}k}\,\dfrac{1}{\Gamma(1-d)}\,\dfrac{d}{dz}\displaystyle\int_z^\infty \frac{F(u)}{(u-z)^{d}}du, & for\ d \in (0, 1) \\ -\dfrac{f_0}{2k}\,\dfrac{d}{dz}F(z), & for\ d = 1 \end{cases} \tag{2.11}$$

where $\Gamma(x)$ is the Gamma function. Note that for d = -0.5, corresponding to the large amplitude limit (i.e. the amplitude is much larger than the characteristic length scale), the result is identical with the result of Dürig [49]. d=0

corresponds to intermediate amplitude regime where force and frequency shift become proportional. This has been observed experimentally by Ke et al. [51]. d=1 corresponds to the small amplitude limit; the relation of proportionality between df and the derivative of the force with respect to z is well known in literature [52]. The function is continuous in d=0 and d=1. In this form, the relation can be inverted (see Appendix C) to give the expression for the force in each interval:

$$F(z) = \begin{cases} -\dfrac{ka^{1-d}}{f_0 c}\dfrac{1}{\Gamma(1+d)}\dfrac{d}{dz}\displaystyle\int_z^\infty \frac{df(u)}{(u-z)^{-d}}du, & for\ d \in [-0.5, 0) \\ \dfrac{ak}{f_0 c}\,df(z), & for\ d = 0 \\ \dfrac{ka^{1-d}}{f_0 c}\dfrac{1}{\Gamma(d)}\displaystyle\int_z^\infty \frac{df(u)}{(u-z)^{1-d}}du, & for\ d \in (0, 1) \\ \dfrac{2k}{f_0}\displaystyle\int_z^\infty df(u)du, & for\ d = 1 \end{cases} \tag{2.12}$$

Relations 2.7 and 2.8 are well established in literature [48, 49]; they make no assumption about the characteristic length scale or the dependence of the force on tip-sample distance. Relation 2.12, however, has been calculated in the assumption that the function T(x) has a power-low dependence and in its expression the characteristic length scale, λ, appears explicitly. λ is a parameter that could not be determined from our experiments and has different values for van der Waals force and magnetic force. To test if the equation is valid, we have done the following. We have considered three curves that are typical for the experiments presented in this thesis which correspond to van der Waals, repulsive magnetic and attractive magnetic forces. The force has been calculated using relation 2.12, for an amplitude of 8.5 nm (experimentally estimated, see section 2.6) and chosen values for the characteristic length scale: 5 nm for van der Waals forces and 13 nm for magnetic forces. Using the calculated force, the frequency shift was calculated using relation 2.8.

The results are presented in Fig. 2.12. The experimental curves and the corresponding calculated frequency shift curves are similar; therefore we believe that the calculated force curves are good approximations of the actual force curves. The inset of Fig. 2.12(b) and (c) shows the magnetic-repulsive and the magnetic-attractive curves. In the process of calculating the force and df, the magnetic and the van der Waals contributions have to be separated, since for each a specific characteristic length scale is valid.

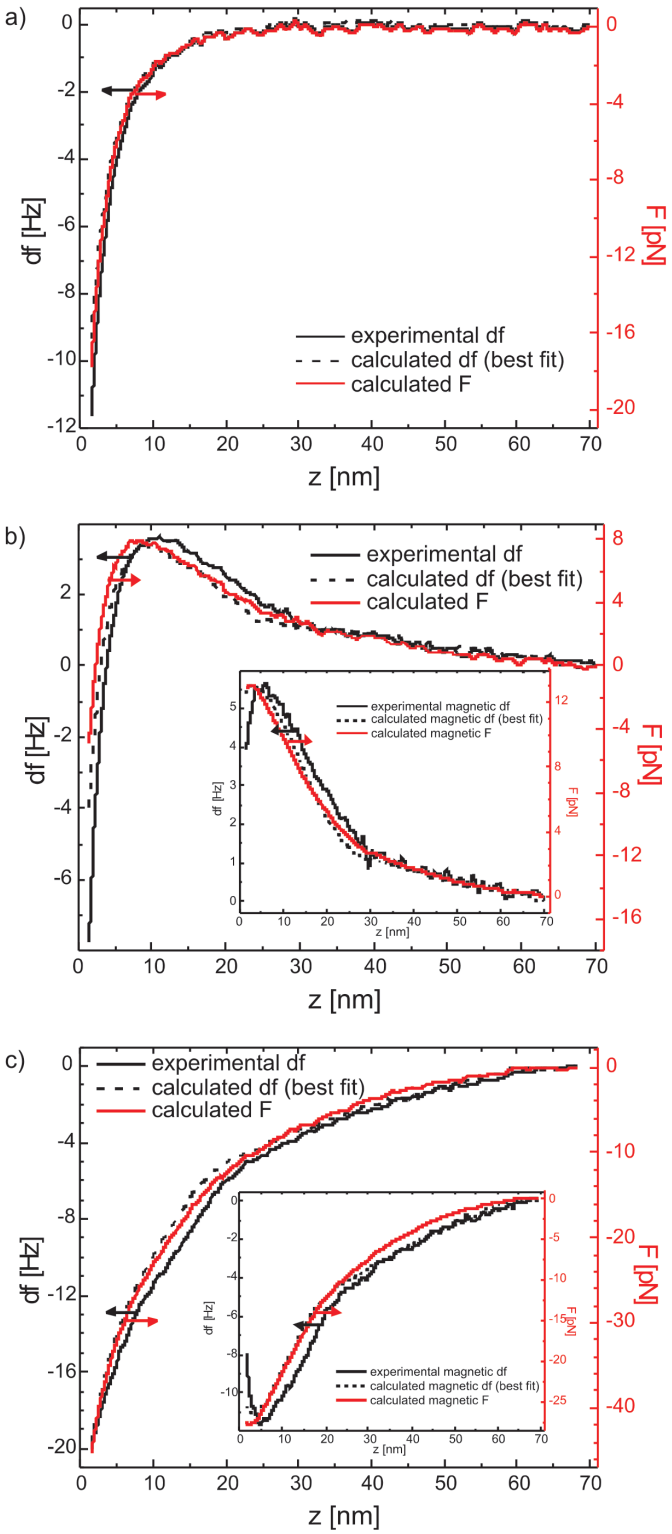

Figure 2.12: *Experimental data, computed frequency shift and corresponding forces for three types of curves. (a) van der Waals, (b) repulsive magnetic, (c) attractive magnetic. The insets show the repulsive and attractive magnetic contributions only.*

The characteristic length scale is a parameter that can only be estimated in a rough way. In order to see how the chosen value influences the results, we are going to use relation 2.12 for the extreme cases $1/\lambda = 20$ nm ($d = 1$, small amplitudes regime), $1/\lambda = 4.8$ nm ($d = 0$, intermediate amplitude), and $1/\lambda = 0.5$ nm ($d = -0.5$, large amplitude regime)[4] and relation 2.8. The regime of large amplitudes can not be reached with amplitudes in the order of 7 to 10 nm and magnetic and van der Waals interactions (with a large characteristic length scale). The results are presented in Fig. 2.13. The curves are calculated for an amplitude of 8.5 nm and the error bars are calculated for a equals 7 nm and 10 nm.

For the van der Waals curve, the relation of proportionality between force and frequency shift holds because the df curve calculated for $d = 0$ is similar with the experimental curve. For the magnetic curves it turns out that none of the approximations are good and the amplitude regime is in between small and intermediate.

Important to note is that for any amplitude regime, positive frequency shift corresponds to repulsive forces and negative df to attractive forces. This result is used in this thesis for the interpretation of the MFM images and spectroscopy curves.

[4]The case of large amplitude regime was considered for completeness purposes only.

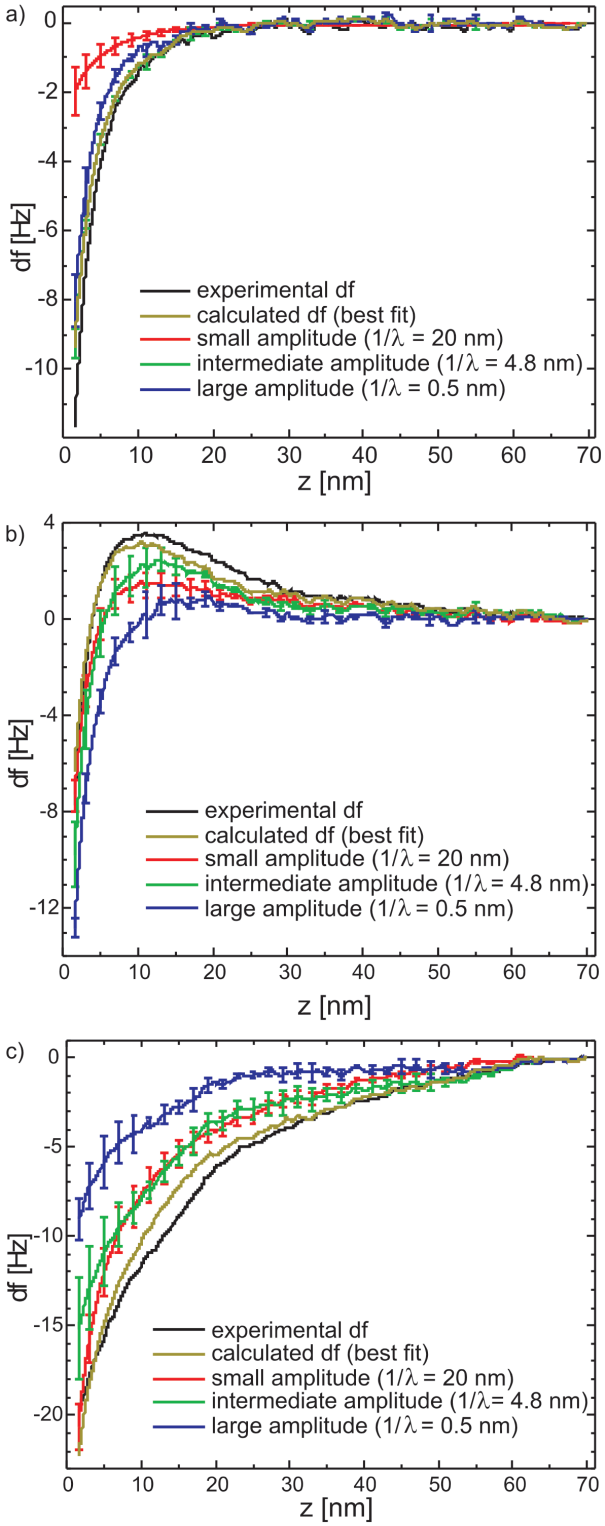

Figure 2.13: *Experimental df curves and computed df curves obtained using the small, intermediate, and large amplitude regimes approximations. (a) Van der Waals, (b) repulsive magnetic, and (c) attractive magnetic. $1/\lambda$ represents the characteristic length scale.*

2.6 Amplitude determination

Equation 2.11 can be written in the form:

$$df(z, a, f_0, k)a^{1-d} = \frac{f_0 c}{k}\Theta(F)(z) \tag{2.13}$$

where Θ is an operator acting on the force. The formulas give known results from literature for the case of small and large amplitude regimes [49, 52] and confirm experimental observations [51]. On the right hand side of the equation we obtain a function that does not depend on the amplitude at which the cantilever is oscillated. This means that in the approximation $d \approx 0$, for two amplitudes a_1 and a_2 with the condition that the turning points z_1 and z_2 are equal, we get:

$$a_1 df_1 = a_2 df_2 \tag{2.14}$$

To keep the turning point constant ($z_1 = z_2$) while the amplitude is changed, the cantilever has to be shifted in the z direction by $\Delta b = b_2 - b_1$, equal, for geometrical reasons, with Δa. With $\Delta a_{PSD} = a_{PSD,2} - a_{PSD,1}$ the difference at the photodetector and c the conversion factor ($a = c \cdot a_{PSD}$), we get:

$$c \equiv \frac{\Delta a}{\Delta a_{PSD}} = \frac{\Delta b}{\Delta a_{PSD}} \tag{2.15}$$

The experimental procedure consists of a cantilever oscillating in one point (x_0, y_0) with an amplitude (at the photodetector) $A_{PSD,1}$ and a frequency shift df_1. The amplitude is decreased in steps from 1 V to 0.5 V and the frequency shift increased so that equation 2.14 is satisfied. The response of the cantilever is monitored. The conversion factor is calculated using relation 2.15. We obtained values for the amplitude in the range of 7 to 10 nm.

3 Numerical calculations

The Monte Carlo method is a powerful tool to obtain values for macroscopic properties starting from a microscopic description of the system. We have developed a Metropolis Monte Carlo model to calculate arrangements of magnetic moments that correspond to minimum energy configurations. For a system of N nanoparticles fixed in the positions $(x_i, y_i, z_i),\ i = \overline{1, N}$, the magnetic moments are able to rotate in the dipole field created by the surrounding particles. The energy of the system has two main contributors: magnetic dipole-dipole energy and anisotropy energy. For a system of magnetite nanoparticles, we show that the magnetic moments tend to arrange themselves in-plane, in flux-closure (i.e. head-to-tail configuration). We will discuss that the calculated arrangement of moments is not unique. Subsequently, for a calculated configuration of moments, spectroscopy curves and MFM images are simulated.

3.1 Monte-Carlo method

Numerical methods that are known as Monte Carlo methods can be described as statistical simulation techniques, where statistical simulation is defined in a general way as any procedure that uses sequences of random numbers to perform the simulation.

Statistical simulation methods may be contrasted to conventional numerical methods, which typically solve equations that describe the behavior of the system. In many Monte Carlo calculations the physical process is simulated directly; the only requirement is that the behavior of the system can be described by a probability function. Once this is known, the Monte Carlo algorithm can proceed by randomly sampling (the result is accepted or rejected according to the probability function). Many simulations are performed and the final result is an average over a number of observations. One can also calculate the statistical error in the average result.

We now consider the case of a canonical ensemble: a system in contact with a heat reservoir of temperature T [53]. The energy of the system depends on the variables $\mathbf{x}^N$, where N is the number of particles and $\mathbf{x}$ a vector related to the degrees of freedom of each particle. The probability distribution $\rho(\mathbf{x}^N)$ of the system being in the configuration defined by $\mathbf{x}^N$ with energy $E(\mathbf{x}^N)$ is given by:

$$\rho(\mathbf{x}^N) = \frac{\exp(-\beta E(\mathbf{x}^N))}{\sum_{\mathbf{x}^N} \exp(-\beta E(\mathbf{x}^N))} \tag{3.1}$$

where $\beta = (k_B T)^{-1}$, $\exp(-\beta E(\mathbf{x}^N))$ is called the Boltzmann factor and $\sum_{\mathbf{x}^N} \exp(-\beta E(\mathbf{x}^N))$ the partition function, Z.

Calculation of the partition function requires sampling over the whole space of configurations (calculating the Boltzmann factor in every state). It turns out that for some situations it is not necessary to calculate Z. One can construct an algorithm that searches important regions of the configuration space (where the Boltzmann factor differs significantly from zero) and concentrates the sampling there. This is mainly done by constructing a transition matrix that satisfies certain conditions related to the dynamics of the systems.

We consider the system in the state i defined by $\mathbf{x}_i^N$. To sample the configuration space a new state j defined by $\mathbf{x}_j^N$ is generated. The probability of transition is given by the transition matrix π where the elements of the matrix π_{ij} are given by the probability of a transition from state i to state j. We turn now to the principle of detailed balance that states that in equilibrium the transition rate between two states mutually balance each other and is written as:

$$\rho(x_i^N)\pi_{ij} = \rho(x_j^N)\pi_{ji} \tag{3.2}$$

where $\rho(x_i^N)$ comes from the fact that in order for the transition to occur, the system has to be in the corresponding state.

The probability of a transition consists of two parts: the probability of attempting to move from state i to state j (α_{ij}) and the probability to accept the move (λ_{ij}). We choose α and λ:

$$\alpha_{ij} = \alpha_{ji} = 1,\ i, j = \overline{1, N} \tag{3.3}$$

since we consider that all transitions are possible and

$$\lambda_{ij} = \begin{cases} 1, & \text{for } E(x_j^N) \leq E(x_i^N) \\ \exp(-\beta(E(x_j^N) - E(x_i^N))), & \text{for } E(x_j^N) > E(x_i^N) \end{cases} \tag{3.4}$$

This choice for α_{ij} and λ_{ij} satisfies relation 3.2. The Monte Carlo simulation that uses the probability described in this equation is called Metropolis Monte Carlo.

3.2 Energy of the system

The energy of the system is crucial in running the simulations. As previously stated, we study systems of two-dimensional arrays of N magnetic (Fe_3O_4 or $CoFe_2O_4$) nanoparticles. From the TEM images the shape of the particles was determined to be, in good approximation, spherical (the shape anisotropy is negligible). They are fixed at the positions x_i, y_i, z_i, with $i = \overline{1, N}$, with the distance between them in the range of 2 to 4 nm. This is due to a surfactant layer (oleic acid and oleylamine) that covers the particles. Therefore, exchange-coupling interactions between particles are negligible. The size of the particles is about 20 nm (excluding the surfactant layer) and, as discussed in section 2.2, the particles are assumed to consist of a single magnetic domain. Their magnetic moments rotate in the magnetic field created by the surrounding particles in order to reach the minimum energy configuration.

It is expected for these particles to have strong magnetic dipole-dipole interactions [21, 44]. We consider first the magnetic field of a point dipole:

$$\mathbf{B_i}(\mathbf{r}) = \frac{\mu_0}{4\pi}\frac{3(\mathbf{m_i}\cdot\mathbf{r})\cdot\mathbf{r} - \mathbf{m_i}r^2}{r^5} \tag{3.5}$$

where $\mathbf{m}_i$ is the magnetic moment of the nanoparticle, $\hat{\mathbf{r}} = \mathbf{r}/r$ is the unit vector in the direction of $\mathbf{r}$, $r = |\mathbf{r}|$ and $\mu_0 = 4\pi\cdot 10^{-7} N/A^2$ is the permeability of vacuum. The interaction energy of a dipole with a magnetic field of another dipole is:

$$E = -\mathbf{m_j}\cdot\mathbf{B_i}(\mathbf{r}) \tag{3.6}$$

Writing this energy for two dipoles we obtain:

$$E_{ij} = -\frac{\mu_0}{4\pi} \frac{3\mathbf{m_j}\cdot(\mathbf{m_i}\cdot\mathbf{r_{ij}})\cdot\mathbf{r_{ij}} - r_{ij}^2\cdot\mathbf{m_i}\cdot\mathbf{m_j}}{r_{ij}^5} \tag{3.7}$$

where $\mathbf{r_{ij}} = \mathbf{r_i} - \mathbf{r_j}$.

The total dipole-dipole energy is given by the summation over all particle pairs:

$$E_{d-d} = \sum_{i=1}^{N} \sum_{j<i} E_{ij} \tag{3.8}$$

It is convenient to write $\mathbf{r}_{ij}$ and $\mathbf{m}_i$ in Cartesian coordinates and the components of the magnetization as function of the zenith and azimuth angles, α_i and β_i. We will further denote the vectors $\boldsymbol{\alpha} = (\alpha_i)_{i=1,N}$ and $\boldsymbol{\beta} = (\beta_i)_{i=1,N}$.

Magnetocrystalline anisotropy can also be important for the total energy of the system. Fe_3O_4 nanoparticles have a small coercivity (see discussion in section 4.1) and we will consider them superparamagnetic, i.e. the magnetic moment is free to rotate. $CoFe_2O_4$, at low temperature, is known from literature to exhibit high anisotropy [17], with three easy axes [14][1]. This anisotropy energy creates large energy barriers preventing the moments to freely rotate inside the particles. It will play an important role in the results presented in this thesis. The first order expression for the anisotropy energy E_i for the particle i is:

$$E_i = V\cdot K_c \left({m_{x'}^i}^2 {m_{y'}^i}^2 + {m_{y'}^i}^2 {m_{z'}^i}^2 + {m_{z'}^i}^2 {m_{x'}^i}^2 \right) \tag{3.9}$$

where V is the magnetic volume of the nanoparticles, K the first-order anisotropy constant and $m_{x'}^i, m_{y'}^i, m_{z'}^i$ the projections of the $\dfrac{\mathbf{m}_i}{|\mathbf{m}_i|}$ vector along the easy axes directions. The total anisotropy energy is given by:

$$E_{an} = \sum_{i=1}^{N} E_i \tag{3.10}$$

.

To express the anisotropy energy as function of $\boldsymbol{\alpha}$ and $\boldsymbol{\beta}$ we need to write $m_{x'}, m_{y'}, m_{z'}$ as function of m_x, m_y, m_z for each particle. We give the direction of the easy axes using the Euler angles in the "x-convention" [54], θ, ϕ, ψ, and:

$$\begin{pmatrix} m_{x'} \\ m_{y'} \\ m_{z'} \end{pmatrix} = \mathbf{A} \begin{pmatrix} m_x & m_y & m_z \end{pmatrix} \tag{3.11}$$

[1] In this article [14] it is stated that the 5-nm-diameter $CoFe_2O_4$ particles exhibit cubic anisotropy with a small contribution of uniaxial anisotropy. It is expected that the uniaxial anisotropy decreases with the increasing size of the nanoparticles. 40-nm $CoFe_2O_4$ particles have been shown to exhibit cubic anisotropy [17].

where **A** is the rotation matrix.

Addition of the dipole-dipole energy given by equation 3.8 and the anisotropy energy given by equation 3.9 yields the total energy $E(\boldsymbol{\alpha}, \boldsymbol{\beta})$ of the system:

$$E(\boldsymbol{\alpha}, \boldsymbol{\beta}) = E_{d-d} + E_{an} \tag{3.12}$$

This is the energy used in the expression of the acceptance probability 3.4.

3.3 Monte-Carlo calculations

We have constructed an algorithm[2] using the Metropolis Monte Carlo applied for our system; we allow the magnetic moments of the particles to rotate[3] (Néel rotation) in order to find the minimum-energy configuration. Monte Carlo is done following the steps:

1. Assign initial values to the angles of the magnetic moments. This can be done in a random way or by using initial values obtained in a previous run of the program.

2. Calculate the total energy of the system, $E_k(\boldsymbol{\alpha}, \boldsymbol{\beta})$.

3. Make a trial move. This means to rotate the angles of a particle by small[4] random amounts. Calculate the energy in the new configuration, $E_l(\boldsymbol{\alpha}, \boldsymbol{\beta})$.

4. If the new energy is lower than the previous one, accept the move.

5. If the new energy is larger, generate a random number $rn \in (0, 1)$ and compare it with the Boltzmann factor of the energy difference, $\exp\left(-\frac{E_l - E_k}{k_B T}\right)$. If the Boltzmann factor is larger than rn accept the move, reject it otherwise.

6. Go back to step 3 for the next particle. If all the moments have been rotated, the procedure continues with the rotation of the moment of the first particle.

Computer simulations are subject to statistical and systematic errors. The mediated value of the energy and its error are calculated assuming a Gaussian

[2]We thank Peter Liljeroth for his contribution in developing the algorithm.
[3]The particles are fixed on the surface, unable to move or rotate.
[4]That means sufficiently small so that the moments cannot "jump" over the energy barriers without the necessary energy.

distribution of the values of the energy over a large number (τ) of accepted configurations (the first few hundred configurations are not considered):

$$\langle E \rangle = \frac{1}{\tau} \sum_{i=1}^{\tau} E_i \tag{3.13}$$

If the configurations are independent, the standard deviation is:

$$\sigma(E) = \frac{1}{\tau} \sqrt{\sum_{i=1}^{\tau} (E_i - \langle E \rangle)^2} \tag{3.14}$$

Systematic errors can be generated, for example, by numerical approximations, system size or the random number generator used in the program. In our numerical code, a program by R. P. Brent [55] was used to generate random numbers in between 0 and 1 using the "generalized Fibonacci" method. The systematic errors are expected to be well within the standard deviation.

3.4 Case study

As an example, we present the case of 36 superparamagnetic Fe_3O_4 nanoparticles hexagonally packed in a two-dimensional structure. The magnetic moment of the individual particles is $1.55 \cdot 10^{-18} Am^2$, a value experimentally determined (see section 2.2). We calculated for 300 K the total energy of the system as a function of the number of steps. Each step corresponds to the situation where all the moments have been rotated once (Fig. 3.1). We start with random initial orientations of the moments and therefore the total energy is relatively large. It decreases very fast in the first few hundred steps until it reaches a relative minimum energy configuration. It will subsequently attempt to overcome the energy barriers created by the surrounding particles. Depending on thermal energy ($k_B T$), the height of the energy barrier and a random number it will succeed in an attempt or not. This is illustrated by the fluctuations of the total energy around a specific value.

The final arrangement of moments is shown in Fig 3.2(a). The magnetic moments arrange themselves in-plane, in a flux-closure-type structure. It is an understandable result since the head-to-tail arrangement corresponds to a minimum energy configuration for magnetic dipoles. The total energy for this configuration is (-8.27 ± 0.17) eV. To address the question whether or not the arrangement of moments is unique, the procedure was repeated using a different initial configuration of moments. The results are presented in Fig. 3.2(b). Although the moments are also mainly in-plane and they tend to arrange themselves again in a flux-closure-type structure, it is clear that many of the moments have a different orientation. The energy of this configuration

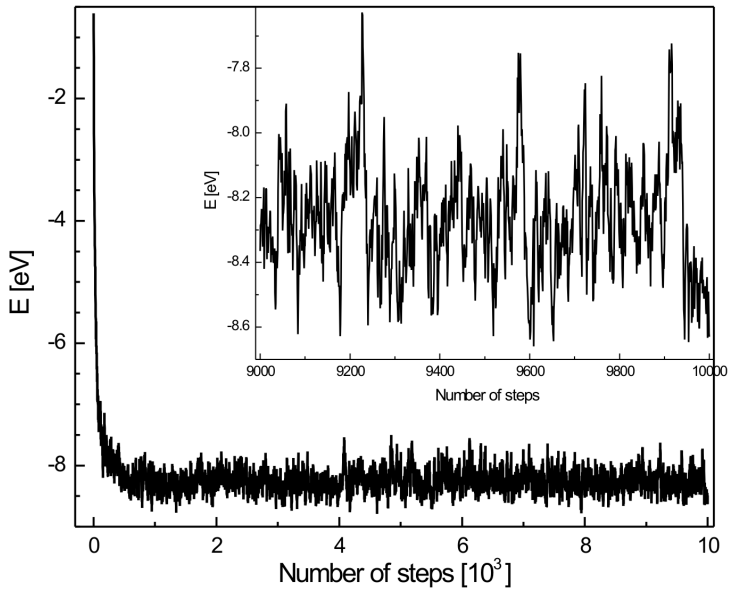

Figure 3.1: *The energy of the system as a function of the number of steps. The inset shows the evolution of the energy over the last 1000 steps, where the mediated energy and its standard deviation were calculated.*

is (-7.81 ± 0.18) eV. With an energy of 0.22-0.23 eV per particle these configurations are stable with respect to thermal excitations. We conclude that the arrangement of moments is not unique, meaning that, depending on the sample preparation, more configurations are possible, although after a long time the arrangement with a smaller energy is more probable.

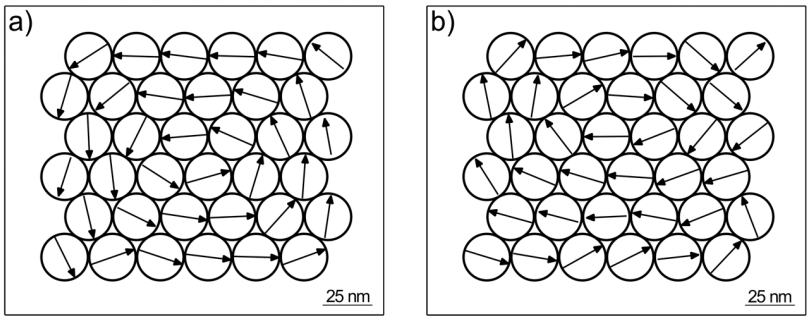

Figure 3.2: *Two possible configurations obtained running Monte Carlo for the given configuration of nanoparticles. The arrows indicate the in-plane components of the magnetic moments.*

3.5 SPECTROSCOPY CURVES AND MFM IMAGES

With the arrangement of magnetic moments known, the MFM image and the force and frequency shift as a function of the tip-sample distance can be calculated[5].

In order to simulate the MFM image, the tip, with the magnetization $\mathbf{m}_{tip} = (m_x^{tip}, m_y^{tip}, m_z^{tip})$, is scanned above the surface at a fixed distance (d). The force and subsequently the frequency shift are calculated for the system in each point $(x,\ y)$. We start with the energy of the tip and particle system:

$$E(x,y,z) = \frac{\mu_0}{4\pi} \sum_{i=1}^{N} \left(\frac{\mathbf{m}_i \cdot \mathbf{m}_{tip}}{r_i^3} - 3\frac{(\mathbf{m}_i \cdot \mathbf{r}_i)(\mathbf{m}_{tip} \cdot \mathbf{r}_i)}{r_i^5} \right) \tag{3.15}$$

with $\mathbf{m_i}$ the magnetization of the particle i and $\mathbf{r_i}$ the distance vector between particle i and the tip. The force is calculated using the relation:

$$F(x,y) = -\frac{\partial E(x,y,z)}{\partial z} \mid_{z=d} \tag{3.16}$$

and the frequency shift using relation 2.8.

The image that can be compared with an experimental MFM image is $df(x,y;z=const)$. The image calculated using the configuration presented in Fig. 3.2(a) at a distance of d = 40 nm (value typically used in our experiments) from the particles is shown in Fig. 3.3. Bright and dark areas are present representing repulsive and attractive forces, respectively (see section 2.5). A one-to-one relation between the areas where the moments are correlated and the magnetic contrast cannot be observed.

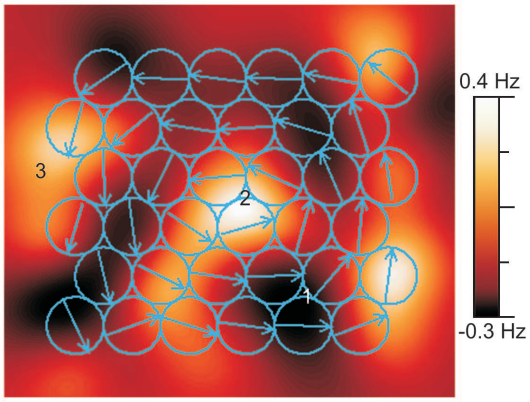

Figure 3.3: *The configuration of particles and magnetic moments and the MFM image taken at 40 nm from the nanoparticles. The magnetization of the tip used was* $2.5 \cdot 10^{-17} Am^2$ *(see section 2.2).*

[5]The calculations are done under the assumption that the tip does not influence the arrangement of moments.

We now consider the tip in the position (x_0, y_0) and the tip-sample distance, z, is increased from 0 to 100 nm. The dipole-dipole energy between the tip and the particles is:

$$E(z) = \frac{\mu_0}{4\pi} \sum_{i=1}^{N} \left(\frac{\mathbf{m}_i \cdot \mathbf{m}_{tip}}{r_i^3} - 3\frac{(\mathbf{m}_i \cdot \mathbf{r}_i)(\mathbf{m}_{tip} \cdot \mathbf{r}_i)}{r_i^5} \right) \tag{3.17}$$

The force is:

$$F(z) = -\frac{dE(z)}{dz} \tag{3.18}$$

and the frequency shift is calculated using relation 2.8.

Three curves are presented in fig. 3.4. The curves are taken in the points indicated in Fig. 3.3; curves 1 and 2 are taken on top of the island and curve 3 is taken at the side. They show long-range (up to 70 nm) attractive and repulsive forces. The magnetic field at this large distance originates from more than one particle. It is therefore impossible to directly correlate the orientation of the individual magnetic moments to the MFM image.

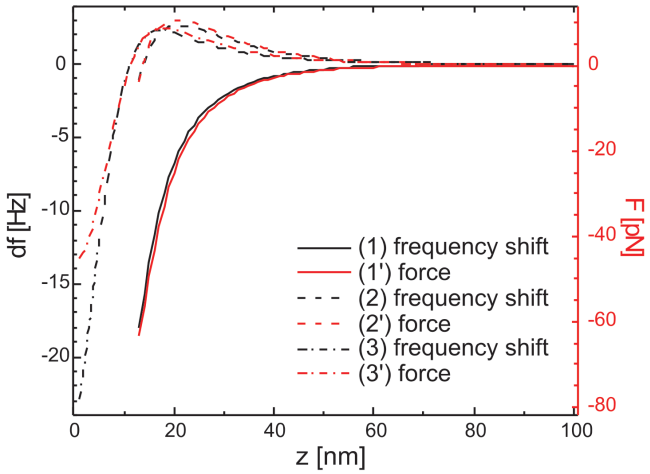

Figure 3.4: *Force and frequency shift as a function of tip-sample distance. 0 nm corresponds to the substrate. Curves 1, 2 and 3 are calculated in points 1, 2 and 3 (indicated in Fig. 3.3), respectively. Curves 1', 2' and 3' represent the corresponding forces.*

4 Flux-closure in magnetite nanoparticle assemblies

This chapter presents the results obtained in MFM investigations of two-dimensional assemblies of 20-nm-diameter magnetite (Fe_3O_4) particles. On top of the islands of these particles only attractive interactions have been observed. This is explained by the strong magnetic moment of the tip reorienting the magnetic moments of the nanoparticles. At the side of the islands, when the tip is laterally further away from the particles, attractive and repulsive interactions are observed. The repulsion is a strong indication of ordering: the magnetic dipole-dipole interactions between the nanoparticles in the island block the moments in a flux-closure-type structure. Another indication of ordering can be observed in the MFM images, where structures on top of the islands are present. Monte Carlo simulations are used to illustrate the flux-closure behavior. Similar results are obtained for very large islands and maze-type particle configurations. For very small islands consisting of only few particles, as expected, the magnetic interactions are very weak. As a test for the proposed model, experimental results obtained for 10-nm magnetite particles are presented as well. Due to the smaller dipolar moment, the flux-closure is no longer observed.

4.1 Background

The systems studied in this chapter consist of two-dimensional aggregates of magnetite nanoparticles. The nanoparticles are considered spherical, about 20 nm in diameter, with a polydispersity of less than 8 %. The particles are small enough to have one magnetic domain and large enough to exhibit a large dipole moment.

Previous work [26] has shown that 5-nm and 10-nm magnetite particles have a blocking temperature (T_B) of about 40 K and 110 K, respectively, values that have been determined using a 100 Oe field. T_B is expected to increase further with increasing nanoparticle size. For 20 nm magnetite nanoparticles, dynamic-susceptibility measurements have been done at room temperature [21] and show that the moments are blocked. However, the blocking has been attributed to the interactions between particles rather than to the anisotropy of the individual particles. For the individual particles, using an anisotropy constant of $7 \cdot 10^3$ J/m^3 [56] and a cubic anisotropy model, we estimate an anisotropy energy barrier[1] $\Delta E_{an} = 5.7 \cdot 10^{-21}$ J per particle at room temperature. Considering the Boltzmann factor, this leads to a 25 % probability that the moments overcome (in each attempt) the internal energy barrier to arrange themselves according to the dipole-dipole interactions. This means that effectively the particles can be considered superparamagnetic. Also, using Monte Carlo simulations, we will show that the influence of anisotropy on the arrangement of moments is minimal.

In order to study the interactions in two-dimensional systems, the particles are deposited on a flat, conductive substrate (HOPG) in monolayered islands. The distance in between the particles is about 3 to 4 nm due to the surfactant layer.

4.2 Experimental results

Non-magnetic measurements

After preparation (as discussed in Section 2.2), the sample was mounted and introduced into the UHV setup. Using a non-magnetic tip (Si) in non-contact AFM, we studied the topography of the sample. We have also carried out z-spectroscopy.

The results are presented in Fig. 4.1. It shows monolayered islands, where the particles do not seem to arrange themselves in a perfect hexagonal array. At a close look, besides the graphite steps, steps with a height of about 2.4 nm can be observed (Fig. 4.1(c)). We conclude that a partial layer of surfac-

[1] The energy necessary for rotation of the dipole moment in a plane containing two of the three easy axes of magnetization, i.e. $K_1 V/4$ [57], where K_1 is the anisotropy constant and V is the volume of the nanoparticle.

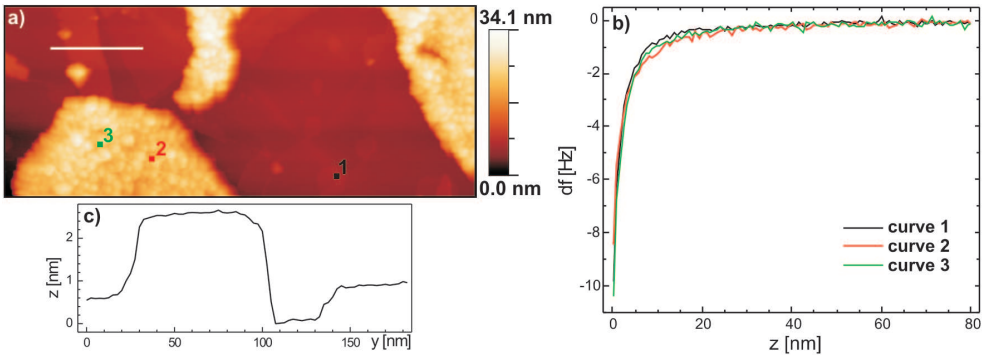

Figure 4.1: *(a) Topography of the sample (407 × 1000 nm^2 area) taken with a Si tip with $f_0 = 285.1\ kHz$ and $k = 42\ N/m$. (b) Z-spectroscopy taken at the points indicated in (a). (c) Line profile along the white line indicated in (a).*

tant, present in the solution to prevent particle conglomeration over a large period of time, has been deposited on the HOPG. Fig. 4.1(b) shows 3 typical z-spectroscopy curves measured at the positions indicated in Fig. 4.1(a). The interaction between tip and sample is dominated by van der Waals forces. The difference between the different curves is very small. Therefore, we conclude that the van der Waals forces on top of the substrate and on top of the magnetite are similar.

Magnetic measurements: large particles

To obtain information on the magnetic properties of the sample, we have used a magnetic tip to perform measurements at room temperature and at low temperatures. The results were similar. We present here a measurement done at 118 K, (Fig. 4.2 and Fig. 4.3)[2]. The tip was oscillated at its resonant frequency of 70.148 kHz, with an amplitude of about 9 nm.

The islands consist mainly of monolayers of nanoparticles with maybe in some areas an extra particle on top. The lateral resolution in the "topography" image is about 20 nm as can be seen at the edges of the island where individual particles can be distinguished. However, the resolution worsens above the nanoparticle islands where long-range attractive forces are present. The spectroscopy curves show the dependence of the frequency shift on the applied potential in the indicated positions (see Fig. 4.2(a)). There are two typical curves: one measured on top of the island (curve 1), with a weak dependence on the potential, and the other ones on top of the substrate. The latter curves exhibit different maxima, at about 0.35 V, 0.45 V and 0.55 V, respectively. Since the sample is not flat, as can be seen from the topographical image, the contact potential differs from one position to the other. To compensate for electrostatic forces on top of the island, we applied a potential of 0.45 V to

[2]Temperature measured at the cooling block

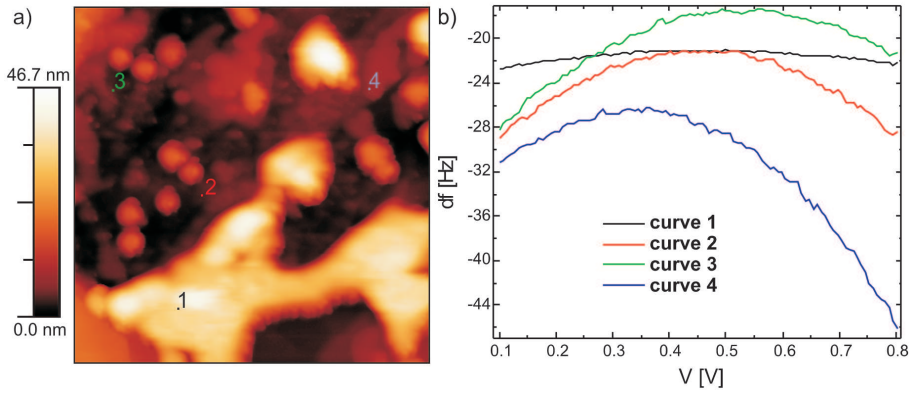

Figure 4.2: *Measurement carried out at 118 K. (a) "Topography" of an* 880 × 880 nm^2 *area of the sample. Note that since the feedback is relatively low (-17 Hz), a strong contribution of the magnetic interactions is present. This can be seen in the large contrast (vertical scale bar of the figure) the sample exhibits. (b) V-spectroscopy curves measured at the positions indicated in (a).*

the tip. The compensation on top of the graphite is not complete everywhere, but the electrostatic signal is below 1 Hz.

The MFM image of the same area (Fig. 4.3(b)), taken at a distance of 60 nm from the substrate (35 nm from the island), shows above the islands dark-colored areas (negative frequency shift), reflecting attraction. The MFM image is reproducible for a tip-substrate distance of 50 nm. Similar results were obtained at other islands of the sample and of other samples. We interpret the attraction in terms of the relatively strong magnetic field of the tip, reorienting the moments of the nanoparticles along the tip's field lines.

Considering the MFM images, it seems that the interactions between tip and nanoparticles are always attractive. Employing spectroscopy, however, we will show that in specific areas repulsion is present (see Fig. 4.3(c)). Curve 1, taken above the HOPG shows attraction due to van der Waals forces. Curves 2, 3, and 4, taken on top of the island, show also attraction but with a much weaker distance dependence. This long-range attractive behavior of the force agrees well with the MFM image and the interpretation given. Curves 5-8 were measured at the edge of the island. Surprisingly, the interaction is predominantly repulsive, with the repulsion becoming stronger when (laterally) approaching the island. These curves show that for the large distances of 60 nm, at which the MFM image was taken, the frequency shift is small, explaining why repulsion is not visible in the MFM image. More details on the interactions at the edge of the islands are presented in Section 4.4.

Repulsion indicates that the magnetic moments of the particles are blocked. Obviously, with the tip laterally sufficiently far away, the field exerted by the tip is sufficiently weak and the magnetic moments of the nanoparticles are blocked. Since the coercivity of the individual nanoparticles is small, the

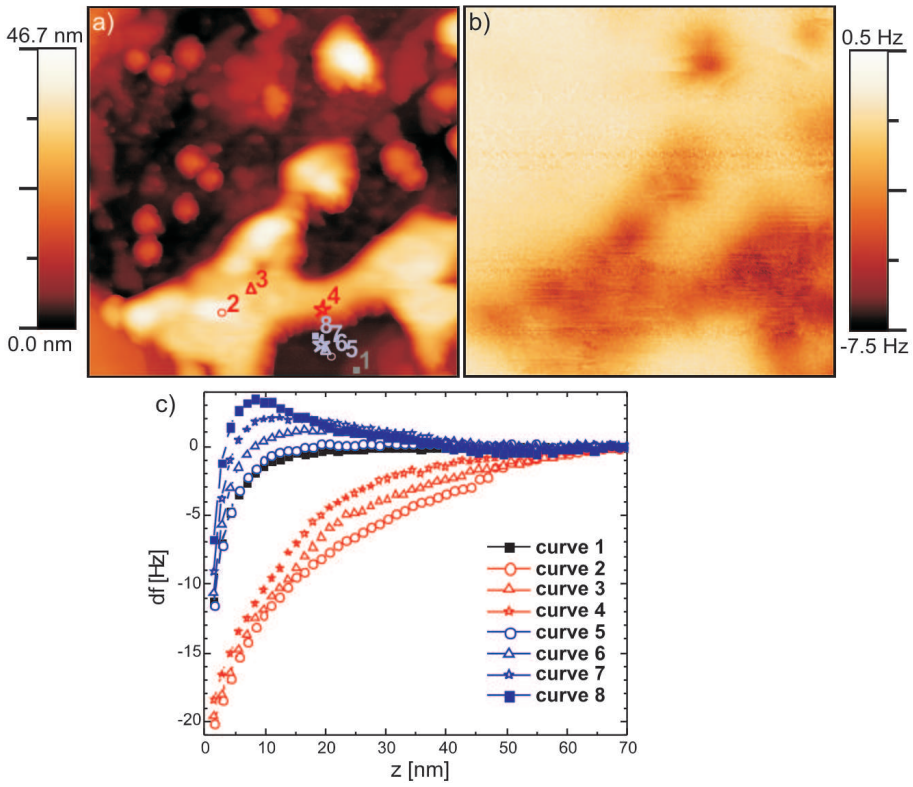

Figure 4.3: *Measurement carried out at 118 K. (a) "Topography" of an* 880 × 880 nm^2 *area of the sample. (b) MFM image of the same area taken at a distance d = 60 nm from the substrate. (c) Spectroscopy curves taken at the locations indicated in (a).*

blocking is probably caused by the strong dipolar coupling between the nanoparticles in the aggregate. For two nanoparticles with a magnetic moment of $1.55 \cdot 10^{-18}$ Am^2 (see Section 2.2), with an interparticle spacing of 3 nm, a minimum dipole-dipole energy (of -96 meV per particle) is obtained for the head-to-tail configuration of the moments. For a 2D island of nanoparticles, the dipoles are oriented such as to minimize the total energy of the system. This explains our experimental observations: an approaching tip may be repelled since, for the reorientation of the magnetic moments, an energy barrier has to be overcome. As will be shown in the next section, the magnetic moments are arranged in a flux-closure-type structure.

On top of the island in the MFM image (Fig. 4.3(b)), weak features are visible. We present a similar measurement in Fig. 4.4, where these features are more clearly visible. The MFM image shows contrast on top on the islands. The features most likely originate in the partial blocking of the moments. Spectroscopy curves show again long-range attractive forces, but the dependence with the distance is slightly different from one curve to another.

We can preliminarily conclude that the measurements on islands of mag-

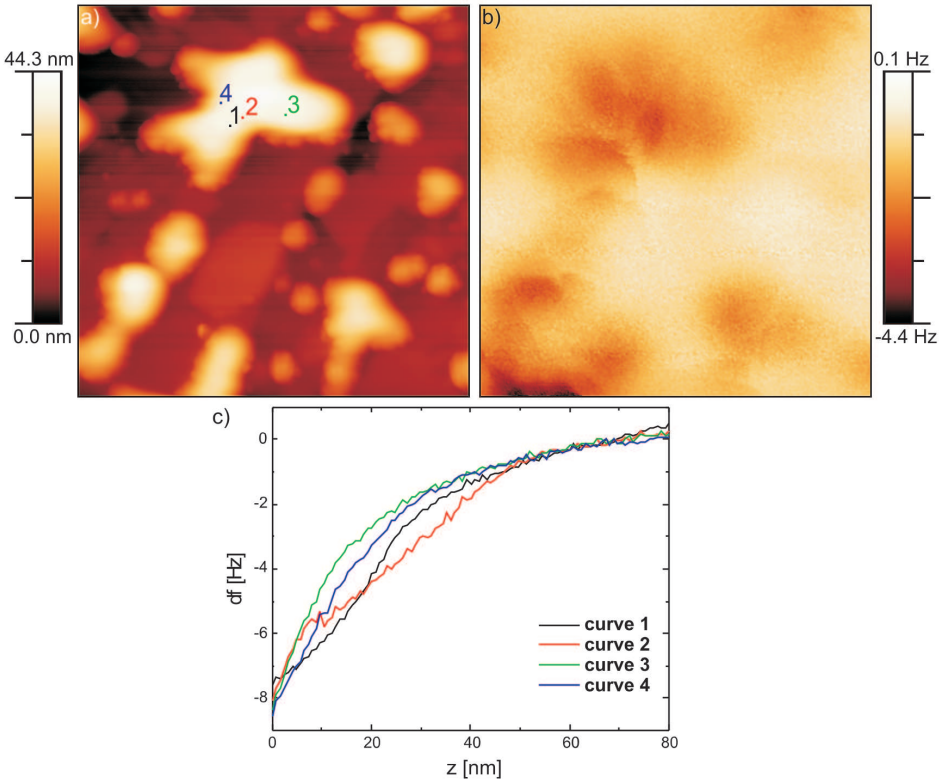

Figure 4.4: *Measurement carried out at room temperature. (a) "Topography" of a 750 × 750 nm^2 area of the sample. (b) MFM image of the same area taken at a distance $d = 60$ nm from the substrate. (c) Spectroscopy curves taken at the locations indicated in (a).*

netite nanoparticles are a consequence of a competition between the dipole-dipole interactions trying to arrange the moments in flux-closure and the tip trying to rotate the moments along its field lines.

Magnetic measurements: small particles

As a test for the proposed model, we performed further experiments on 2D islands of significantly smaller magnetite nanoparticles (physical diameter 10.8 nm; magnetic diameter 9.4 nm). The maximum dipolar energy of two particles separated by 3 nm amounts to about -8.5 meV per particle. This energy is small compared to k_BT at room temperature and dipolar coupling should not play any role. The consequence of the small diameter is illustrated in the measurements presented in Fig. 4.5, where, besides the smaller contrast due to the smaller magnetic moment of the particles, no repulsion at the edges of the island or features on top of the island in the MFM image were observed. Also, in other experiments on different islands, repulsion was never observed.

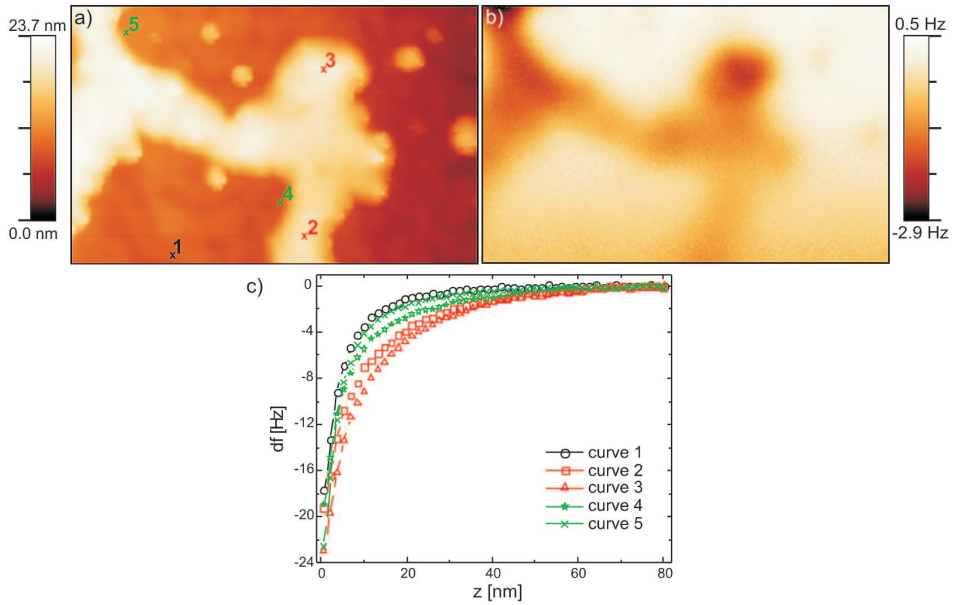

Figure 4.5: *Measurements on a 2D system of 10.8-nm magnetite nanoparticles, carried out at room temperature. (a) "Topography" of a* 1000×635 nm^2 *area of the sample. (b) MFM image of the same area taken at a distance d=50 nm from the substrate. (c) Spectroscopy curves taken at the locations indicated in (a).*

4.3 Monte Carlo simulations

To study the magnetic dipolar interactions in a more quantitative way, we performed Monte Carlo simulations on an arrangement of 40 nanoparticles. We used the values $m_p = 1.55 \cdot 10^{-18}$ Am^2 and $m_{tip} = 2.5 \cdot 10^{-17}$ Am^2 for the magnetic moments of the particles and tip, respectively, as discussed in Section 2.2. Few aspects of our interpretation of the results will be studied in detail:

- The flux-closure type arrangement of the moments.
- The assumption of superparamagnetic particles.
- The presence of repulsion at the side of the island, the shape of the curves and the dependence on the lateral distance to the island.
- The influence of the tip on the arrangement of moments.

Flux-closure

Fig. 4.6(a) shows the configuration of particles we have considered in these simulations. In the background, the region in the low central part of the experimental image presented in Fig. 4.3(a) is shown. We started with an arbitrary configuration of magnetic dipoles, i.e. with their moments pointing in any direction *in* as well as *out* of the plane of dipoles (Fig. 4.6(b)). The magnetic

moment of the tip was considered perpendicular to the surface, towards the sample. The temperature amounts to 120 K, similar to the temperature in the experiments. The configuration of moments obtained after running Monte Carlo simulations in the absence of the tip is presented in Fig. 4.6(c) and has a total energy of $-8.15 \pm 0.07\ eV$. Using the configuration shown in Fig. 4.6(c) the MFM image has been simulated. We present it in Fig. 4.6(d). In the simulation of the MFM image, the moments of the particles are assumed to be "frozen", i.e. they are not allowed to rotate in the field of the tip. This is the reason why on top of the island repulsive and attractive interactions are found. As anticipated in the experimental section, in the absence of the tip, the magnetic moments arrange themselves in-plane, in flux-closure structures.

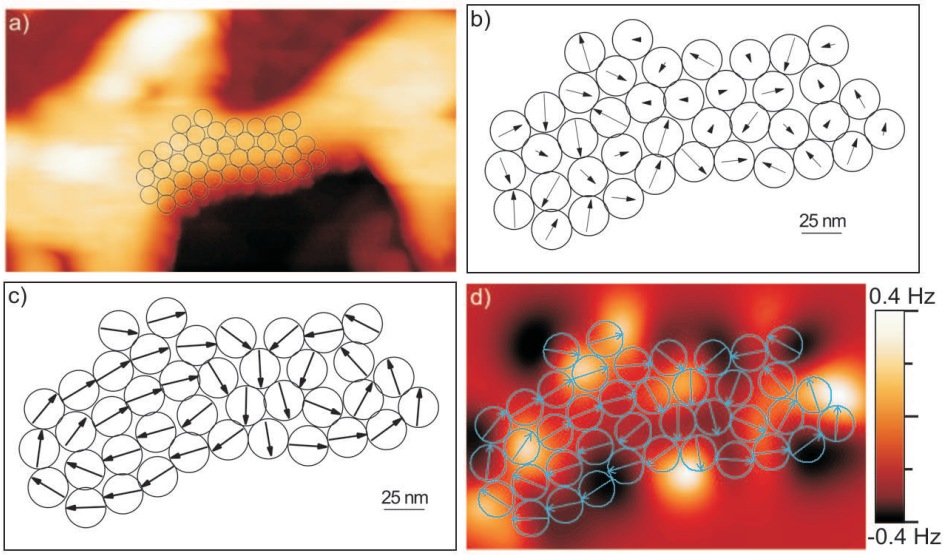

Figure 4.6: *(a) A configuration of 40 nanoparticles that we considered in these simulations. The background shows a* $650 \times 380\ nm^2$ *area on the sample. (b) The initial configuration of moments used in these simulations. (c) The obtained configuration of moments after running Monte Carlo, at a temperature of 120 K. (d) For this configuration of nanoparticles and moments, the calculated MFM image at a distance of 60 nm from the substrate.*

Anisotropy energy

We will now study the effect of the anisotropy energy on the final arrangement of moments. We consider the same configuration of particles with the same initial conditions, without anisotropy and with an anisotropy constant $K_1 = 7 \cdot 10^3\ J/m^3$ [56]. We assume also a random cubic anisotropy model (i.e. we considered three easy axes for each particle with the orientation of the easy axes arbitrarily chosen). As it can be observed from Fig. 4.7, the influence of the anisotropy on the configuration of moments is relatively small. Considering the total energy of the two configurations, -8.15 eV for the configuration

calculated without anisotropy and -7.00 eV for the configuration calculated with anisotropy (-7.66 eV dipole energy and 0.66 eV anisotropy energy), it is clear that, although anisotropy adds disorder to the orientation of moments, the flux-closure is preserved. The MFM images are notably different, indicating their sensitiveness to the detailed orientation of the moments. One should be aware, however, that the images cannot be compared with the experiments since in the experiments presumably the moments are influenced by the tip. We conclude that for magnetite the small anisotropy does not have a large influence on the final orientation of the moments and, for a qualitative interpretation, the assumption of superparamagnetic nanoparticles is justified.

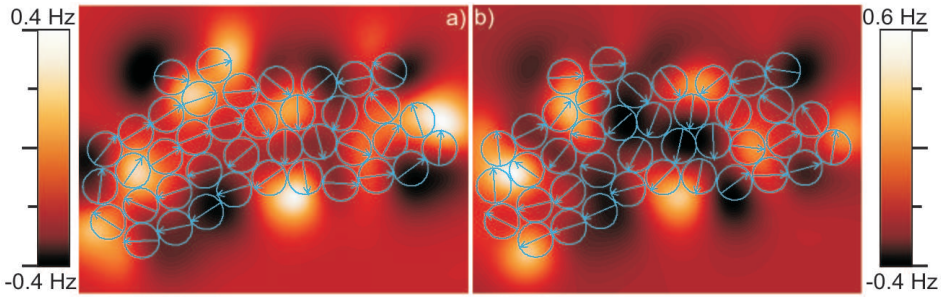

Figure 4.7: *The obtained configurations of the moments and the corresponding MFM image calculated at 60 nm away from the sample. (a) with anisotropy constant* $K_1 = 0\ J/m^3$ *and (b) with* $K_1 = 7 \cdot 10^3\ J/m^3$.

Spectroscopy curves: without influence of the tip

In the experiments, we have observed repulsive interactions at the edges of the islands. The next question we would like to address is, whether or not in the simulated flux-closure type arrangement of moments, repulsive interactions can be obtained. Freezing the moments, spectroscopy curves have been calculated in the positions indicated in Fig. 4.8(a). Repulsion is indeed obtained, as shown in Fig. 4.8(b). The repulsive curves have similar shapes as the experimental curves (Fig. 4.8b, inset). Two differences can however be noticed. The dependence with the lateral distance is stronger for the simulated curves, i.e. the repulsive signal which is generated mainly by the particles at the side of the island disappears at an estimated lateral distance of 30 nm to the island, while this distance can be estimated to amount to 60 nm for the experiment. Secondly, there is a horizontal shift between the experimental and calculated curves, i.e. the maximum of the simulations is reached at different distances z. These differences can both be attributed to the assumption in the simulations of a point-like tip with the moment considered at its apex. A small contribution to the horizontal shift is caused by the different meaning of z = 0 nm in experiments and simulations (see the discussion of Fig. 4.10).

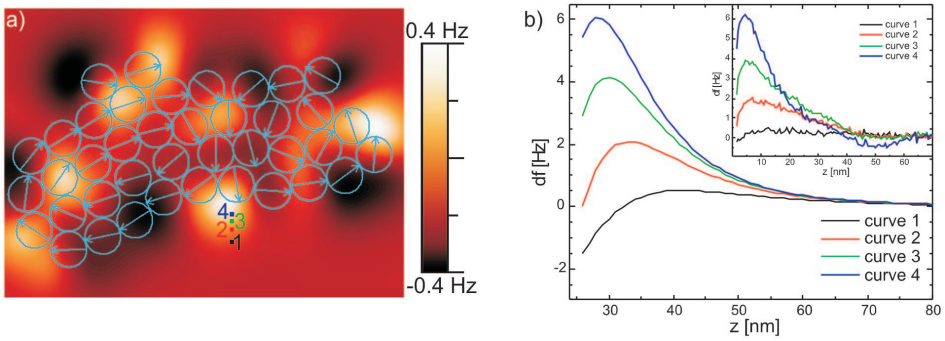

Figure 4.8: *Results of the Monte Carlo simulations for an island of 40 nanoparticles at a temperature of 120 K. The total energy of the system is* -8.15 ± 0.07 *eV. (a) The obtained configuration of the moments and the corresponding MFM image calculated at 60 nm away from the sample. (b) Simulated frequency shift curves at the (x, y) positions of the tip indicated in (a). The inset shows 4 experimental curves (curves 5-8 in Fig. 4.3 from which the van der Waals interaction was subtracted).*

Spectroscopy curves: with influence of the tip

Thus far we did observe repulsion in the simulations, but one should realize that in the experiments presumably the moments were "pinned" in the field of the tip. We therefore did two sets of additional simulations: one to see if the moments are influenced by the tip and the other to simulate the experimental spectroscopy curves.

First, we performed Monte Carlo simulations with the tip in specific positions on top of the island and at its side. We allowed the particle moments to relax in the presence of the tip. With an estimated value for the attempt frequency for variation of the moments of 10^{10} s^{-1}, the moments are able to follow the oscillation of the tip. The simulation (10^4 steps) takes place on a time scale of the order of 10^{-6} s, representing roughly a tenth part of the oscillation period of the tip. We show in Fig. 4.9(a) the calculated configuration of moments of the same aggregate of particles as before, without the tip. In Fig. 4.9(b) the tip was located at the side of the island, in the marked position. The configuration of moments remains practically unchanged compared to the one presented in Fig. 4.9(a), meaning that the moments are blocked in this configuration by dipole-dipole interaction, also in the presence of the tip at the side of the island. In Fig. 4.9(c,d) the tip was located on top of the marked particle, at 25 nm and 50 nm from the substrate, respectively. The moments align along the direction of the field lines: the particle below the tip orients its moment perpendicular to the plane and towards the surface, the surrounding particles orient their moments in plane, away from the tip (see Fig. 4.9(c)). At a larger tip-sample distance, the moments slightly relax towards the flux-closure arrangement (see Fig. 4.9(d)). Similar results are obtained when the tip is positioned in between the particles as shown in Fig. 4.9(e,f). These results are consistent with the experimental observations: when the tip is on

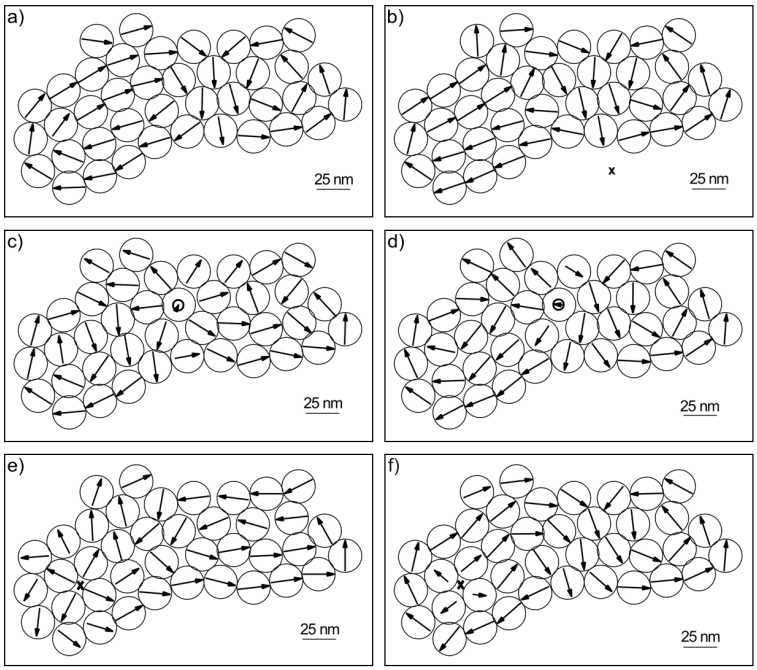

Figure 4.9: *Simulations for the system of nanoparticles in the (a) absence and (b-f) presence of the tip. The tip is situated (b) at the side of the island: at the marked position, at 25 nm from the substrate, (c) on top of the marked particles at 25 nm from the substrate, (d) on top of the marked particle at 50 nm from the substrate, (e) in the marked position (in between the particles) at 25 nm from the substrate, and (f) in the marked position at 50 nm from the substrate.*

top of the island the moments are influenced by the strong field of the tip, leading to attraction.

The second set of calculations was performed to simulate the experimental spectroscopy curves: with the tip in one position ($x_0,\ y_0$), the particles were allowed to relax in the presence of the tip. Monte Carlo simulations were performed at different z positions of the tip. Subsequently, the frequency shift was calculated. Fig. 4.10 shows the frequency shift as function of z for three ($x_0,\ y_0$) positions of the tip.

From the curves in Fig. 4.10(a), with the tip on top of the island, we conclude that the moments appear influenced by the tip, resulting in attraction. While in the calculations z = 0 nm represents the substrate, in the experiments z = 0 nm represents the distance from the sample at which the feedback-set is reached. We present in the inset of Fig. 4.10(a) the two curves laterally shifted so that z = 0 nm corresponds to -15 Hz. The difference between the curves is small, indicating that the differences we notice in the experiments (see Fig. 4.4) have another origin than the difference in the relative position of the tip with respect to its closest neighbor. Fig. 4.10(b) shows the spectroscopy curve calculated for the tip in the position indicated in Fig. 4.9(b),

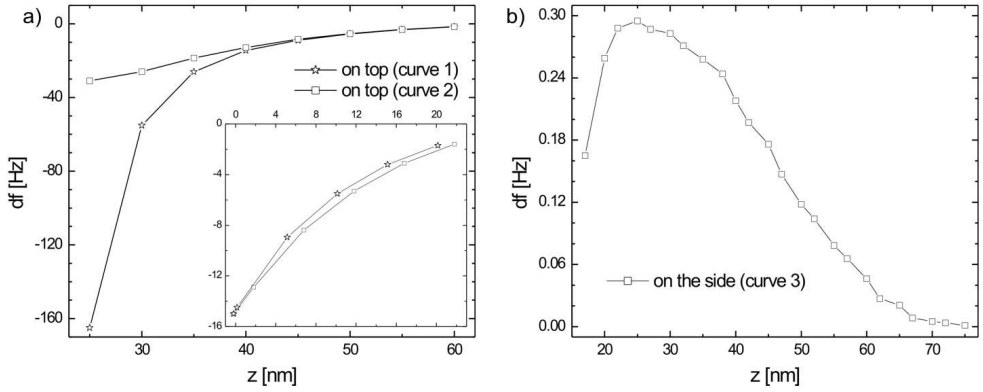

Figure 4.10: *Simulated spectroscopy curves (frequency shift vs. distance) considering the influence of the tip on the orientation of the magnetic moments. The tip is positioned in the locations indicated in Fig. 4.9(c,d) for curve 1, in Fig. 4.9(e,f) for curve 2 and in Fig. 4.9(b) for curve 3. The inset of (a) shows the calculated curves laterally shifted so that 0 nm corresponds to -15 Hz (for comparison with the experiments).*

aside of the island. Repulsion is obtained and, qualitatively, the experimental observations are reproduced in the simulations.

Two differences between the experimental and the simulated spectroscopy curves can be noticed. The calculated frequency shifts for the tip at the side of the island are small. Here, it should be noted that the spectroscopy curves were calculated with the tip laterally farther away from the island in comparison to the experimental distance, resulting in a smaller signal. This was done since at smaller lateral distances the arrangement of moments is significantly disturbed by the magnetic field of the tip. In the experiments, the tip has an apex radius of about 40 nm and the magnetic field is therefore less localized. This can lead to a situation where the moments of the particles are more difficult to influence. Secondly, a lateral shift of the curve can be noticed. The shape and size of the experimental tip were not included in our simulations which can explain the lateral shift of the simulated curves compared to the experimental curves.

4.4 Other experimental results

To study the effect of the arrangement of nanoparticles on magnetic ordering, we have prepared samples with islands of different dimensions by changing some parameters during the drop-casting and drying procedure: using different concentrations of particles in the solution, changing the drying time, by changing the solvent (Decalin or hexane) or drying the sample under an angle. The following configurations have been obtained and studied:

- Very large islands.

- Very small islands.
- Maze-like structures.

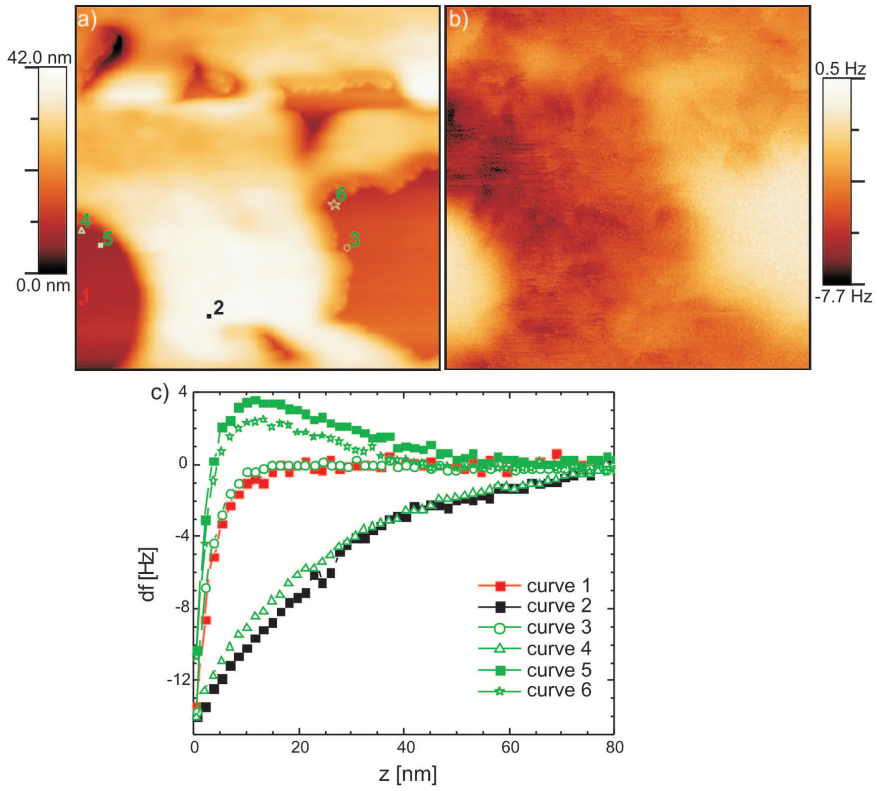

Figure 4.11: *Measurements on a* 1×1 μm^2 *area on the sample where a very large island of nanoparticles is present performed at RT. (a) Topography. (b) MFM image taken at 60 nm. (c) Spectroscopy curves taken at the locations indicated in (a).*

On a large island (Fig. 4.11) the results are similar to those presented in Section 4.2. We present here curves measured at the side of the island that are repulsive (curves 5,6), attractive (curve 4) and without (very small) magnetic interactions (curve 3). These observations are consistent with the proposed model of flux-closure.

We did measurements also on very small islands. We present the results in Fig. 4.12. From the line profile shown in Fig. 4.12(b) and considering its shape, it follows that the island has up to 4 particles. From the spectroscopy curves, it follows that the magnetic signal is small, only slightly larger than the noise level. This makes it difficult to observe repulsion. In Fig. 4.12(d) simulated spectroscopy curves for an arrangement of 1, 7, and 19 hexagonal packed particles are presented. With the tip situated in the middle of the arrangement, the curves were calculated in a similar fashion as the curves presented in fig. 4.10. The tip is interacting mainly with the particle directly

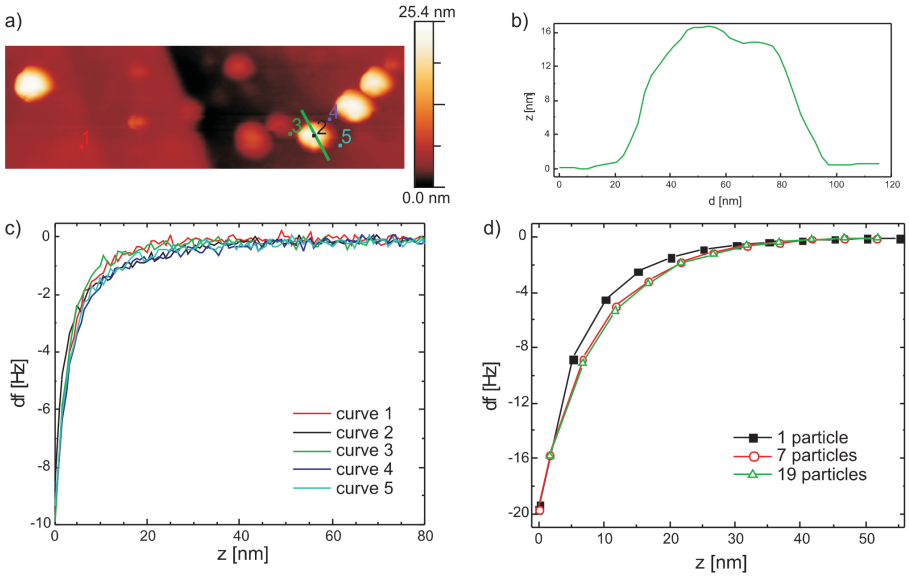

Figure 4.12: *Measurements carried out at 130 K on a* $278 \times 1000\ nm^2$ *area on the sample where small islands are present. (a) Topography. (b) Line profile along the green line indicated in (a). (c) Spectroscopy curves taken at the locations indicated in (a). (d) Simulated spectroscopy curves (magnetic interactions only) for a hexagonal arrangement of 1, 7, and 19 particles. They are laterally shifted do that* $z = 0$ *nm corresponds to -20 Hz.*

beneath it and with its first order neighbors. Since the curves calculated for 7 and 19 particles are practically identical, the interaction between tip and second order neighbors is negligible. Because of the finite dimensions of a realistic tip, however, in the experiments more particles may play a role.

In Fig. 4.13 experimental and simulated results are presented for the maze-like structures. The maze-type structures are interesting to study because the arrangement of nanoparticles may favor the flux closure arrangement of magnetic moments. This is illustrated in Fig. 4.13(d), where simulations were done for a configuration of 54 particles at room temperature. As it can be noticed from the topography and the experimental MFM image (Fig. 4.13), the magnetic contrast is smaller than in the previous measurements. This is at least partially likely to be due to the smaller magnetic moment of the tip (the tip used in these specific measurements was new, therefore sharp), although the arrangement of the moments in a "more perfect" flux-closure structure may also play a role. The repulsion is very weak at the side of the islands. Curve 5 in Fig. 4.13(c) shows the strongest repulsion we have found for these structures, which is much weaker than the one observed for large islands. The interaction even becomes attractive for large z-distances.

We have previously discussed the lateral distance dependence of the magnetic interaction (60 nm for the measurement presented in Fig. 4.3 and 30 nm

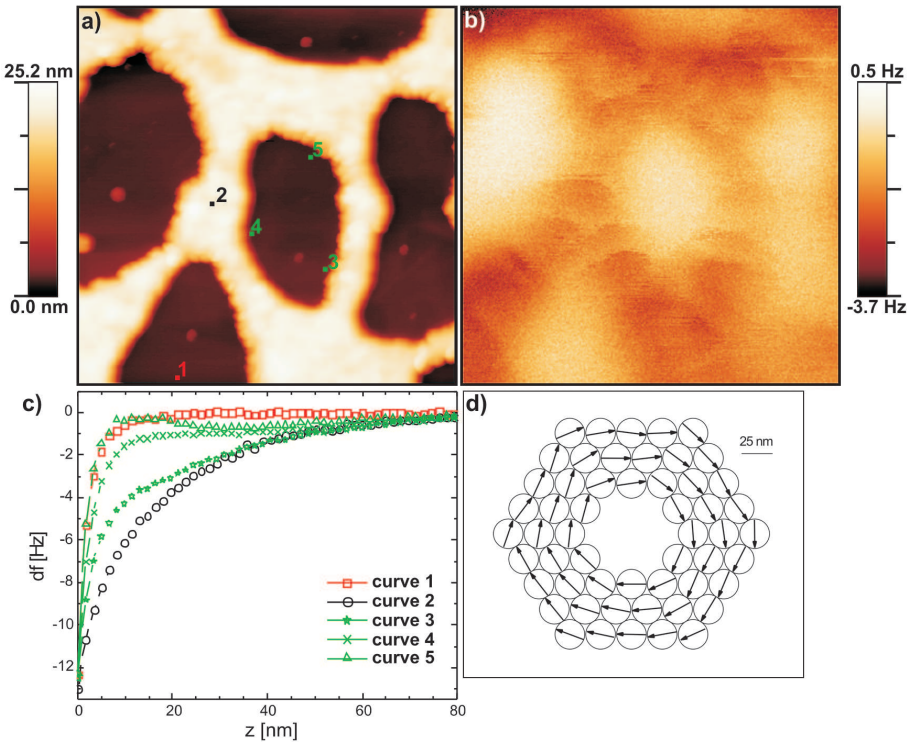

Figure 4.13: *Measurements performed at room temperature on a* 1×1 μm^2 *area where maze-like structures are present. (a) Topography. (b) MFM image taken at 60 nm. (c) Spectroscopy curves taken in the locations indicated in (a). (d) Numerical simulation.*

for the simulation presented in Fig. 4.8). This distance is estimated at 20 nm for the maze-like structures.

4.5 Conclusions and outlook

We have shown in this chapter that in 2D systems of magnetite particles (20 nm in diameter) magnetic dipole-dipole interactions play an important role in the arrangement of the magnetic moments resulting in a flux-closure type of configuration. On top of the islands of nanoparticles we observed only attraction caused by the strong magnetic field of the tip. Repulsion, the uncontested prove of blocking of moments, is found only at the side of the islands, with the tip laterally further away.

To reduce the effect of the stray field of the tip on the magnetic moments of the nanoparticles, we may consider the use of other particles. A significant increase in the size of the magnetite particles would increase the strength of the dipolar interactions and experiments on such systems would therefore be interesting. However, large particles may consist of more than one magnetic

domain thereby reducing the magnetic moment of the particles. We therefore decided to continue with particles consisting of another material, i.e. cobalt ferrite. The cobalt ferrite particles have a large cubic anisotropy and, therefore, a much larger internal energy barrier. This is anticipated to lead to stronger blocking of the moments in the presence of the tip and therefore also repulsion on top of the islands might be observed.

5 Short-range magnetic order in cobalt-ferrite nanoparticle assemblies

In the previous chapter two-dimensional assemblies of magnetite nanoparticles have been studied. We have concluded that the dipole-dipole interactions are too small to block the moments while the tip is in the close proximity of the nanoparticles. We consider next the case of 21 nm $CoFe_2O_4$ particles. Although the magnetization of these particles is similar as for the magnetite particles, cobalt-ferrite presents high coercivity at low temperatures, suggesting that the cobalt-ferrite nanoparticles exhibit a large anisotropy energy. That means that, at low temperature, the anisotropy energy creates large internal barriers for rotation of the magnetic moment, which are difficult for the particles to overcome, even in the large field of the tip. The existence of the barriers will be demonstrated experimentally in the MFM images and in spectroscopy experiments, where attraction and repulsion on top of the islands is observed. Monte-Carlo simulations have been carried out to study in more detail the arrangement of the moments in a 2D assembly of cobalt-ferrite nanoparticles. They illustrate the short-range magnetic order as a consequence of dipole-dipole interactions at high temperature and high anisotropy energy at low temperature.

5.1 Background

In this chapter we describe a study of 2D systems of cobalt ferrite ($CoFe_2O_4$) nanoparticles, 21 nm in diameter with a polydispersity below 9 %. Their magnetic moment is similar to that of the magnetite nanoparticles which were studied in the previous chapter. Additionally, particles with a small diameter of 8 nm are investigated.

Unlike magnetite, $CoFe_2O_4$ is known to exhibit large magnetic anisotropy at low temperature [18]. Song et al. [26] have experimentally observed large differences between the magnetic properties of magnetite and cobalt-ferrite nanoparticles of the same size, (including the blocking temperature, and hence, the anisotropy constant). Apparently, the strong L-S coupling at Co^{2+} lattice sites generates a large anisotropy constant and therefore large energy barriers for the rotation of the magnetic moment within cobalt-ferrite nanoparticles exist. The internal energy barrier is expected to block the moments. We will show that this, together with the dipole-dipole interactions, give rise to short-range order of the magnetic moments in a 2D assembly of these particles.

In a study by Chinnasamy et al. [17] it was determined from coercivity vs. particle-size curves that the single domain size of $CoFe_2O_4$ is about 40 nm. Our particles are significantly smaller than 40 nm and can therefore be considered to have one magnetic domain.

Most of the studies on cobalt-ferrite nanoparticles do not consider the temperature dependence of the anisotropy constant. Our measurements done at room temperature and at low temperatures give significantly different results. Since the magnetization has only a weak dependence on temperature, we conclude that anisotropy must play an important role at low temperature. We will use in our calculations an anisotropy constant with a temperature dependence as for bulk $CoFe_2O_4$:

$$K_1 = a \cdot \exp(-b \cdot T^2) \tag{5.1}$$

where $a = 19.6 \cdot 10^5\ J/m^3$ and $b = 1.9 \cdot 10^{-5}\ K^{-2}$ [18]. At 300 K this results in $K_1 = 3.5 \cdot 10^5\ J/m^3$. Using the work done by Chinnasamy et al. [17], we can estimate K_1 for 21-nm diameter cobalt-ferrite particles to be $4.0 \cdot 10^5\ J/m^3$ at room temperature, which is close to the value obtained using the temperature dependence for bulk cobalt ferrite. In our simulations, we will consider a cubic anisotropy model, i.e. each particle has three easy axes perpendicular to each other. The orientation of the easy axes of a specific particle is arbitrarily oriented with respect to the easy axes of the other particles.

The cobalt-ferrite particles were prepared and deposited by drop casting on HOPG to form monolayered islands. The sample was annealed at 500 K for two hours in vacuum. Without this procedure, instabilities occurred during scanning, which were probably caused by the excess surfactant present on the surface. After annealing no structural changes to the individual particles, like disintegration, or conglomeration of particles were noticed.

5.2 Experimental results

Room temperature

At first we describe experiments on the cobalt-ferrite samples carried out with the sample at room temperature (RT). A typical result of an nc-AFM experiment is shown in Fig. 5.1.

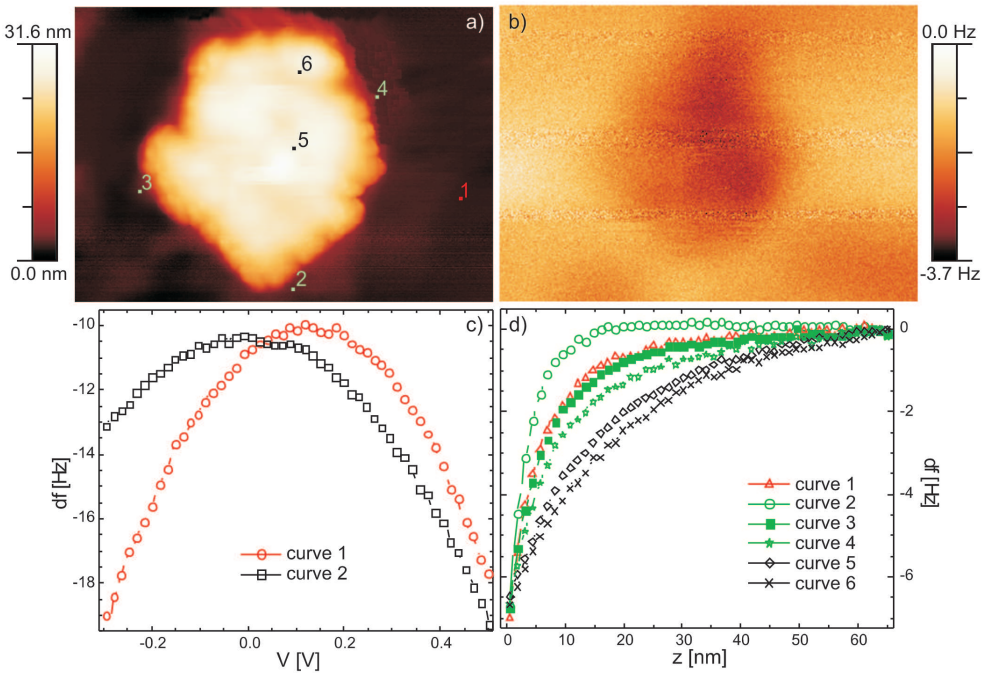

Figure 5.1: *Measurements on a sample with 21-nm $CoFe_2O_4$ particles, taken at RT. We have used a magnetic tip with a resonant frequency of 74.7 kHz oscillated with an amplitude of about 8 nm. (a) "Topography" of a 500 × 353 nm^2 area on the sample. (b) MFM image of the same area taken at 40 nm from the substrate. (c) V-spectroscopy curves taken on top of the substrate (curve 1) and on top of the island (curve 2). (d) z-spectroscopy taken in the locations indicated in (a).*

The size of the nanoparticle island, imaged in Fig. 5.1(a), indicates it consists of up to 100 particles. The MFM image shows attraction with virtually no contrast variation on top of the island. Before the scanning experiments were taken, V-spectroscopy was performed to find the appropriate voltage to minimize the electrostatic forces. Curve 1 in Fig. 5.1(c) was measured on top of the substrate and shows a maximum at 125 mV while curve 2, measured on top of the island, presents a maximum at -25 mV. We applied a voltage of 0 V that ensures a good compensation for electrostatic forces on top of the island while the electrostatic signal on top of the substrate is below 0.5 Hz. The z-spectroscopy results shown in Fig. 5.1(d) are consistent with the MFM image: strong attraction on top of the island (curves 5,6). At the side of the island, weak repulsive and attractive forces are measured, as shown by curves 2, 3 and

4. Note that curve 1, measured on top of the substrate, illustrates the rather poor compensation for electrostatic forces since it has a weak dependence with the distance in between 25 and 50 nm. The results are reminiscent of what we observed at two-dimensional islands of magnetite nanoparticles, presented in the previous chapter. The interpretation, therefore, is along the same lines: the dipole moments of the individual particles are blocked due to dipole-dipole interactions and, for cobalt ferrite, also due to anisotropy. This may lead to repulsive interactions when the tip is at the side of the island. Directly above the island, however, the stray field of the tip is sufficiently strong to reorient the dipole moments of the particles, leading to attraction.

Another example of a measurement performed at room temperature is presented in Fig. 5.2. The island is smaller, consisting of about 50 particles. The MFM image shows features on top of the island, similar to the ones observed for magnetite and presented in Fig. 4.4. For magnetite, we explained them considering the dipole-dipole interactions partly blocking the moments when the tip is sufficiently far away. The spectroscopy measurements are given in Fig. 5.2(c) and show mainly attraction. However, at about 31 nm for curve 4 and 17 nm for curve 6, a jump in the curves occurs. We propose that these jumps are related to switching of the moments by the magnetic field of the tip.

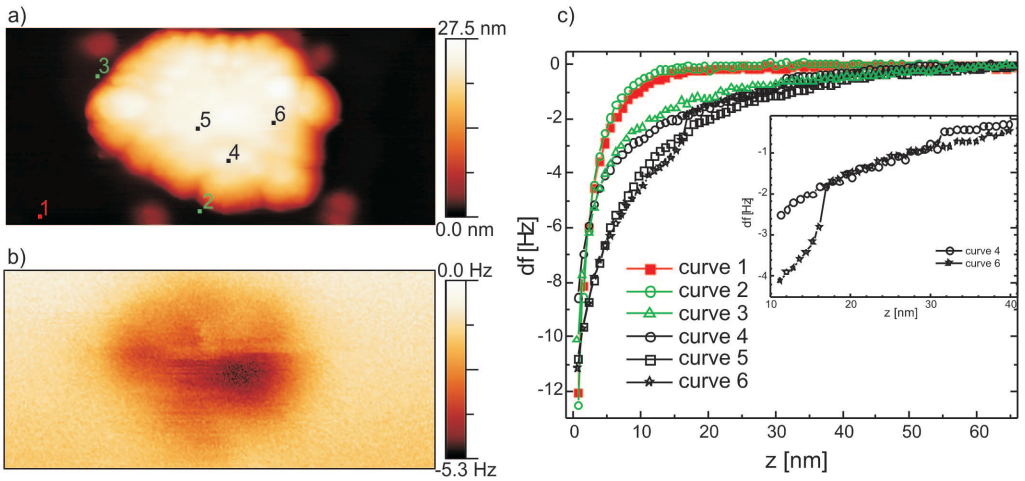

Figure 5.2: *Measurements performed at RT. (a) Topography of a* $450 \times 200\ nm^2$ *area on the sample. (b) MFM image of the same area, taken at 40 nm distance from the substrate (15 nm from the island surface). (c) z-spectroscopy measured at the locations indicated in (a). The inset shows details of curves 4 and 6.*

We interpret the occurrence of the jumps as follows. At small distances, the tip and nanoparticle system is found in a minimum-energy configuration with the magnetic moments of the particles in a specific arrangement. As the distance increases, the influence of the tip becomes smaller and the sys-

tem not only relaxes towards flux-closure, but, even more, it jumps into a lower energy minimum configuration. This means that the configuration of moments changes significantly. It seems that the tip intermediates a jump in between two energy minima. The features on top of the island, revealed in the MFM image, may be explained in the same fashion: with the tip at 15 nm from the island, the configuration of moments may be found close to a critical point, where a switch may occur. E.g. with the tip in position 6, from the spectroscopy curve it becomes clear that this takes place at about 16 nm. Therefore, at specific positions, as the tip scans above the island the configuration of moments changes, resulting in a variation of the contrast. A strong indication that the variation in contrast is not only related to the flux-closure (i.e. the MFM image is not only a result of the interaction of the tip with the ensemble of moments arranged in one specific flux-closure type structure) is the sharpness of the features in the MFM image: the distance in which the contrast changes is below 5 nm, much smaller than the resolution that can be achieved in our MFM measurements.

Since the cobalt-ferrite nanoparticles at room temperature behave similarly to the magnetite nanoparticles, we propose that the features observed for the magnetite in Fig. 4.4 have the same nature as the ones here presented.

Low temperature: large islands

For cobalt ferrite, the temperature is an important parameter as with decreasing temperature the anisotropy constant strongly increases as shown by equation 5.1. In this section we report a study of the $CoFe_2O_4$ nanoparticle system at low temperature to investigate how this increase in anisotropy affects the behavior of the moments in the presence of the tip. We present in Fig. 5.3 and 5.4 two typical results obtained at 80 K and 96 K, respectively. They show large islands, of about 70 and 180 particles, respectively. The MFM images clearly show that above the island not only attractive but also repulsive areas are present. This result is markedly different from the results obtained at room temperature and is supported by force-spectroscopy experiments taken in the attractive as well as in the repulsive areas. Obviously, at these reduced temperatures, the anisotropy energy barriers in the particles are sufficiently high to prevent reorientation of the dipole moments by the stray field of the tip. The repulsive and attractive 2D areas are of rather arbitrary shape and typically exhibit a characteristic length in the range of 70 nm to 130 nm. With the finite size of the tip limiting the lateral resolution to approximately 40 nm, the actual size of the areas may be somewhat smaller. Interesting to note is that in the bright areas in the MFM image individual particles are visible in topography. This can be explained as follows. Where repulsive magnetic interactions are present and therefore the moments are blocked, the force has, at small distances, a strong dependence with the distance, leading to an enhanced resolution.

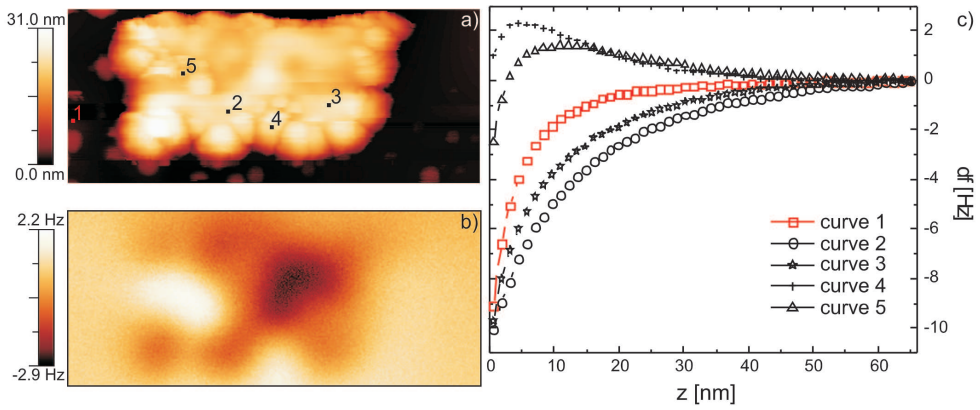

Figure 5.3: *Measurements done at T=80 K. (a) Topography of a* 500×210 nm^2 *area. (b) MFM image of the same area taken at 45 nm from the substrate. (c) Spectroscopy curves, frequency shift vs. distance, taken in the positions indicated in (a).*

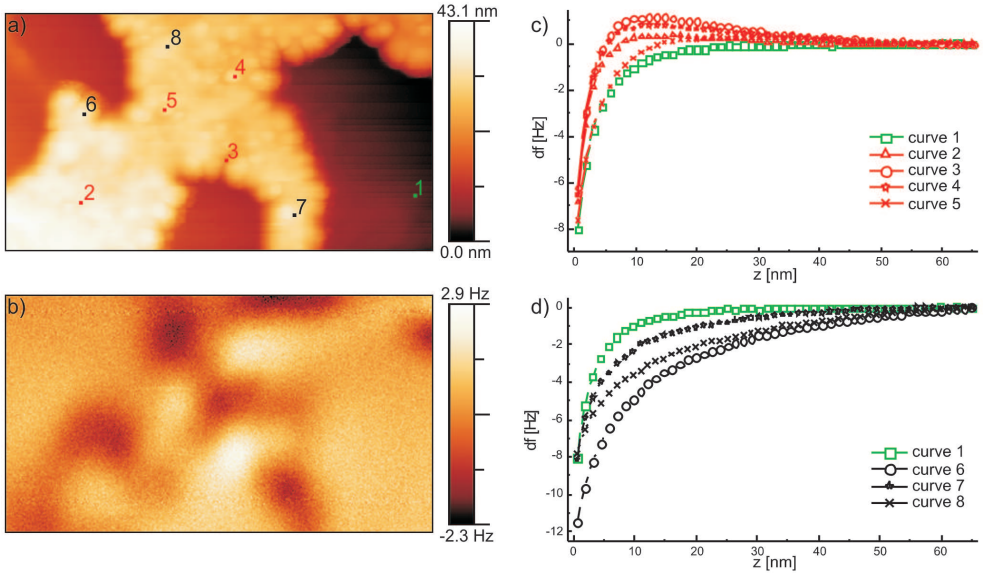

Figure 5.4: *(a) Topography and (b) MFM image (taken at 40 nm from the substrate) of a* 700×390 nm^2 *area on the sample measured at 96 K. (c-d) Frequency shift as a function of the tip-sample distance taken at the locations indicated in (a).*

Low temperature: small islands

An interesting question arises what will happen with the size and shape of the repulsive and attractive areas when the size of the island decreases. We next present results obtained on small islands at low temperatures. The measurements presented in Fig. 5.5 were obtained at a temperature of 100 K and shows an island consisting of 30 to 50 nanoparticles. The MFM image, taken at 40 nm from the substrate, reveals two main areas, one bright area reflecting

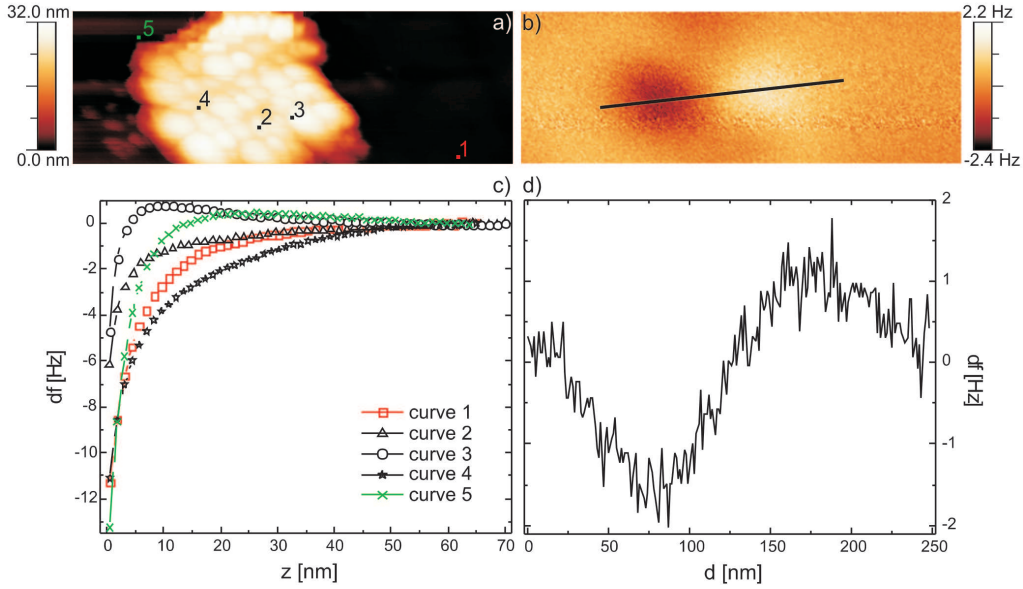

Figure 5.5: *Measurements performed at 100 K. (a) Topography of a* $425 \times 150\ nm^2$ *area on the sample. (b) MFM image of the same area taken at 40 nm from the substrate. (c) z-spectroscopy performed at the locations indicated in (a). (d) Line profile taken along the black line in (b).*

repulsion and one dark area reflecting attraction. Spectroscopy curves measured on top of the island (curves 2-4 in Fig. 5.5(c)) are consistent with the MFM image. Curve 5, measured at the side of the island, shows repulsion. For a distance of z = 40 nm, this spectroscopy curve exhibits a small frequency shift explaining why repulsion is not noticeable at the edge of the island in the MFM image. It is obvious that the moments are blocked, also for this small island, since repulsive interactions on top of the island are observed. The size of the dark and bright areas is about 100 nm in diameter, as shown in the line profile in Fig. 5.5(d), and is similar to the one observed for large islands.

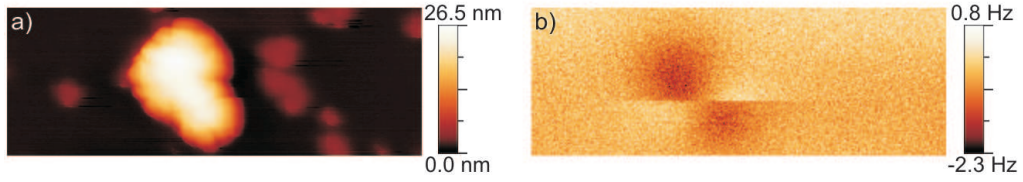

Figure 5.6: *Measurements of a* $500 \times 180\ nm^2$ *area, taken at 175 K. (a) Topography. (b) MFM image taken at 37 nm from the substrate.*

We have observed that at room temperature the stray field of the tip strongly influences the nanoparticle-dipole-moment arrangement (Fig. 5.1 and 5.2), whereas at temperatures around 100 K the moments seem to be blocked (Fig. 5.3, 5.4 and 5.5). To find the temperature at which the behavior of the

moments changes, we have performed measurements at intermediate temperatures. The measurement presented in Fig. 5.6 was performed at 175 K. The MFM image, taken at 37 nm from the substrate, is reproducible meaning that after another topography scan, the same image was obtained. The MFM scan starts at the bottom of the image in a horizontal fashion. After a few line scans two areas can be observed, one indicating repulsion, the other one attraction. During scanning, just below the middle of the image, a reversal of the contrast occurs. The reversal occurs in about 5 nm, equivalent to 3 scan lines. This indicates that the island contains only one attractive and one repulsive area, which switch under the influence of the tip. The dark areas are clearly larger than the bright areas, indicating that the moments are not completely blocked at this temperature. In fact, they may slightly rotate in the field of the tip, thereby increasing the size of the attractive areas. Obviously, although at this intermediate temperature of 175 K it is clear that the moments are sufficiently blocked to give rise to repulsive areas on top of the island, it is also clear that there is an influence of the tip that even seems to be able to switch all the moments at once.

Smaller particles

We have made several experiments on two-dimensional assemblies of significantly smaller cobalt-ferrite nanoparticles. We show in Fig. 5.7 results from experiments carried out on a large island of 8 nm diameter nanoparticles. The MFM image exhibits only very small contrast, reflecting attraction only. The spectroscopy curves shown in Fig. 5.7(d) show that the contrast obtained with the tip on top of the island is indeed small. This makes detection of repulsion a very difficult task. Interesting to note is that in some areas in the topography image individual particles can be distinguished. Unlike the measurements performed on larger particles where these areas were correlated with repulsive areas in the MFM image, the increased resolution in this measurement is probably due to the absence of very long-range attractive forces.

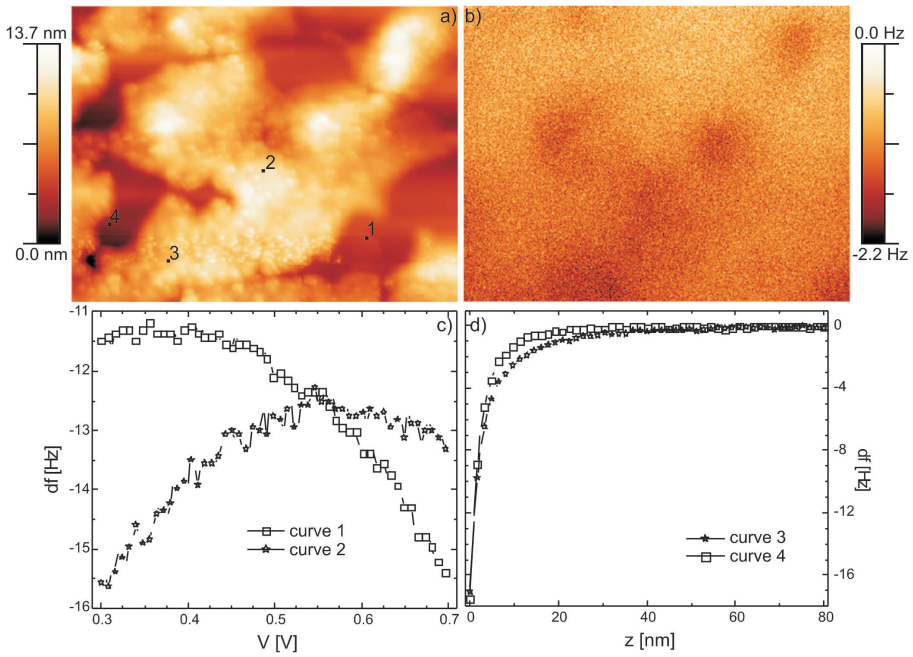

Figure 5.7: *Measurements on a sample containing 8 nm diameter $CoFe_2O_4$ particles performed at room temperature. (a) Topography of a 1×0.77 μm^2 area on the sample. (b) MFM image of the same area taken at 20 nm from the substrate. (c) Frequency shift as function of the applied voltage. For these measurements a voltage of 0.5 V was applied to minimize the electrostatic forces. (d) Spectroscopy curves with the frequency shift as a function of the tip-sample distance. The measurements were performed at the locations indicated in (a).*

5.3 Monte Carlo simulations

High temperature

To study the origin of the repulsive and attractive areas in the measured MFM images, Monte Carlo simulations have been carried out. We have considered the case of a large island consisting of 71 particles. The arrangement of particles is shown in fig. 5.8(a) as well as, in the background, the experimental result from Fig. 5.4(a).

Besides the dipole-dipole interactions, the anisotropy energy is assumed to have a strong effect on the behavior of the dipole moments. We consider the cobalt-ferrite nanoparticles to have cubic anisotropy, with the first anisotropy constant $K_1(T)$ being temperature dependent, as in relation 5.1. The anisotropy constant being positive implies that the easy axes of magnetization coincide with its three cubic crystal axes. The orientation of the crystal axes of each particle was taken to be random with respect to the orientation of the axes of all other particles. During the simulations the particles were not allowed to move or rotate, meaning that the orientation of the easy axes re-

mained the same. We used a value of $1.1 \cdot 10^{-18}\ Am^2$ for the magnetic moment of the particles. The magnetic moment of the tip, $m_{tip} = 2.5 \cdot 10^{-17}\ Am^2$, is assumed to be perpendicular to the surface, pointing towards the sample, as discussed in Section 2.2.

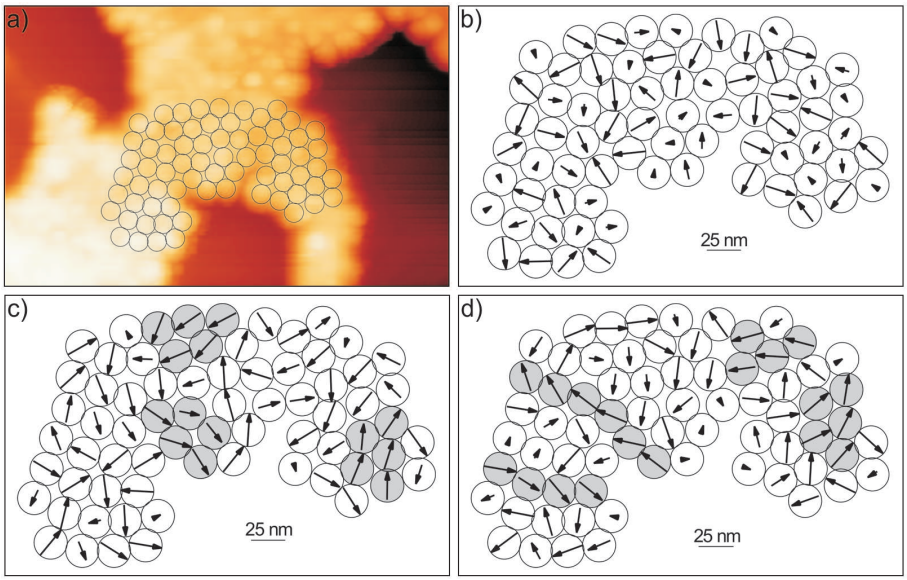

Figure 5.8: *(a) The configuration of 71 nanoparticles used in the simulations. The background shows an experimental topography image of* $665 \times 385\ nm^2$ *area on the sample, shown also in Fig. 5.4(a). (b) The initial configuration of moments. The arrows indicate the direction of the magnetic moments and their length the in-plane component. The easy-axes orientation is arbitrary chosen for each particle and remains the same during the simulations. (c) Calculated configuration of magnetic moments at a temperature* $T = 500\ K$ *after* 10^4 *steps. The grey areas indicate a few of the areas where short-range order is present. (d) Simulated results after another* 10^4 *steps, using the configuration shown in (c) as the initial configuration of moments.*

As discussed in section 5.1, before carrying out the scanning-probe experiments, the sample was annealed at 500 K. We first present the results for simulations at this elevated temperature. We start with an arbitrary configuration of dipole moments, as shown in Fig. 5.8(b). The arrows in the figure correspond to the in-plane components of the moments. After 10^4 Monte Carlo steps, we obtained the configuration shown in Fig. 5.8(c). The moments arrange themselves mostly in plane, although some of them have a significant out-of-plane component. The grey areas, where the moments point to (close to) the same direction, illustrate a few regions where short-range magnetic order is present. The order originates in dipole-dipole interactions, which tend to bring the system in a (partial) flux-closure type arrangement. This is also illustrated by the value of the average dipolar energy per particle

$E^p_{dd} = E_{dd}/71 = -77\ meV$, where E_{dd} is the total dipole-dipole energy as discussed in Section 3.2. The anisotropy energy at 500 K also plays a role, with an average per particle $E^p_{an} = E_{an}/71 = 28\ meV$, where E_{an} is the total anisotropy energy as discussed in Section 3.2. As can be observed in Fig. 5.8 (c) short-range order is obviously present. With an average total energy per particle of -49 meV and a typical height of the anisotropy energy barrier $K_1(T)\cdot V/4 \simeq 68\ meV$, the individual moments are expected to rapidly fluctuate by thermal excitations ($k_BT \simeq 43\ meV$). This is illustrated in Fig. 5.8(d), which is the result of the simulations shown in Fig. 5.8(c) after another 10^4 steps at 500 K and which shows that the magnetization pattern has completely changed.

Low temperature: large islands

We next discuss the behavior of the dipole moments when the particle assemblies are cooled to a temperature of 100 K. The effect of the anisotropy is expected to increase significantly because of its exponential dependence on temperature. To mimic the experimental procedure as good as possible, the moments obtained in the simulations for 500 K were used as input for the simulation for 100 K. As an example, we used the results shown in Fig. 5.8(c). They are shown again in Fig. 5.9(a), together with the result obtained for 100 K, Fig. 5.9(b).

In the simulations for 500 K, some areas with short-range order can be identified. Upon cooling, these areas seem to preserve their short-range order, but the moments become more disordered and the average dipole-dipole energy per particle decreases from -77 meV to -60 meV. Since at this temperature the anisotropy energy has increased by almost two orders of magnitude, this can be easily understood in terms of a reorientation of the dipole moments in the direction of one of their easy axes. As a result, the average anisotropy energy per particle remains low, 9 meV per particle. Since the energy barriers ($K_1(T)\cdot V/4 \simeq 6.5\ eV$) are very high compared to k_BT, they are virtually impossible to cross by thermal excitations at 100 K and the magnetization pattern therefore remains stable. Important to note is that the presence of short-range order at this temperature is a consequence of the order already present at 500 K, with the dipole moments remaining at an energetically favorable side of the anisotropy energy barriers during the cooling process. To confirm this picture, we carried out simulations at 100 K that were started with an arbitrary set of initial moments. The dipole moments were not able to cross the energy barriers, resulting in the absence of short-range order and an average dipole-dipole energy per particle very close to 0.

The 100-K configuration is presented again in Fig. 5.9(c), together with, in the background, the calculated MFM signal. An important observation is that the contrast (bright and dark areas) in the MFM image cannot be related, one-to-one, to areas of short-range order or to transition regions between these

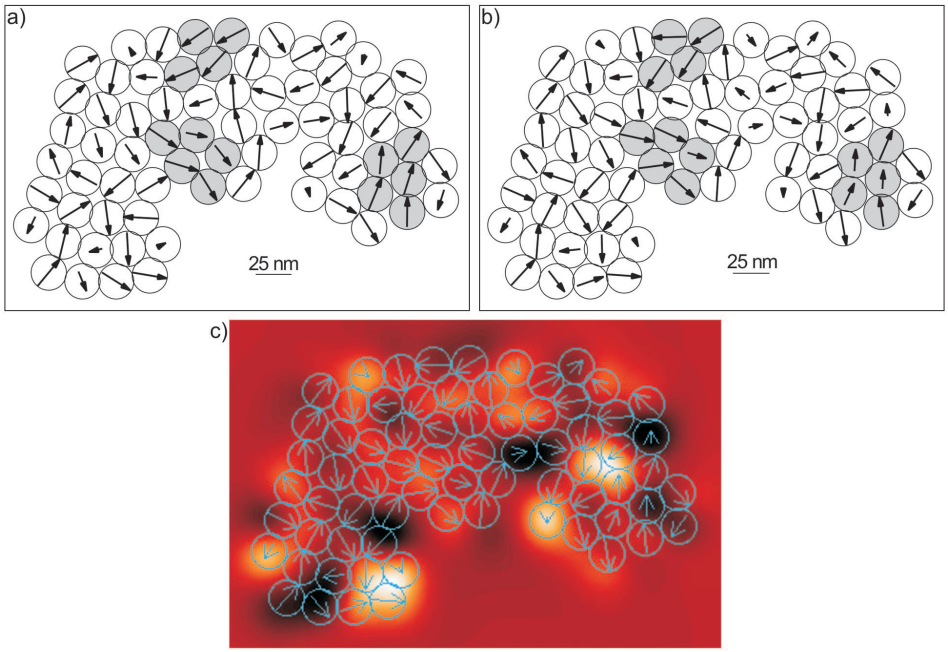

Figure 5.9: *(a) Calculated configuration of moments at a temperature of T=500 K. (b) Calculated configuration of moments at 100 K using as input the configuration presented in (a). The particles were not allowed to rotate, therefore the orientation of the easy axes remains the same during these simulations. (c) The same configuration as presented in (b) and, in the background, the MFM image calculated with the tip moving at 50 nm from the substrate (25 nm from the nanoparticles). The area is* 375×265 nm^2*. The colors range from dark (-2.4 Hz) to bright (2.6 Hz).*

areas. This shows that an interpretation of the MFM image of a system of interacting dipoles is less straight-forward than the interpretation of an image of magnetic domains in ferromagnetic materials. The size of the repulsive and attractive areas in Fig. 5.9(c) is up to 5 particles, smaller than the ones observed in the experimental results shown in Fig. 5.3 and 5.4. However, as pointed out in the experimental section, the size of the contrast areas in the experiments is larger due to the limited resolution of the MFM measurements.

Low temperature: small islands

In the following, we present the results of the simulations on smaller islands. In the experiments, no significant differences are observed when measuring on small islands compared to measuring on large islands. An arrangement of 37 particles was considered in the simulations. Its dimensions and shape are similar to those of the experimentally studied island presented in Fig. 5.5, as it can be seen in Fig. 5.10(a). We have used the same procedure as in the case of a large island to find the final configuration of moments: we have considered an arbitrary configuration of initial moments and easy axes. The

easy axes were fixed during the simulations while the moments were allowed to rotate in order to minimize the total energy of the system. The arrangement obtained by performing Monte Carlo calculations for 500 K was used as initial configuration for the simulation for 100 K. Both configurations are presented in Fig. 5.10(b) and (c), respectively. The final configuration obtained for 100 K has a total dipole-dipole energy of -1.76 eV. This means an average dipolar energy per particle of -48 meV, slightly smaller than the value obtained in the simulation performed for the large island. This is probably due to the (assumed) more disordered arrangement of particles (than in the case of the arrangement of 71 nanoparticles previously considered); the distance between some particles is larger, resulting in a smaller dipole-dipole energy. This results also in a smaller anisotropy energy (4 meV per particle) since, as the interaction between dipoles is weaker, the moments will rotate more towards the easy axes directions. Note that, by definition, the anisotropy energy becomes zero when the moments are aligned along one of the easy axes direction and positive otherwise (see equation 3.9).

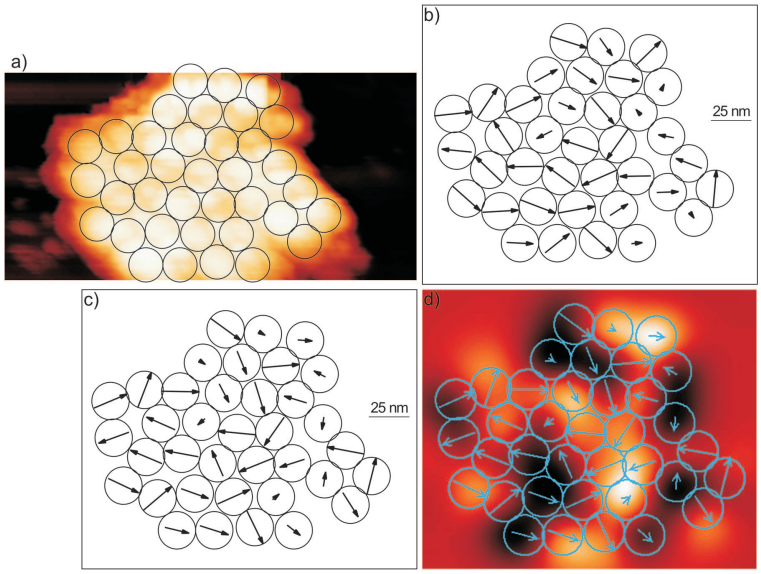

Figure 5.10: *(a) The configuration of 37 nanoparticles considered in the simulations. The background shows the experimental image of the small island presented in Fig. 5.5. The area of the topography image here presented is* $150 \times 270\ nm^2$*. (b) Configuration of moments calculated at T=500 K using an arbitrary initial configuration of moments and an arbitrary orientation of the easy axes of the individual particles. (c) Configuration of moments calculated at 100 K using as input the configuration presented in (b). (d) Same result as presented in (c) with, in addition, the MFM signal calculated at a distance of 50 nm from the substrate (area of* $200 \times 170\ nm^2$*). Colors range from dark (-2.3 Hz) to bright (2.4 Hz).*

Although, by inspecting the arrangement of moments, it may not be di-

rectly clear that short-range order is present, the relatively large value of the dipole-dipole energy is the prove that short-range order is still present as a reminiscence of flux-closure. Fig. 5.10(d) presents the final configuration of moments and the MFM image calculated with the tip at a distance of 50 nm from the substrate. Dark and bright areas are obtained, reflecting attraction and repulsion. The size of these areas is up to 3 particles. As also observed experimentally, there are no significant differences between small and large islands regarding the nature, size and shape of the repulsive and attractive areas.

Influence of the tip

One should realize that the contrast in the calculated MFM images is obtained while 'freezing' the orientation of the moments thus neglecting the influence of the tip. So far we have not yet shown with our simulations whether or not the increased anisotropy at low temperatures can lead to blocking of the moments in the presence of the tip. We have therefore performed simulations on the small island where, with the tip in one position $(x_0,\ y_0)$, the moments were allowed to relax in the presence of the tip. Monte Carlo simulations were performed for different z values to simulate the spectroscopy curves.

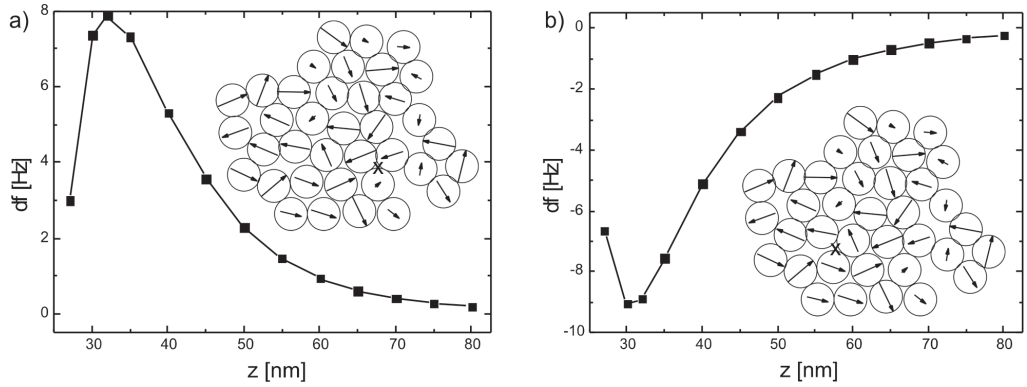

Figure 5.11: *Spectroscopy curves (frequency shift vs. distance) calculated considering the influence of the tip in the positions indicated in the inset figure at a temperature of T=100 K. z=0 nm corresponds to the substrate surface, z=25 nm to the top of the island. (a) Repulsive interaction. (b) Attractive interaction.*

The spectroscopy curves simulated at the indicated positions on the small island are shown in Fig. 5.11. Also shown are the configurations of moments calculated in the presence of the tip at a distance z=27 nm from the substrate (2 nm from the island surface). The configuration of moments obtained appears identical to the one presented in Fig. 5.10(c) where the tip was not considered. The spectroscopy curve presented in Fig. 5.11(a), taken in an area where, according to Fig. 5.10(d), repulsion is present, shows indeed repulsion. A similar agreement is obtained for another location, chosen in an attractive

area (Fig. 5.11(b)). This shows that the anisotropy energy is sufficiently large to virtually completely block the moments in the field of the tip.

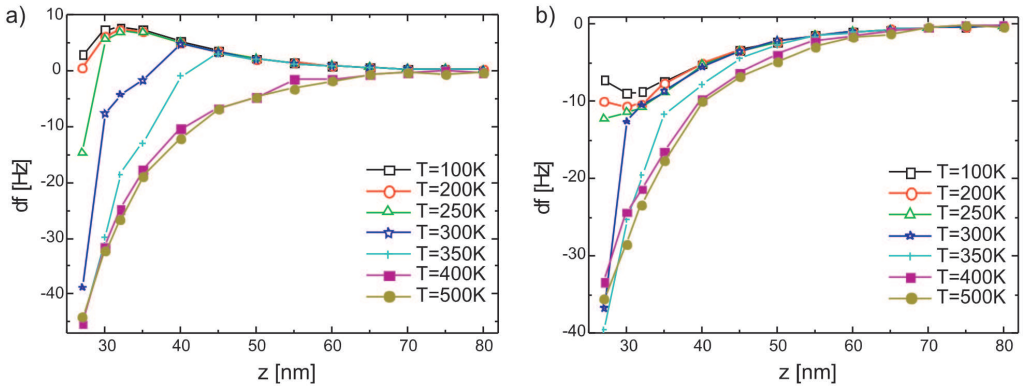

Figure 5.12: *Spectroscopy curves calculated at different temperatures with the tip in the position indicated in the inset of (a) Fig. 5.11(a) and (b) Fig. 5.11(b).*

When the temperature increases, the anisotropy constant decreases. To investigate at which temperature the anisotropy energy is so low that the moments are not blocked anymore in the field of the tip, we simulated the behavior of the spectroscopy curves as a function of temperature. The results for the repulsive and attractive areas are shown in Fig. 5.12 (a) and (b), respectively.

For 100 K the curves are indicating repulsion and attraction, respectively, as previously discussed. The moments are blocked even with the tip at a distance of only 2 nm from the particles (27 nm from the substrate). At 400 K and 500 K, both curves show attraction: the presence of the tip makes the dipole moments arrange themselves in the direction of the field lines. For the repulsive case, at intermediate temperatures (Fig. 5.12(a)), the curves seem to jump from the attractive curve at small distances to the repulsive curve at large distances. This makes sense since with increasing distance the influence of the tip decreases.

We next discuss the case of an intermediate temperature of 300 K in more detail. The case of the repulsive interactions is presented in Fig. 5.13. In Fig.5.13(a) two simulated z-spectroscopy curves are presented: one with the tip influencing the moments, the other one without. As it can be seen for distances smaller than 35 nm there is a large influence of the tip: the curve becomes attractive. The configuration of moments at z=27 nm, presented in Fig. 5.13(b), shows the moments of the three closest neighbors of the tip aligning themselves away from the tip, in the direction of the field lines of the tip. At $z = 35\ nm$, the moments are slightly relaxed, two of them arranging themselves in the head-to-tail configuration. As the tip-sample distance increases to 40 nm, the orientation of the moments becomes identical to the one calculated with the tip at an even larger distance of 80 nm, as shown in

Fig. 5.13(d) and (e), respectively. The curve calculated taking into account the influence of the tip becomes, for distances larger than 40 nm, virtually identical to the one in which the tip was considered but did not influenced the arrangements of moments. It seems that a jump in the configuration of moments of nearby particles occurs in between 35 nm and 40 nm, related to a switch of the moments.

According to the simulated spectroscopy curve in Fig. 5.13(a), at room temperature it would still be possible to experimentally observe repulsion on top of the island. Since this did not happen in our experiments, it seems that the anisotropy constant considered in the simulations is somewhat larger than the experimental one. This may well be since for 21-nm cobalt-ferrite nanoparticles the value of the anisotropy constant is likely to be smaller than the bulk value.

The case of attractive interactions, at T=300 K, is presented in Fig. 5.14. For a tip-sample distance of 2 nm (27 nm from the substrate), the moments are strongly influenced by the tip. This is illustrated in the spectroscopy curve in Fig. 5.14(a) that considers the influence of the tip (i.e. the curve becomes strongly attractive) as well as the configuration of moments presented in Fig. 5.14(b) where the moments of the nearest-by neighbors of the tip significantly change their orientation. As the tip-sample distance increases, the moments relax towards the configuration where the influence of the tip was not considered. Note that at 15 nm (40 nm from the substrate) the influence of the tip is already negligible (compare Fig. 5.14(e) to Fig. 5.10(c)).

The rotation of the moments as the tip-sample distance increases followed by the jumps in the spectroscopy curves in Fig. 5.13 and 5.14 may represent the same phenomena as the experimental observation of switching of the direction of the moments and jumps in spectroscopy curves presented in Fig. 5.2 and 5.6.

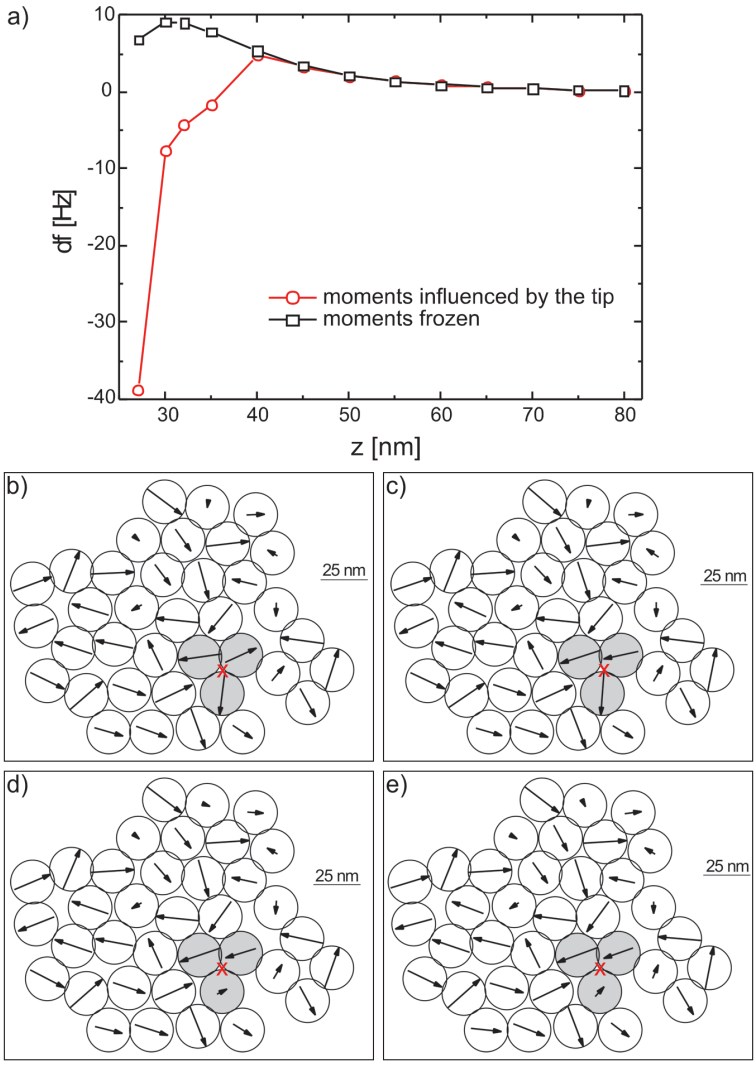

Figure 5.13: *Simulations for a temperature of T=300K. (a) Spectroscopy curves calculated considering the influence of the tip (red curve) and with the moments frozen (black curve). (b-e) The calculated configuration of moments at a distance of z=27 nm, 35 nm, 40 nm and 80 nm, respectively, with the influence of the tip taken into account. The (x,y) position of the tip is indicated by the red cross.*

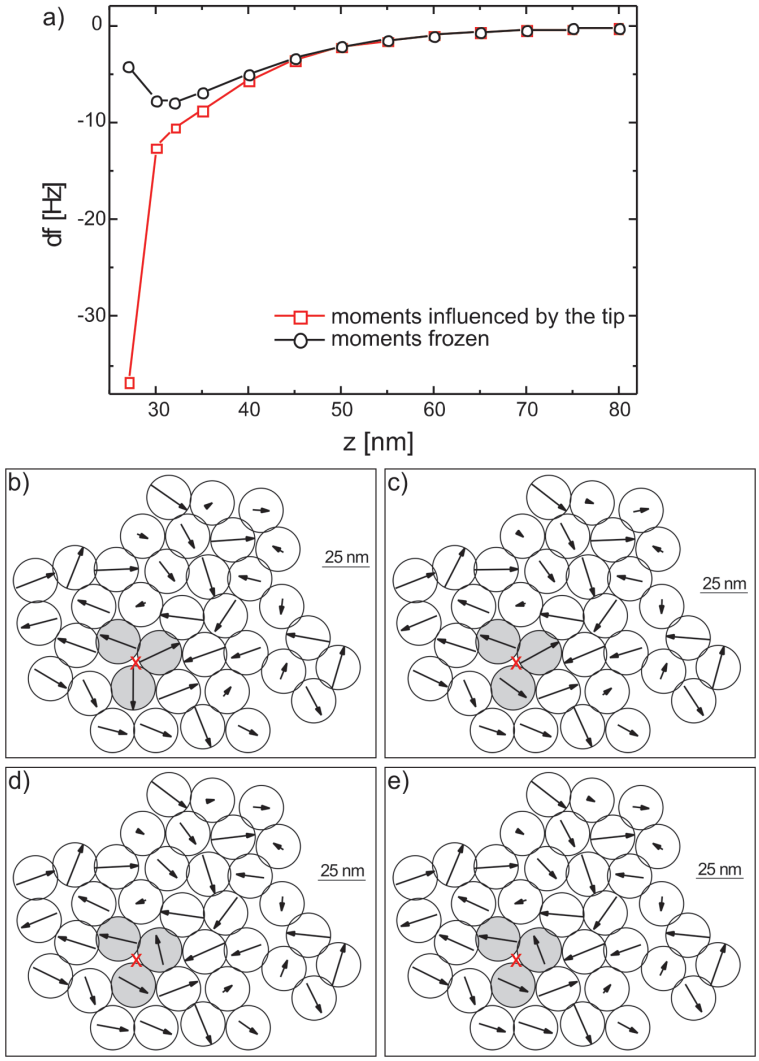

Figure 5.14: *Simulations for a temperature of T=300K. (a) Spectroscopy curves calculated considering the influence of the tip (red curve) and with the moments frozen (black curve). (b-e) The calculated configuration of moments at a distance z=27 nm, 30 nm, 35 nm and 40 nm from the substrate, respectively, with the influence of the tip taken into account. The (x,y) position of the tip is indicated by the red cross.*

5.4 Conclusion and outlook

In this chapter, we have shown that for two-dimensional assemblies of 21-nm cobalt-ferrite nanoparticles, mainly dipole-dipole interactions play an important role in the (short-range) ordered arrangement of moments at 500 K. The order is preserved as the temperature decreases. At low temperature the large magnetocrystalline anisotropy plays an important role in the blocking of the moments in the strong field of the tip. This explains the experimental observation of repulsion and attraction on top of the island at low temperatures. At room temperature, on the other hand, the anisotropy constant is relatively small and the behavior of the moments becomes similar to the one for 20-nm magnetite particles. The numerical simulations illustrate the short-range order of the moments, the presence of attractive and repulsive interactions on top of the island and the blocking of the moments in the presence of the tip.

6 General conclusions

In this thesis, scanning probe microscopy has been used to study magnetic interactions in two-dimensional nanoparticle assemblies. Results for two systems have been presented: 20-nm magnetite (Fe_3O_4) nanoparticles and 21-nm cobalt ferrite ($CoFe_2O_4$) nanoparticles. We have presented an analytical model to interpret the spectroscopy curves (frequency-shift as a function of the distance) in terms of force, to enable a quantitative interpretation of the experimental results. In addition, a model based on the Metropolis Monte Carlo method has been developed to calculate the configuration of magnetic moments with minimum energy. The energy consists of dipolar energy and anisotropy energy. The simulations have shown that several local energy minima are present that correspond to different configurations of magnetic moments. Because of the thermal energy, the system may jump in between these energy minima. Considering a specific configuration of moments, MFM images were simulated taking the dipolar interactions between the particles and the tip into account. Spectroscopy curves were calculated for two cases: namely with and without the influence of the tip.

The magnetite nanoparticles present a relatively large magnetic moment and exhibit strong dipole-dipole interactions and small, negligible, anisotropy. The observed repulsion between tip and nanoparticles at the side of the nanoparticle islands shows that dipolar coupling between the particles causes blocking of their magnetic moments. The experimental observations agree well with the numerical calculations, which show that the magnetic moments arrange themselves in flux-closure structures. However, the magnetite nanoparticle 2D systems can be considered soft-magnetic: their moments are strongly influenced by the strong field of the tip. This has been observed experimentally and confirmed by simulations for the considered value of the magnetic moment of the tip. The results open up the way to more detailed and more quantitative

studies: a tip with a smaller magnetic moment [58] would be more suitable for the study of such soft-magnetic samples. The numerical simulations so far have been carried out with a point-like magnetic moment representing the tip. This can be improved by considering a more realistic shape and size of the tip.

The cobalt-ferrite nanoparticles present a similar magnetic moment as the magnetite nanoparticles. The anisotropy, however, increases significantly with decreasing temperature, which leads to blocking of the moments even in the strong field of the tip. As a consequence, attractive and repulsive areas were observed in the MFM images above the islands of nanoparticles. In our simulations we assumed arbitrary orientations of the easy axes of the particles. The simulation results reveal short-range order of the magnetic moments, consistent with the experimental results.

Magnetic moments considerably larger than any possible moment of the individual particles were recently reported by Trudell et al. [59,60]. The results were interpreted in terms of strongly interacting dipoles resulting in a increase of the observed effective moment. The areas of short-range order presented in the present thesis correspond to the 'correlated clusters' as discussed in ref. [60]. We have furthermore shown that the repulsive and attractive areas in the MFM images of interacting dipoles cannot directly be related to areas with aligned moments (domain-like structures). This should be taken into account in the interpretation of the MFM images of one- and two-dimensional assemblies of interacting nanoparticles as discussed elsewhere [37, 61].

Finally, we propose that the occurrence of areas of short-range order in 2D assemblies of nanoparticles may be of use for magnetic data storage purposes. It has been proposed recently [62] that for use of 2D assemblies of magnetic nanoparticles it would be 'highly desirable that the ordered particles have a common magnetic easy axis'. The present results illustrate that in assemblies of nanoparticles with cubic anisotropy, a relatively high degree of short-range order can be achieved without their axes being aligned. This may open interesting possibilities for future application of such nanoparticle assemblies.

Appendix

A Determination of the local constants c and d

T(x) is defined as:

$$T(x) = I_1(x)e^{-x} \tag{A.1}$$

where I_n is the modified Bessel function of order n,

$$I_1(x) = -\frac{1}{\pi}\int_{-1}^{1} \frac{ue^{-xu}}{\sqrt{1-u^2}}du \tag{A.2}$$

and the proposed dependence in $x = \lambda a$ is:

$$T(x) = cx^d \tag{A.3}$$

therefore

$$I_1(x) = cx^d e^x \tag{A.4}$$

Using the formulas:

$$I_1'(x) = \frac{1}{x}I_1(x) + I_2(x) \tag{A.5}$$

and

$$I_1(x) = \frac{x}{2}I_0(x) - \frac{x}{2}I_2(x) \tag{A.6}$$

to obtain

$$I_1'(x) = \frac{I_0(x)}{2} + \frac{I_2(x)}{2} \tag{A.7}$$

Calculating the derivative in equation A.4 we obtain another expression for $I_1'(x)$:

$$I_1'(x) = ce^x x^{d-1}(x+d) \tag{A.8}$$

We form a system of two equations with two unknowns, c and d:

$$\begin{aligned} I_0(x) + I_2(x) &= 2ce^x x^{d-1}(x+d) \\ I_1(x) &= ce^x x^d \end{aligned} \tag{A.9}$$

Solving the system, we obtain:

$$d = \frac{x}{2}\,\frac{I_0(x) - 2I_1(x) + I_2(x)}{I_1(x)} \tag{A.10}$$

$$c = \frac{I_1(x)}{x^d e^x} \tag{A.11}$$

$x = \lambda a$ where $1/\lambda$ is the characteristic length scale and a is the amplitude.
If $x \gg 1$ (corresponding to the large amplitude regime) $d = -0.5$
If $x \approx 1$ (corresponding to the intermediate amplitude regime) $d = 0$
If $x \ll 1$ (corresponding to the small amplitude regime) $d = 1$

B CALCULATION OF THE FREQUENCY SHIFT WITH FRACTIONAL INTEGRALS

$$df(z) = \frac{f_0 c}{a^{1-d}k}\int_0^\infty A(\lambda)\lambda^d e^{-\lambda z} d\lambda \tag{B.1}$$

If $\mathbf{d} \in [\mathbf{-0.5}, \mathbf{0})$, we start with:

$$\begin{aligned} \int_z^\infty \frac{F(u)}{(u-z)^{1+d}} du &= \int_z^\infty (u-z)^{-1-d} \int_0^\infty A(\lambda) e^{-\lambda u} d\lambda\, du \\ &= \int_0^\infty A(\lambda) \int_z^\infty (u-z)^{-1-d} e^{-\lambda u} du\, d\lambda \end{aligned}$$

Changing the variable $\lambda(u-z) = v$, we obtain:

$$\begin{aligned} \int_z^\infty \frac{F(u)}{(u-z)^{1+d}} du &= \int_0^\infty A(\lambda) e^{-\lambda z} \lambda^d \int_0^\infty v^{-1-d} e^{-v} dv\, d\lambda \\ &= \Gamma(-d) \int_0^\infty A(\lambda) e^{-\lambda z} \lambda^d d\lambda \end{aligned}$$

Therefore we can write relation B.1 in the form

$$df(z) = \frac{f_0 c}{a^{1-d}k}\frac{1}{\Gamma(-d)}\int_z^\infty \frac{F(u)}{(u-z)^{1+d}} du \tag{B.2}$$

If $\mathbf{d} \in (\mathbf{0}, \mathbf{1})$, we start with:

$$\begin{aligned}\frac{d}{dz}\int_z^\infty \frac{F(u)}{(u-z)^d}du &= \frac{d}{dz}\int_z^\infty (u-z)^{-d}\int_0^\infty A(\lambda)e^{-\lambda u}d\lambda\, du \\ &= \frac{d}{dz}\int_0^\infty A(\lambda)\int_z^\infty (u-z)^{-d}e^{-\lambda u}du\, d\lambda\end{aligned}$$

Changing the variable $\lambda(u-z)=v$, we obtain:

$$\begin{aligned}\frac{d}{dz}\int_z^\infty \frac{F(u)}{(u-z)^d}du &= \frac{d}{dz}\int_0^\infty A(\lambda)e^{-\lambda z}\lambda^{d-1}\int_0^\infty v^{-d}e^{-v}dv\, d\lambda \\ &= \Gamma(1-d)\frac{d}{dz}\int_0^\infty A(\lambda)e^{-\lambda z}\lambda^{d-1}d\lambda \\ &= -\Gamma(1-d)\int_0^\infty A(\lambda)e^{-\lambda z}\lambda^{d}d\lambda\end{aligned}$$

Therefore, we can write relation B.1 in the form

$$df(z) = -\frac{f_0 c}{a^{1-d}k}\frac{1}{\Gamma(1-d)}\frac{d}{dz}\int_z^\infty \frac{F(u)}{(u-z)^d}du \tag{B.3}$$

If $\mathbf{d} = \mathbf{0}$ relation B.1 becomes:

$$df(z) = \frac{f_0 c}{ak}\int_0^\infty A(\lambda)e^{-\lambda z}d\lambda = \frac{f_0 c}{ak}F(z) \tag{B.4}$$

If $\mathbf{d} = \mathbf{1}$, equation B.1 becomes:

$$df(z) = \frac{f_0 c}{k}\int_0^\infty A(\lambda)\lambda e^{-\lambda z}d\lambda \tag{B.5}$$

and c=1/2. We start with:

$$\frac{d}{dz}F(z) = \frac{d}{dz}\int_0^\infty A(\lambda)e^{-\lambda z}d\lambda = -\int_0^\infty A(\lambda)\lambda e^{-\lambda z}d\lambda$$

Therefore, relation B.5 becomes:

$$df(z) = -\frac{f_0}{2k}\frac{d}{dz}F(z) \tag{B.6}$$

C CALCULATION OF THE FORCE WITH FRACTIONAL INTEGRALS

For the case of d equals 0 or 1 it is trivial to calculate the force as function of the frequency shift. Therefore, we will concentrate on the intervals $d \in [-0.5,\, 0)$ and $d \in (0,\, 1)$.

If $\mathbf{d} \in [\mathbf{-0.5},\, \mathbf{0})$, we consider the operator:

$$OF(z) = \frac{1}{\Gamma(-d)} \int_z^\infty \frac{F(u)}{(u-z)^{1+d}} du \tag{C.1}$$

We propose an inverse operator O^- with the expression:

$$O^- F(z) = -\frac{1}{\Gamma(1+d)} \frac{d}{dz} \int_z^\infty \frac{F(u)}{(u-z)^{-d}} du \tag{C.2}$$

We have to show that $O^- \cdot O(F(z)) = F(z)$. The calculations for $O \cdot O^-(F(z)) = F(z)$ are similar and will not be presented here.

$$O^-(O(F(z))) =$$

$$= -\frac{1}{\Gamma(1+d)\Gamma(-d)} \frac{d}{dz} \int_z^\infty (u-z)^d \int_u^\infty \int_0^\infty A(\lambda) e^{-\lambda t} (t-u)^{-d-1} d\lambda\, dt\, du$$

Rearranging and changing the variable $v = \lambda(t-u)$ in the integral over t, we obtain:

$$O^-(O(F(z))) =$$

$$= -\frac{1}{\Gamma(1+d)\Gamma(-d)} \frac{d}{dz} \int_0^\infty A(\lambda) \int_z^\infty (u-z)^d \lambda^d e^{-\lambda u} \int_0^\infty v^{-d-1} e^{-v} dv\, du\, d\lambda$$

The integral over v equals $\Gamma(-d)$. We change again the variable in the integral over u, $\lambda(u-z) = t$ and

$$O^-(O(F(z))) = -\frac{1}{\Gamma(1+d)} \frac{d}{dz} \int_0^\infty A(\lambda) \frac{1}{\lambda} e^{-\lambda z} \int_0^\infty t^d e^{-t} dt\, d\lambda$$

The integrals over t equals $\Gamma(1+d)$ and

$$O^-(O(F(z))) = -\frac{d}{dz} \int_0^\infty A(\lambda) \frac{1}{\lambda} e^{-\lambda z} d\lambda = \int_0^\infty A(\lambda) e^{-\lambda z} d\lambda = F(z) \tag{C.3}$$

If $\mathbf{d} \in (\mathbf{0}, \mathbf{1})$, we consider the operator:

$$OF(z) = -\frac{1}{\Gamma(1-d)}\frac{d}{dz}\int_z^\infty \frac{F(u)}{(u-z)^d}du \tag{C.4}$$

We propose a inverse operator O^- with the expression:

$$O^-F(z) = \frac{1}{\Gamma(d)}\int_z^\infty \frac{F(u)}{(u-z)^{1-d}}du \tag{C.5}$$

We have to show that $O\cdot O^-(F(z)) = F(z)$. The calculations for $O^-\cdot O(F(z)) = F(z)$ are similar and will not be presented here.

$$O(O^-(F(z))) =$$

$$= -\frac{1}{\Gamma(1-d)\Gamma(d)}\frac{d}{dz}\int_z^\infty (u-z)^{-d}\int_u^\infty\int_0^\infty A(\lambda)e^{-\lambda t}(t-u)^{d-1}d\lambda\, dt\, du$$

Rearranging and changing the variable $v = \lambda(t-u)$ in the integral over t, we obtain:

$$O(O^-(F(z))) =$$

$$= -\frac{1}{\Gamma(1-d)\Gamma(d)}\frac{d}{dz}\int_0^\infty A(\lambda)\int_z^\infty (u-z)^{-d}\lambda^{-d}e^{-\lambda u}\int_0^\infty v^{d-1}e^{-v}dv\, du\, d\lambda$$

The integral over v equals $\Gamma(d)$. We change again the variable in the integral over u, $\lambda(u-z) = t$ and

$$O(O^-(F(z))) = -\frac{1}{\Gamma(1-d)}\frac{d}{dz}\int_0^\infty A(\lambda)\frac{1}{\lambda}e^{-\lambda z}\int_0^\infty t^{-d}e^{-t}dt\, d\lambda$$

The integrals over t equals $\Gamma(1+d)$ and

$$O(O^-(F(z))) = -\frac{d}{dz}\int_0^\infty A(\lambda)\frac{1}{\lambda}e^{-\lambda z}d\lambda = \int_0^\infty A(\lambda)e^{-\lambda z}d\lambda = F(z) \tag{C.6}$$

References

[1] N. Taniguchi, *On the Basic Concept of "Nano-technology"*, Proc. Intl. Conf. Prod. Eng, Tokio, part 2, Japan Society of Precision Engeneeniring (1974).

[2] J. Rogué, J. Molera, P. Scian, E. Pantos, and M. Vendrell-Saz, *Copper and Silver Nanocrystals in Lustre Lead Glasses: Developement and Optical Properties*, J. Europe Ceramic Soc. **26**, 3813 (2006).

[3] S. Sun, C. B. Murray, D. Weller, L. Folks, and A. Moser, *Monodisperse FePt Nanoparticles and Ferromagnetic FePt Nanocrystal Supperlattices*, Science **287**, 1989 (2000).

[4] V. F. Puntes, K. M. Krishnan, and P. Alivisatos, *Colloidal Nanocrystal Shape and Size Control: The Case of Cobalt*, Science **291**, 2115 (2001).

[5] C. B. Murray, C. R. Kagan, and M. G. Bawendi, *Synthesis and Characterization of Monodisperse Nanocrystals and Close-Packed Nanocrystal Assemblies*, Annu. Rev. Mater. Sci. **30**, 545 (2000).

[6] D. A. Thompson and J. S. Best, *The Future of Magnetic Data Storage*, IBM J. Res. Dev. **44**, 311 (2000).

[7] D. Weller and A. Moser, *Thermal Effect Limits in Ultrahigh-Density Magnetic Recording*, IEEE Trans. Magn. **35**, 4423 (1999).

[8] Q. A. Pankhurst, J Connolly, S. K. Jones, and J. Dobson, *Applications of Magnetic Nanoparticles in Biomedicine*, J. Phys. D: Appl. Phys. **36**, R167 (2003).

[9] P. Tartaj, *Nanomagnets-From Fundamental Physics to Biomedicine*, Current Nanoscience **2**, 43 (2006).

[10] F. Bloch and G. Gentile, *Zur Anisotropie der Magnetisierung ferromagnetischer Einkristalle*, Z. Phys. A **70**, 395 (1931).

[11] R. Skomski, *Simple Models of Magnetism*, Oxford University Press (2008).

[12] A. Hubert and R. Schäfer, *Magnetic Domains: The Analysis of Magnetic Microstructures*, Springer (1998).

[13] L. Néel, *Theorie du trainage magnetique des ferromagnetique en grains fins avec applications aux terres cuites*, Ann. Geophys. **5**, 99 (1949).

[14] N. Moumen, P. Bonville, and M. P. Pileni, *Control of the Size of Cobalt Ferrite Magnetic Fluids: Mössbauer Spectroscopy*, J. Phys. Chem. **100**, 14410 (1996).

[15] V. F. Puntes, K. M. Krishnan, and A. P. Alivisatos, *Synthesis, Self-Assembly, and Magnetic Behavior of a Two-Dimensional Superlattice of Single-Crystal ϵ -Co Nanoparticles*, Appl. Phys. Lett. **78**, 2187 (2001).

[16] N. Moumen and M. P. Pileni, *Control of the Size of Cobalt Ferrite Magnetic Fluid*, J. Phys. Chem. **100**, 1867 (1996).

[17] C. N. Chinnasamy, B. Jeyadevan, K. Shinoda, K. Tohji, D. J. Djayaprawira, M. Takahashi, R. J. Joseyphus, and A. Narayanasamy, *Unusually High Coercivity and Critical Single-Domain Size of Nearly Monodispersed $CoFe_2O_4$ Nanoparticles*, Appl. Phys. Lett. **83**, 2862 (2003).

[18] H. Shenker, *Magnetic Anisotropy of Cobalt Ferrite ($Co_{1.01}Fe_{2.00}O_{3.62}$) and Nickel Cobalt Ferrite ($Ni_{0.72}Fe_{0.20}Co_{0.08}Fe_2O_4$)*, Phys. Rev. **107**, 1246 (1957).

[19] Y. Lalatonne, J. Richardi, and M. P. Pileni, *Van der Waals versus Dipolar Forces Controlling Mesoscopic Organizations of Magnetic Nanocrystals*, Nature Mat. **3**, 121 (2004).

[20] R. W. Chantrell, A. Bradbury, J. Popplewell, and S. W. Charles, *Particle Cluster Configuration in Magnetic Fluids*, J. Phys. D: Appl. Phys. **13**, L119 (1980).

[21] M. Klokkenburg, C. Vonk, E. M. Claesson, J. D. Meeldijk, B. H. Erné, and A. P. Philipse, *Direct Imaging of Zero-Field Dipolar Structures in Colloidal Dispersions of Synthetic Magnetite*, J. Am. Chem. Soc **126**, 16706 (2004).

[22] M. Grigorova, H. J. Blythe, V. Blaskov, V. Rusanov, V. Petkov, V. Masheva, D. Nihtianova, L. M. Martinez, J. S. Muñoz, and M. Mikhov, *Magnetic Properties and Mössbauer Spectra of Nanosized $CoFe_2O_4$ Powders*, J. Magn. Magn. Mater. **183**, 163 (1998).

[23] C. Djurberg, P. Svedlindh, P. Nordblad, M. F. Hansen, F. Bødker, and S. Mørup, *Dynamics of an Interacting Particle System: Evidence of Critical Slowing Down*, Phys. Rev. Lett. **79**, 5154 (1997).

[24] M. Sasaki, P. E. Jönsson, H. Takayama, and H. Mamiya, *Aging and Memory Effects in Superparamagnets and Superspin Glasses*, Phy. Rev. B **71**, 104405 (2005).

[25] C. Liu, A. J. Rondinone, and Z. J. Zhang, *Synthesis of Magnetic Spinel Ferrite $CoFe_2O_4$ Nanoparticles from Ferric Salt and Characterization of the Size-Dependent Superparamagnetic Properties*, Pure Appl, Chem. **72**, 37 (2000).

[26] Q. Song and Z. J. Zhang, *Correlation between Spin-Orbital Coupling and the Superparamagnetic Properties in Magnetite and Cobalt Ferrite Spinel Nanocrystals*, J. Phys. Chem. B **110**, 11205 (2006).

[27] A. Mumtaz, K. Maaz, B. Janjua, S. K. Hasanain, and M. F. Bertino, *Exchange Bias and Vertical Shift in $CoFe_2O_4$ Nanoparticles*, J. Magn. Magn. Mater. **313**, 266 (2007).

[28] W. Luo, S. R. Nagel, T. F. Rosenbaum, and R. E. Rosensweig, *Dipole Interactions with Random Anisotropy in a Frozen Ferrofluid*, Phys. Rev. Lett. **67**, 2721 (1991).

[29] R. W. Chantrell, N. Walmsley, J. Gore, and M. Maylin, *Calculations of the Susceptibility of Interacting Superparamagnetic Particles*, Phy. Rev. B **63**, 024410 (2000).

[30] J. Garcia-Otero, M. Porto, J. Rivas, and A. Bunde, *Influence of Dipolar Interaction on Magnetic Properties of Ultrafine Ferromagnetic Particles*, Phys. Rev. Lett. **84**, 167 (2000).

[31] J. -O. Andersson, C. Djurberg, T. Jonsson, P. Svedlindh, and P. Nordblad, *Monte Carlo Studies on the Dynamics of an Interacting Monodispersive Magnetic-Particle System*, Phys. Rev. B **56**, 13983 (1997).

[32] S. Mørup and E. Tronc, *Superparamagnetic Relaxation of Weakly Interacting Particles*, Phys. Rev. Lett. **72**, 3278 (1994).

[33] P. Poddar, T. Telem- Shafir, T. Fried, and G. Markovich, *Dipolar Interactions in Two- and Three-dimensional Magnetic Nanoparticle Arrays*, Phys. Rev. B **66**, 060403(R) (2002).

[34] T. Fried, G. Shemer, and G. Markovich, *Ordered Two-Dimensional Arrays of Ferrite Nanoparticles*, Adv. Mater. **13**, 1158 (2001).

[35] J. B. Kortright, O. Hellwig, K. Chesnel, S. Sun, and E. E. Fullerton, *Interparticle Magnetic Correlation in Dense Co Nanoparticle Assemblies*, Phys. Rev. B **71**, 012402 (2005).

[36] Y. Sun and M. B. Salamon, K. Garnier, and R. S. Averback, *Memory Effects in an Interacting Magnetic Nanoparticle System*, Phys. Rev. Lett. **91**, 167206 (2003).

[37] V. F. Puntes, P. Gorostiza, D. M. Aruguete, N. G. Bastus, and A. P. Alivisatos, *Collective Behaviour in Two-dimensional Cobalt Nanoparticle Assemblies Observed by Magnetic Force Microscopy*, Nat. Mater. **3**, 263 (2004).

[38] F. G. Giessibl, *Advances in Atomic Force Microscopy*, Rev. Mod. Phys. **75**, 949 (2003).

[39] G. Meyer and N. Amer, *Novel Optical Approach to Atomic Force Microscopy*, Appl. Phys. Lett. **53**, 1054 (1988).

[40] S. Alexander, L. Hellemans, O. Marti, J. Schneir, V. Elings, P. K. Hansma, M. Longmire, and J. Gurley, *An Atomic-Resolution Atomic-Force Microscope Implemented Using an Optical Lever*, J. Appl. Phys. **65**, 164 (1989).

[41] M. Raşa, B. W. M. Kuipers, and A. P. Philipse, *Atomic Force Microscopy and Magnetic Force Microscopy Study of Model Colloids*, J. Coll. Int. Sci. **250**, 303 (2002).

[42] S. Sun and H. Zeng, *Size-Controlled Synthesis of Magnetite Nanoparticles*, J. Am. Chem. Soc **124**, 8204 (2002).

[43] S. Sun, H. Zeng, D. B. Robinson, S. Raoux, P. M. Rice, S. X. Wang, and G. Li, *Monodisperse MFe_2O_4 (M=Fe, Co, Mn) Nanoparticles*, J. Am. Chem. Soc. **126**, 273 (2004).

[44] J. L. Viota, *Synthesis and Characterization of Monodisperse Cobalt Ferrite Nanoparticles*, Internal report (2006).

[45] H. Hölscher and U. D. Schwartz, *Theory of Amplitude Modulation Atomic Force Microscopy*, Int. J. Non-Lin. Mechan. **42**, 608 (2007).

[46] U. Hartmann, *Magnetic Force Microscopy*, Annu. Rev. Mater. Sci. **29**, 53 (1999).

[47] J. G. Zhu, *New Heights for Hard Disk Drives*, Mat. Today **6**, 22 (2003).

[48] F. J. Giessibl, *Forces and Frequency Shifts in Atomic-Resolution Dynamic Force Microscopy*, Phys. Rev. B **56**, 16010 (1997).

[49] U. Dürig, *Relations between Interaction Force and Frequency Shift in Large Amplitude Dynamic Force Microscopy*, Appl. Phys. Lett. **75**, 433 (1999).

[50] J. E. Sader, and S. P. Jarvis, *Interpretation of Frequency Modulation Atomic Force Microscopy in Terms of Fractional Calculus*, Phys. Rev. B **70**, 012303 (2004).

[51] S. H. Ke, T. Uda, and K. Terakura, *Quantity Measured in Frequency-Shift-Mode Atomic-Force Microscopy: An Analysis with a Numerical Model*, Phys. Rev. B **59**, 13267 (1999).

[52] T. R. Albrecht, P. Grütter, D. Horne, and D. Rugar, *Frequency Modulation Detection using High-Q Cantilevers for Enhanced Force Microscope Sensitivity*, J. Appl. Phys. **69**, 668 (1991).

[53] B. K. Agarwal, M. Eisner, *Statistical mechanics*, New Age International Publishers, 1973.

[54] http://mathworld.wolfram.com/EulerAngles.html

[55] http://wwwmaths.anu.edu.au/ brent/random.html

[56] C. N. Marin, I. Malaescu, and A. Ercuta, *The Dependence of the Effective Anisotropy Constant on Particle Concentration within Ferrofluids, Measured by Magnetic Resonance*, J. Phys. D: Appl. Phys. **34**, 1466 (2001).

[57] M. P. Pileni, *Magnetic Fluids: Fabrication, Magnetic Properties, and Organization of Nanocrystals*, Adv. Funct. Mater. **11**, 323 (2001).

[58] M. R. Koblischka and U. Hartmann, *Recent Advances in Atomic Force Microscopy*, Ultramicroscopy **97**, 103 (2003).

[59] S. Trudel and R. H. Hill, *Magnetic Properties of Binary Mixtures of Metal Oxide Nanoparticles*, Polyhedron **26**, 1863 (2007).

[60] S. Trudel, C. H. W. Jones, and R. H. Hill, *Magnetic Properties of Nanocrystalline Iron Oxide/Amorphous Manganese Oxide Nanocomposite Thin Films Prepared via Photochemical Metal-Organic Deposition*, J. Mater. Chem. **17**, 2206 (2007).

[61] J. M. Kinsella and A. Ivanisevic, *DNA-Templated Magnetic Nanowires with Different Compositions: Fabrication and Analysis*, Langmuir **23**, 3886 (2007).

[62] B. D. Terris and T. Thomson, *Nanofabricated and Self-Assembled Magnetic Structures as Data Storage Media*, J. Phys. D: Appl. Phys. **38**, R199 (2005).

Samenvatting

Magnetische nanodeeltjes zijn deeltjes met afmetingen varirend van enkele nanometers tot honderd nanometer, die magnetische elementen zoals ijzer, nikkel of cobalt bevatten (n nanometer is gelijk aan n miljardste meter). Met hedendaagse chemische methoden kunnen de afmetingen van deze deeltjes evenals hun vorm en samenstelling precies gekozen worden. Samen met de mogelijkheid ze te manipuleren in een magneetveld betekent dit dat magnetische nanodeeltjes uitermate geschikt zijn voor een reeks van toepassingen op het gebied van medicijnen, de farmacie en de biotechnologie. Magnetische nanodeeltjes kunnen in de toekomst ook een rol gaan spelen voor de opslag van gegevens op magnetische harde schijven. In de hedendaagse harde-schijf technologie wordt informatie opgeslagen in dunne films, die bestaan uit kleine, willekeurig gevormde, magnetische deeltjes. Een enkel bit wordt weggeschreven in een groepje van deze deeltjes. De toename van opslagdichtheid wordt vooral bereikt door het verkleinen van de afmetingen van de deeltjes; een toename die onvermijdelijk ophoudt wanneer de informatie door thermische effecten verloren gaat.

Naast deze toepassingsmogelijkheden zijn magnetische nanodeeltjes interessant vanuit fundamenteel oogpunt. Een zeer klein magnetisch nanodeeltje, typisch kleiner dan ongeveer 30 nanometer, gedraagt zich als een zeer klein magneetje, een zogenaamde **nanomagneet** met een zekere sterkte en een zekere richting. De eigenschappen van een nanomagneet worden bepaald door zijn afmetingen, zijn vorm, het materiaal waaruit het deeltje is opgebouwd en zijn precieze (kristallijne) structuur. De richting van de nanomagneet hangt nauw samen met de interne energie van het deeltje: voor bepaalde richtingen, zogenaamde voorkeursrichtingen, is deze energie minimaal. Bij een sferisch gevormd deeltje, zoals bestudeerd in dit proefschrift, kunnen deze voorkeursrichtingen veroorzaakt worden door de kristallijne structuur van het deeltje. Doordat het deeltje een bepaalde temperatuur heeft, heeft het thermische energie en probeert de nanomagneet continu "spontaan" van richting te veranderen (binnenin het deeltje, dus zonder dat het deeltje zelf beweegt). Op het moment dat de nanomagneet van de ene voorkeursrichting naar een andere draait, moet een bepaalde energie barrire overwonnen worden. De energie term die deze barrire veroorzaakt wordt de anisotropie energie genoemd. Wanneer de energie barrire beduidend hoger is dan de thermische energie is de nano-

magneet vrijwel "vastgevroren" in het deeltje. Wanneer de barrire echter even hoog is als dan wel lager is dan de thermische energie, verandert de richting van de nanomagneet continu. Dit laatste verschijnsel wordt superparamagnetisme genoemd.

Wanneer twee magnetische nanodeeltjes dicht bij elkaar worden gebracht zullen ze wisselwerken, d.w.z. het magneetveld van de ene nanomagneet oefent een kracht uit op de andere nanomagneet. Wanneer de afstand tussen de nanodeeltjes een paar nanometer bedraagt, wordt de wisselwerking in de eerste plaats bepaald door een zogenaamde dipool-dipool interactie. Deze interactie probeert de nanomagneten in de "kop-staart" configuratie te brengen, zoals te zien is in onderstaande figuur. De cirkels in de figuur representeren de nanodeeltjes, de pijlen de nanomagneten (de pijlen wijzen van zuidpool ("staart") naar noordpool ("kop")). De figuur laat zien dat er twee voorkeurssituaties op kunnen treden, die beiden corresponderen met een zo laag mogelijke interactie energie.

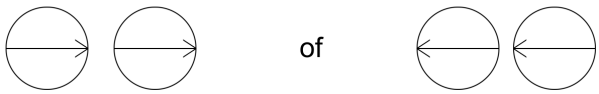

In dit proefschrift wordt een studie beschreven van twee-dimensionale structuren van sferische magnetische nanodeeltjes, die onderzocht zijn met rastermicroscopische technieken (atomaire kracht microscopie en magnetische kracht microscopie). De twee-dimensionale structuren kan men zich het best voorstellen als grote eilanden van slechts n laag dik, waarbij de deeltjes als pingpongballen tegen elkaar aan liggen. Bij atomaire kracht microscopie worden de deeltjes afgetast met een zeer scherpe naald, die bevestigd is aan een buigzame naaldhouder. Wanneer de afstand tussen naald en deeltjes voldoende klein is, wordt een kracht op de naald uitgeoefend waardoor de naaldhouder doorbuigt. Door de naaldhouder tijdens het aftasten een bepaalde mate van doorbuigen "op te leggen", wat in feite betekent dat de kracht op de naald constant gehouden wordt, kunnen de vorm en de grootte van de eilanden worden afgebeeld. Magnetische kracht microscopie is hierop een variatie waarbij een magnetische naald wordt gebruikt. Met deze methode kan de magnetische kracht op de naald worden afgebeeld. Dit levert informatie op over de richting van de nanomagneten.

We hebben een numeriek model ontwikkeld, dat voor een gegeven verdeling van magnetische nanodeeltjes de richting van de nanomagneten berekent. Tijdens de berekeningen wordt de richting van de nanomagneten gevarieerd tot er een situatie ontstaat die correspondeert met een minimale energie en dus met een (min of meer) stabiele toestand. In het model wordt ook de magnetische kracht berekend die de nanomagneten uitoefenen op de naald. Dit is belangrijk om een vergelijk te kunnen maken met de experimentele resultaten.

Als eerste systeem hebben we magnetiet nanodeeltjes met een diameter

van 20 nanometer bestudeerd. Magnetiet is een sterk magnetisch ijzeroxide (Fe_3O_4), zodat de wisselwerking tussen de nanodeeltjes sterk is. Aangezien de anisotropie energie van magnetiet klein is, waardoor er binnenin de deeltjes nauwelijks voorkeursrichtingen zijn, wordt de richting van de nanomagneten vooral bepaald door de onderlinge wisselwerking. Onze numerieke berekeningen laten zien dat de nanomagneten zichzelf richten in een zogenaamde "flux closure" structuur. In een dergelijke structuur komen "kop-staart" configuraties, zoals we al gezien hebben voor een twee-deeltjes systeem (zie figuur), van aangrenzende nanomagneten relatief vaak voor. De numerieke berekeningen zijn consistent met de experimentele resultaten, die laten zien dat het systeem van nanomagneten inderdaad een stabiel systeem is. Echter, de metingen laten ook zien dat het magneetveld van de naald de richting van de nanomagneten benvloed. Dit is een ongewenst effect en we hebben daarom besloten om op een ander systeem over te gaan.

Het tweede systeem dat we bestudeerd hebben bestaat uit cobalt-ferriet ($CoFe_2O_4$) nanodeeltjes met een diameter van 21 nanometer. Ook cobalt ferriet is sterk magnetisch, zodat de wisselwerking tussen de nanodeeltjes weer sterk is. De aanwezigheid van cobalt zorgt er echter voor dat bij lage temperaturen de anisotropie energie groot is. Dit betekent dat er binnenin een deeltje sterke voorkeursrichtingen zijn voor de richting van de nanomagneet, waardoor de invloed van het magneetveld van de naald veel geringer zou moeten zijn. De numerieke berekeningen en de experimentele resultaten laten dit inderdaad zien en geven aan dat er kleine gebiedjes zijn waarin de nanomagneten dezelfde richting hebben.

Dit werk vertegenwoordigt een fundamentele studie aan twee-dimensionale systemen van magnetische nanodeeltjes. We hebben de mechanismen beschreven die tot magnetische orde leiden voor twee verschillende typen nanodeeltjes. Uit dit werk kan verder nog het volgende worden geconcludeerd. De interpretatie van raster-microscopie experimenten aan dit soort systemen moet zorgvuldig worden uitgevoerd en is zeker niet zo eenvoudig als beschreven door anderen in de literatuur. Verder kunnen onze bevindingen voor cobalt-ferriet nanodeeltjes mogelijk worden gebruikt voor toekomstige technologie voor de opslag van gegevens op magnetische harde schijven.

Rezumat

Nanoparticulele magnetice sunt particule cu dimensiuni cuprinse între câţiva nanometri şi o sută de nanometri (un nanometru reprezintă a milioana parte dintr-un metru), ce conţin elemente magnetice cum ar fi fier (Fe), nichel (Ni) sau cobalt (Co). În ziua de azi, folosind metode chimice, se pot controla dimensiunile, forma şi compoziţia acestor nanoparticule. Împreună cu faptul că pot fi manipulate în câmp magnetic, face ca aceste particule să aibă numeroase aplicaţii în domenii ca medicină, farmacie şi biotehnologie. Nanoparticulele magnetice sunt de asemeni candidate pentru posibile viitoare hard-disk-uri. În tehnologia hard-disk-urilor actuală, informaţia este stocată în filme subţiri formate din mici granule magnetice, cu forme neregulate. Un bit corespunde unui grup de granule magnetizate. Creşterea densităţii de biţi se realizează în principiu prin reducerea dimensiunilor granulelor; creştere care se va opri când, din cauza efectelor termice, informaţia de pe hard disk se va pierde.

Pe lângă aceste aplicaţii practice, particulele magnetice sunt de asemenea interesante de studiat din punct de vedere fundamental. O nanoparticulă magnetică mică (mai mică decât aproape 30 nm) se comportă ca un magnet minuscul, aşa numit **nanomagnet**, care are o direcţie şi o putere. Puterea nanomagneţilor e dată de mărimea, forma, materialul din care sunt făcute nanoparticulele. Pentru o particulă sferică, ca cele studiate în această carte, structura sa cristalină creează direcţii privilegiate în interiorul particulelor; dacă nanomagnetul e aliniat acestor direcţii energia internă a particulelor e minimă. Deoarece se află la o anumită temperatură, aceste particule au energie termică iar nanomagnetul va încarca "spontan" să îşi schimbe direcţia (numai nanomagnetul se poate roti, nu şi nanoparticula). Pentru ca nanomagnetul să îşi schimbe orientarea de la o direcţie privilegiată la alta, o barieră energetică trebuie să fie depăşită; energia care cauzează această barieră se numeşte energie de anizotropie. Când energia de anizotropie e mai mare decât energia termică nanomagnetul este "îngheţat" în interiorul nanoparticulei, dacă aceasta nu se află în câmp magnetic extern. Când energia de anizotropie este mai mică decât energia termică nanomagnetul se poate roti continu. Acest fenomen se numeşte superparamagnetism.

Când nanoparticulele sunt apropiate unele de altele, ele interacţionează; adică câmpul magnetic creat de o particulă exercită o forţă asupra celor-lalte particule. Dacă distanţa dintre nanoparticule este de câţiva nanometri,

interacţia predominantă între nanoparticule este forţa dipolară. Această interacţie tinde să aranjeze nanomagneţii în configuraţia numită "cap-coadă", aşa cum este ilustrat în imaginea următoare, unde cercurile reprezintă nanoparticule iar săgeţile reprezintă nanomagneţii. Imaginea prezintă două situaţii care corespund energiei de interacţie minime a sistemului de două particule.

În studiul efectuat, structuri bidimensionale (ce pot fi imaginate ca insule mari consistînd dintr-un singur strat) de nanoparticule sferice au fost preparate şi studiate utilizînd următoarele metode: non-contact Atomic Force Microscopy, Atomic Force Spectroscopy şi Magnetic Force Microscopy. Principiul de operare al metodei numită Atomic Force Microscopy este următorul: un ac foarte ascuţit este aflat la capătul unei bare flexibile ataşate unui scaner care se poate deplasa în orice direcţie. Când distanţa dintre ac şi probă e destul de mică, proba acţionează cu o forţă asupra berei flexibile, care se va îndoi. "Cerînd" barei să fie îndoită în acelaşi fel (adică forţa acţionînd asupra barei să fie constantă) în timp ce proba e scanată, atât forma şi mărimea insulei cât şi structuri la nivel nanoscopic pot fi vizualizate. Magnetic Force Microscopy este o variaţie a acestei metode şi e folosită la măsurarea forţelor magnetice; acestea ne dau informaţii despre aşezarea (organizarea) nanomagneţilor în structurile studiate.

În lucrare este prezentat şi un model numeric care calculează, pentru un aranjament al nanoparticulelor dat, configuraţia nanomagneţilor. Modelul presupune o variaţie a orientării nanomagneţilor până când se ajunge la configuraţia corespunzătoare energiei minime a sistemului şi, deci, o configuraţie (mai mult sau mai puţin) stabilă. De asemenea, folosind configuraţia nanomagneţilor calculată, forţa care acţionează asupra acului este calculată. Aceasta este important pentru a putea face o comparaţie cu rezultatele experimentale.

Am studiat un caz particular: nanoparticule de magnetită (Fe_3O_4), cu diametru de 20 nm. Magnetita este un oxid al fierului puternic magnetic, ceea ce face ca interacţiile dintre particule să fie mari. Energia de anizotropie e mică; de aceea particulele nu prezintă direcţii preferenţiale astfel încât orientarea nanomagneţilor este dată de interacţiile dintre particule. Simulări numerice arată că nanomagneţii sunt fixi într-o configuraţie numită "flux-closure". În acest tip de aranjament, configuraţii "cap-coadă", ca cele existente pentru sisteme de două particule (vezi figura), apar frecvent între particule alăturate. Simulările numerice dau rezulate similare cu cele experimentale şi arată că sistemul de nanomagneţi e într-adevăr stabil. Cu toate acestea, în timpul măsurătorilor am realizat că acul, care este de fapt un magnet foarte mic şi ascuţit influenţează aranjamentul nanomagneţilor. Acesta este un efect nedorit şi, pentru a-l evita, am decis să studiem alt sistem de particule.

Următorul caz studiat este cel al nanoparticulelor din ferită de cobalt ($CoFe_2O_4$), de 21 de nm în diametru. Nanomagneţii sunt aproape la fel de puternici ca cei de magnetită, ceea ce face ca interacţiile dintre particule să fie la fel de puternice. Prezenţa cobaltului induce însă o energie de anizotropie mare la temperaturi mici. Aceasta înseamnă că în interiorul particulelor direcţiile preferenţiale sunt foarte puternice, ceea ce face ca influenţa acului asupra aranjamentului de nanomagneţi să fie cu mult mai mică decât în cazul magnetitei. Aceasta se poate observa în calculele numerice efectuate şi rezultatele experimentale, şi arată că există zone reduse în care nanomagneţii sunt aliniaţi.

Acest lucrare reprezintă un studiu fundamental al sistemelor bidimensionale de nanoparticule magnetice. Înţelegem mecanismul care duce la formarea diferitelor tipuri de ordine în două tipuri de sisteme de nanoparticule. Câteva concluzii au fost obţinute în această lucrare. Mai multă atenţie trebuie acordată interpretării rezultatelor experimentale obţinute folosind microscopia folosită de noi în obţinerea acestor rezultate şi cu siguranţă nu e atât de simplă cum a fost folosită în alte lucrări publicate. Noi propunem că rezultatele obţinute pentru sisteme bidimensionale de nanoparticule de ferită de cobalt pot fi folosită în viitoarea technologie de stocare a datelor.

Publications

Publications related to the work described in this thesis:

- *Flux Closure in Two-Dimensional Magnetite Nanoparticle Assemblies*; Phys. Rev. B, **73**, 184415 (2006); M. Georgescu, M. Klokkenburg, B. H. Erné, P. Liljeroth, D. Vanmaekelbergh, and P. A. Zeijlmans van Emmichoven. (part of Chapter 4)
- *Short-Range Magnetic Order in Two-Dimensional Cobalt-Ferrite Nanoparticle Assemblies*; Phys. Rev. B, **77**, 024423 (2008); M. Georgescu, J. L. Viota, M. Klokkenburg, B. H. Erné, D. Vanmaekelbergh, and P. A. Zeijlmans van Emmichoven. (part of Chapter 5)
- Part of Chapter 5 will be included in an article in progress

Acknowledgments

During the creation of this thesis I have rediscovered my style of writing: short and concise. I finish the thesis in the same style: I thank everyone who contributed directly or indirectly to the work described in this thesis and not only: I have evolved as a person, I gained experience, I received encouragements and I went on. I could not have done it without you.

First of all I want to thank my supervisor, Pedro Zeijlmans van Emmichoven, who made this project possible from the beginning until the end. Thank you for an interesting project, your optimism inspired me, your knowledge kept the project running when things seemed hopeless, your wisdom and patience made our long discussions fruitful. I want to thank Frans Habraken. Thank you for your enthusiasm, optimism and interest in my project, for your suggestions and comments.

Our technicians, Jitse and Theo, were up to their task. Jitse, you helped me and you teach me UHV. You always found a solution to problems, you always found in some cabinet an apparatus I needed. Theo, you were our technician in the last years. Your door was open every time we needed you. I thank Mathias, Ralf and Jurgen from Omicron. You were there to answer our questions, you gave us advice. You came as soon as possible to repair our fragile setup, your work was fast and effective so we can return to our experiments as soon as possible.

I thank Ben Erne and Mark Klokkenburg for giving us the material to work with; you prepared the nanoparticles and you gave us useful information we used in our project. I am grateful to Daniel Vanmaekelbergh for keeping the group together and motivating us to obtain more results. To Peter Liljeroth I thank for helping me not only in preparing the samples but also for learning me to use the ambient AFM and sharing his experience in using the UHV setup. You gave us the idea to use Metropolis Monte-Carlo method and even the first version of the numerical program. And to Karin Overgaag, we used the setup and it was a pleasant experience. We shared information and the time to use the setup in a flexible way, so everyone could perform their experiments. To all of you I thank for questions, comments, ideas; they helped us in continuing the project.

With Ernst van Fassen I had interesting discussions. The first one opened the door to Utrecht University, Surfaces, Interfaces and Devices group. I was

nervous and afraid I will not succeed, but you gave me a chance. Other discussions showed me another points of view and tough me some more physics. Thank you.

There was a pleasant atmosphere in room 12c in R. vd Graaff lab thanks to the people that passed by. For a short period of time I shared the room with Marijn. He introduced me to our lab and the setups. Elmuez, I enjoyed sharing the room with you.

To everyone in the (old) Surfaces, Interfaces and Devices group, although our projects did not have much in common I enjoyed our lunch breaks and the few coffee breaks I attended, our "outjes" and spending time together during Do-days! and Winterschool.

To everyone I want thank for your support during a difficult time in my life, specially to Frans and Danielle, Pedro and Maartje, Ernst and Liliana, Riny.

To Carmen and Karin: I was delighted when my best friends have accepted to be my 'paranimfs' for the defense ceremony.

And last but not least, I want to thank my family. Doru şi Anca, deşi departe, aţi fost tot timpul aproape de mine. Trăiască tehnologia! Doru, fără tine viaţa mea ar fi avut un alt curs; tu m-ai încurajat "să-mi iau zborul". Mulţumesc! Florin, tu eşti principalul vinovat pentru apariţia acestei cărţi. Cuvintele care să descrie cât de mult m-ai ajutat sunt de neajuns. Te iubesc!

Curriculum vitae

Mirela (Costache) Georgescu was born December 7^{th} 1978 in Galaţi, Romania. She graduated "Radu Negru high school" in Galaţi in 1997, class of informatics.

She continued her studies in the autumn of the same year at the Physics Faculty, Bucharest University where she graduated in the summer of 2001. In September 2001 she started an Erasmus program at the Brandenburgische Technische Universität Cottbus in the group of Prof. dr. Ernst Sigmund. Under the supervision of Dr. Ulrich Wulf and Paul Racec she obtained her master in science with the thesis entitled "Self-consistent calculations of potential energy and charge distributions for strained Si/SiGe based semiconductor devices".

In August 2003 she started her PhD research at Utrecht University, in the Surface, Interfaces and Devices group, under the supervision of Dr. Pedro A. Zeijlmans van Emmichoven and Prof. dr. Frans H. P. M. Habraken. The results of her research are presented in this thesis an published in scientific journals. The author participated at various schools and workshops and presented her work at conferences. Besides her research activities she was member of the Debye PhD committee, supervised a bachelor student and contributed to two summer schools in nanoscience.